ผลของการผสมโลหะทรานซิชันต่อสมบัติของฟิล์มไนตรายด์และฟิล์มออกไซด์

นางสาวแคททรียา ทวีทรัพย์

บทคัดย่อและแฟ้มข้อมูลฉบับเต็มของวิทยานิพนธ์ตั้งแต่ปีการศึกษา 2554 ที่ให้บริการในคลังปัญญาจุฬาฯ (CUIR)
เป็นแฟ้มข้อมูลของนิสิตเจ้าของวิทยานิพนธ์ ที่ส่งผ่านทางบัณฑิตวิทยาลัย
The abstract and full text of theses from the academic year 2011 in Chulalongkorn University Intellectual Repository (CUIR)
are the thesis authors' files submitted through the University Graduate School.

วิทยานิพนธ์นี้เป็นส่วนหนึ่งของการศึกษาตามหลักสูตรปริญญาวิศวกรรมศาสตรดุษฎีบัณฑิต
สาขาวิชาวิศวกรรมโลหการ ภาควิชาวิศวกรรมโลหการ
คณะวิศวกรรมศาสตร์ จุฬาลงกรณ์มหาวิทยาลัย
ปีการศึกษา 2557

ลิขสิทธิ์ของจุฬาลงกรณ์มหาวิทยาลัย

EFFECT OF TRANSITION METAL-ALLOYING ON THE PROPERTIES OF NITRIDE AND OXIDE FILMS

Miss Kattareeya Taweesup

A Dissertation Submitted in Partial Fulfillment of the Requirements
for the Degree of Doctor of Engineering Program in Metallurgical Engineering
Department of Metallurgical Engineering
Faculty of Engineering
Chulalongkorn University
Academic Year 2014
Copyright of Chulalongkorn University

Thesis Title	EFFECT OF TRANSITION METAL-ALLOYING ON THE PROPERTIES OF NITRIDE AND OXIDE FILMS
By	Miss Kattareeya Taweesup
Field of Study	Metallurgical Engineering
Thesis Advisor	Associate Professor Gobboon Lothongkum, Dr.Ing.
Thesis Co-Advisor	Associate Professor Patama Visuttipitukul, Ph.D.
	Assistant Professor Sukkaneste Tungasmita, Ph.D.

Accepted by the Faculty of Engineering, Chulalongkorn University in Partial Fulfillment of the Requirements for the Doctoral Degree

....Dean of the Faculty of Engineering
(Professor Bundhit Eua-arporn, Ph.D.)

THESIS COMMITTEE

....Chairman
(Associate Professor Prasonk Sricharoenchai, D.Eng.)

....Thesis Advisor
(Associate Professor Gobboon Lothongkum, Dr.Ing.)

....Thesis Co-Advisor
(Associate Professor Patama Visuttipitukul, Ph.D.)

....Thesis Co-Advisor
(Assistant Professor Sukkaneste Tungasmita, Ph.D.)

....Examiner
(Assistant Professor Yuttanant Boonyongmaneerat, Ph.D.)

....External Examiner
(Assistant Professor Niti Yongvanich, Ph.D.)

CHULALONGKORN UNIVERSITY

แคททรียา ทวีทรัพย์ : ผลของการผสมโลหะทรานซิชันต่อสมบัติของฟิล์มไนตรายด์และฟิล์มออกไซด์ (EFFECT OF TRANSITION METAL-ALLOYING ON THE PROPERTIES OF NITRIDE AND OXIDE FILMS) อ.ที่ปรึกษาวิทยานิพนธ์หลัก: รศ. ดร. กอบบุญ หล่อทองคำ, อ.ที่ปรึกษาวิทยานิพนธ์ร่วม: รศ. ดร. ปฐมา วิสุทธิพิทักษ์กุล, ผศ. ดร. สุคคเณศ ตุงคะสมิต, 123 หน้า.

ในปัจจุบันฟิล์มไนตรายด์และฟิล์มออกไซด์มีการนำไปใช้ในอุตสาหกรรมอย่างแพร่หลาย แม้ว่าฟิล์มไนตรายด์เดี่ยวและฟิล์มออกไซด์เดี่ยวจะให้ประโยชน์ในการปรับปรุงผิววัสดุ แต่ก็อาจไม่เพียงพอที่จะป้องกันผิววัสดุในทุกสภาพแวดล้อมการใช้งาน การผสมกันของฟิล์มเดี่ยวเพื่อสร้างฟิล์มที่มีสมบัติใหม่จึงเป็นที่น่าสนใจอย่างมาก การเปลี่ยนแปลงสมบัติของฟิล์มไนตรายด์และฟิล์มออกไซด์ ทำได้โดยการเติมธาตุชนิดอื่นเข้าไป เพื่อเปลี่ยนแปลงสมบัติทางกลและสมบัติการกัดกร่อน ดังนั้นในฟิล์มไนตรายด์จึงเพิ่มธาตุโครเมียมเป็นธาตุผสมเข้าในฟิล์มไทเทเนียมไนตรายด์เพื่อเปลี่ยนแปลงสมบัติของฟิล์มดังกล่าว สำหรับการศึกษาสมบัติทางไฟฟ้าของฟิล์มออกไซด์ได้ทำการเพิ่มธาตุรูทีเนียมเป็นธาตุผสมในฟิล์มอินเดียมออกไซด์เพื่อศึกษาสมบัติทางไฟฟ้าที่เปลี่ยนแปลงไปเช่นกัน ดังนั้นในการทำวิจัยนี้จึงมุ่งเน้นที่จะศึกษาผลของการผสมโลหะทรานซิชันต่อสมบัติของฟิล์มไนตรายด์และฟิล์มออกไซด์เพื่อให้ได้มาซึ่งฟิล์มที่มีสมบัติใหม่ด้วยวิธีการปลูกฟิล์มแบบดีซีแมกนีตรอนสปัตเตอริง ผลที่ได้หลังการเติมธาตุโครเมียมเข้าไปในฟิล์มไทเทเนียมไนตรายด์เกิดเป็นฟิล์มผสม (Ti,Cr)N พร้อมกับการควบคุมโครงสร้างของฟิล์ม พบว่าฟิล์มมีโครงสร้างเปลี่ยนจากคอลัมนาร์เป็นอีควิแอกซ์จากการเพิ่มอุณหภูมิชิ้นงานจากอุณหภูมิห้องขึ้นไปที่ 190 องศาเซลเซียส จากโครงสร้างฟิล์มที่เปลี่ยนไปส่งผลต่อความหยาบผิวของฟิล์มลดลงจาก 2.35 nm เป็น 1.93 nm ความแข็งฟิล์มเพิ่มขึ้นจาก 16.12 GPa เป็น 24.79 GPa และค่า E_{corr} เพิ่มขึ้นจาก -460 mV เป็น -320 mV ขณะที่ I_{corr} ลดลงจาก 0.15 mA/cm^2 เป็น 0.02 mA/cm^2 ดังนั้นฟิล์ม (Ti,Cr)N ที่ปลูกด้วยอุณหภูมิที่ 190 องศาเซลเซียส จึงเป็นฟิล์มที่มีสมบัติป้องกันชิ้นงานดีกว่าฟิล์ม (Ti,Cr)N ที่ปลูกด้วยอุณหภูมิห้อง กรณีของฟิล์มออกไซด์พบว่าหลังการเติมธาตุรูทีเนียมในฟิล์มอินเดียมออกไซด์กลายเป็นฟิล์มผสม $In_{1-x}Ru_xO_y$ พบว่าฟิล์มที่ดีที่สุดคือ ITO (150-nm)/ultrathin $In_{0.38}Ru_{0.62}O_y$ (3 nm) ไบเลเยอร์ ที่มีค่าฟังก์ชันงานประสิทธิผลอยู่ที่ 5.3 eV ยอมให้แสงส่องผ่านถึง 86% และมีความต้านทานทางไฟฟ้าต่ำ 9.2×10^{-5} Ωcm.

ภาควิชา	วิศวกรรมโลหการ	ลายมือชื่อนิสิต	....
สาขาวิชา	วิศวกรรมโลหการ	ลายมือชื่อ อ.ที่ปรึกษาหลัก	....
ปีการศึกษา	2557	ลายมือชื่อ อ.ที่ปรึกษาร่วม	....
		ลายมือชื่อ อ.ที่ปรึกษาร่วม	....

5271856121 : MAJOR METALLURGICAL ENGINEERING
KEYWORDS:

KATTAREEYA TAWEESUP: EFFECT OF TRANSITION METAL-ALLOYING ON THE PROPERTIES OF NITRIDE AND OXIDE FILMS. ADVISOR: ASSOC. PROF. GOBBOON LOTHONGKUM, Dr.Ing., CO-ADVISOR: ASSOC. PROF. PATAMA VISUTTIPITUKUL, Ph.D., ASST. PROF. SUKKANESTE TUNGASMITA, Ph.D., 123 pp.

Recently, nitride-and oxide films were used in tool applications. However, single films (oxide or nitride only) might not be sufficient to protect the matrix from harsh working environment. Combination of two or more single films, might offer potential alternatives to this problem. The properties of nitride-and oxide films could be modified by adding other elements. Cr is one alloying element in a single TiN thin film, offering good mechanical and corrosion properties. Also, to achieve good electrical and physical properties of oxide films, Ru addition to a single In_2O_3 film is an attractive method. Therefore, this research aims to investigate the effect of transition metal-alloying element on single nitride-and single oxide films to obtain proper films properties by using DC magnetron sputtering. After adding Cr into TiN film to be (Ti,Cr)N film with control film structure. An effect of film structure changes from columnar to equiaxed by increase substrate temperature from room temperature (RT) to 190 ℃, causes the reduction of surface roughness from 2.35 nm to 1.93 nm, Hardness of (Ti,Cr)N film increases from 16.12 GPa to 24.79 GPa, and E_{corr} can be increased from -460 mV to -320 mV while I_{corr} decreases from 0.15 mA/cm^2 to 0.02 mA/cm^2. Therefore, (Ti,Cr)N grown at 190 °C give the better protective film than that growth at RT. In case of oxide film, after adding Ru into In_2O_3 to be $In_{1-x}Ru_xO_y$ film. The best condition found in thick ITO (150-nm)/ultrathin $In_{0.38}Ru_{0.62}O_y$ (3 nm) bilayers had an effective work function of 5.3 eV, high transmittance of 86%, and low specific resistivity of 9.2×10^{-5} Ω cm.

Department:	Metallurgical Engineering	Student's Signature	....
		Advisor's Signature	....
Field of Study:	Metallurgical Engineering	Co-Advisor's Signature	....
		Co-Advisor's Signature	....
Academic Year:	2014		

ACKNOWLEDGEMENTS

First and foremost I would like to thank you the Buddha's teaching words for giving me strength and endurance throughout of the course of this project. I thank my parents for never-ending supports throughout all hardships.

I would like to extend my special thanks to the following people who made this project possible:

1. Assoc. Prof. Patama Vissuttipitukul, Assoc. Prof. Gobboon Lothongkum, and Asst. Prof. Sukkaneste Tungasmita, who recommended this project, thank you for your valuable input, encouragement, guidance, and mentorship throughout the course of this project.

2. Mr. Somchai Taweesup and Piyavatin's family for your moral support all the time.

3. Prof. Chikyo and Dr. Nabatame for giving precious opportunity and excellent care of me during a great research course in Japan.

4. The members and junior of Department of Metallurgical Engineering, Faculty of Engineering Chulalongkorn University for always support throughout the course of this project.

5. The member of the International Center for Material Nanoarchitectonics (MANA) of the National Institute Materials Science, Japan. Part of this research was supported by CREST, JST.

6. The financial supports from the Thailand Research Fund and Chulalongkorn University through the Royal Golden Jubilee Ph. D Program (Grant No. PHD/0367/2550)

จุฬาลงกรณ์มหาวิทยาลัย
Chulalongkorn University

CONTENTS

Page

THAI ABSTRACT iv

ENGLISH ABSTRACT v

ACKNOWLEDGEMENTS vi

CONTENTS vii

REFERENCES 97

VITA 123

CHAPTER 1 Introduction and literature review 9

1.1 Surface modification 9

1.2 Objectives of dissertation 28

1.3 Scopes of investigation 28

1.4 Advantages of research 29

CHAPTER 2 Characterization techniques

2.1 Scanning electron microscopy (SEM) 30

2.2 Glancing incident angle X-ray diffractrometry (XRD) 31

2.3 Atomic force microscopy (AFM) 32

2.4 Nanoindentation 33

2.5 Scratch tester 34

2.6 Autolab PGSTAT 302N galvanostat/potentiostat 35

2.7 Inductively coupled plasma atomic emission spectroscopy (ICP-AES) 40

2.8 Spectroscopic ellipsometer (M-2000^{TM} XLS-100 D2) 41

2.9 Four-terminal specific- resistance tester 42

2.10 Semiconductor parameter analyzer (Keithley 4200 SCS) 44

CHAPTER 3 DC sputtering deposition and mechanical properties of (Ti,Cr)N films

3.1 Introduction 47

3.2 Experimental procedure 48

3.3 Results and discussion 50

3.4 Summary of mechanical properties 63

จุฬาลงกรณ์มหาวิทยาลัย
CHULALONGKORN UNIVERSITY

CHAPTER 4 DC sputtering deposition and corrosion properties of (Ti,Cr)N films

4.1 Introduction 64

4.2 Experimental procedure 65

4.3 Results and discussion 67

4.4 Summary of corrosion resistance 79

CHAPTER 5 DC sputtering deposition of ruthenium (Ru) doped indium oxide (In_2O_3) as transparent conducting oxide film

5.1 Introduction 80

5.2 Experimental procedure 82

5.3 Results and discussion 86

5.4 Summary of electrical properties 95

CHAPTER 6 Conclusions 96

จุฬาลงกรณ์มหาวิทยาลัย
Chulalongkorn University

LIST OF FIGURES

Figure 1.1: Schematic of reactive sputtering 10

Figure 1.2: Schematic of magnetron sputtering cathode 11

Figure 1.3: Polarization curves of ordinary and duplex TiN coating deposited on to AISI 304 substrate in a solution of 0.1 M H_2SO_4 + 0.05 M HCl 14

Figure 1.4: TiN coated SS410, (a) TiN coating surface, (b) Cross-sectional view of TiN coating on SS410, (c) Cross-section view of TiN coating on SS410 15

Figure 1.5: Elements in the periodic table that react together to from the max phase 16

Figure 1.6: Cross-sectional SEM micrographs of single (a) TiN (b) CrN coatings. 18

Figure 1.7: Structure Zone Model by Thorton 20

Figure 1.8: Resistivity of ITiO film with variation of Ar gas pressure 23

Figure 1.9: Optical transmittance spectra of ITiO film with different Ar gas pressure 23

Figure 1.10: Flat-band voltage as a function of EOT for Ru gate MOS capacitor with SiO_2. Three capacitors were the As-deposited (square), Oxidation (circle) and Reduction (triangle) 26

Figure 1.11: TiN deduced surface roughness of CoCr biomedical (a) CoCr film (b) surface roughness after adding TiN into CoCr film 27

Figure 1.12: In_2O_3 deduced surface roughness of TiO_2 (a) TiO_2 film (b) surface roughness after adding In_2O_3 into TiO_2 film. 27

Figure 2.1: Schematic of the scanning electron microscope 30

Figure 2.2: X - ray diffraction (a) Bragg's Law and the structure of NaCl 31

Figure 2.3: The X-ray spectrometer 31

Figure 2.4: Principle of operation of the AFM. 33

Figure 2.5: Nano-indentation Tester 34

Figure 2.6: Revetest Scratch Tester 34

Figure 2.7: PGSTAT 302N for corrosion testing 35

Figure 2.8: Impedance experiments: sinusoidal voltage input *V* at a single frequency *f* and current response *I*. 36

Figure 2.9: Impedance data representations: (A) Lissajous figure; (B) Complex impedance plot**.** 38

Figure 2.10: EIS show the result in 3D projection. 39

Figure 2.11: EIS equivalent circuit model. 40

Figure 2.12: Atomic emission spectroscopy: a schematic summary of how analytical results are obtained from a sample 41

Figure 2.13: Atomic emission 41

Figure 2.14: Measurement principle of ellipsometry 42

Figure 2.15: Arrangement of a four-point probe on rectangular sample 43

Figure 2.16: MOS Structure 45

Figure 2.17: C-V Characteristic of a MOS Structure 46

Figure 2.18: Carrier Distribution of a MOS Structure 46

Figure 3.1: AISI H13 samples after PVD sputtering: (a) CrN, (b) TiN 50

Figure 3.2: Co-deposition sample growth at room temperature (a) film color (b) composition by EDS, (c) cross-sectional film. 52

Figure 3.3: XRD pattern of PVD sample of CrN, TiN, and (Ti,Cr)N 52

Figure 3.4: Hardness of CrN, TiN, and (Ti,Cr)N film tested by Nano-indentation 53

จุฬาลงกรณ์มหาวิทยาลัย
Chulalongkorn University

Figure 3.5: AFM image of film growth at room temperature: (a) CrN film roughness, (b) TIN, and (c) (Ti,Cr)N film roughness. 55

Figure 3.6: Distance and critical load of scratch testing (L_{c1}, L_{c2}) which film growth at room temperature. 55

Figure 3.7: Co-deposition sample growth at 190°C (a) film color (b) Composition by EDS, (c) Cross-sectional film. 56

Figure 3.8: XRD profiles of coated samples at different growth temperatures 57

Figure 3.9: SEM image of cross-section PVD film (a) 190 °C, (b) room temperature 58

Figure 3.10: Representative load of final depth of (Ti, Cr)N at difference growth temperatures 59

Figure 3.11: Hardness of (Ti,Cr)N films growth at RT, 130°C, and 190 °C tested by Nanoindentation. 61

Figure 3.12: Scratch track (a) (Ti,Cr)N at RT, b) (Ti,Cr)N at 190 °C. 62

Figure 3.13: Distance and critical load of scratch testing (L_{c1}, L_{c2}) which film growth at RT, (Ti,Cr)N at 130 °C, and (Ti,Cr)N at 190 °C 62

Figure 4.1: SEM image of cross-sectional (Ti,Cr)N films (a) at 190 °C, (b) at RT 68

Figure 4.2: Anodic Polarization curves of (Ti, Cr)N film at different growth temperature 70

Figure 4.3: Nyquist plot of the (Ti,Cr)N film at difference growth temperature 72

Figure 4.4: Nyquist plot shows two semi-circles of the (Ti,Cr)N film at RT 73

Figure 4.5: Bode plots of (Ti,Cr)N film at different growth temperature 73

Chulalongkorn University

Figure 4.6: Bode plots of the (Ti,Cr)N film at 190ºC - grown temperature
at various immersion times. 75

Figure 4.7: EIS equivalent circuit model of the (Ti,Cr)N film at (a) 190ºC-grown film, (b) 130ºC- grown film (c) RT- grown film in 3.5% NaCl solution.
Sol and Sub means solution and steel substrate, respectively 76

Figure 4.8: SEM images of (a) RT-grown film, (b) 190 °C-grown film
after polarization test. 78

Figure 5.1: P-type Si with a 100-nm-thick SiO_2 layer samples after PVD sputtering:
(a) In_2O_3, (b) RuO_2. 83

Figure 5.2: Fabrication of: (a) MOS capacitor (b) Pattern no. 80 of
MOS capacitor. 85

Figure 5.3: XRD patterns of $In_{1-x}Ru_xO_y$ thin films on SiO_2/Si substrates. Ru content was varied from 0 to 1.0. 88

Figure 5.4: AFM images of as-grown films of (a) In_2O_3, (b) RuO_2, (c) $In_{0.95}Ru_{0.05}O_y$, and (d) $In_{0.38}Ru_{0.62}O_y$. 88

Figure 5.5: (a) Transmittance of 150-nm-thick as-grown films of In_2O_3, $In_{0.95}Ru_{0.05}O_y$, $In_{0.38}Ru_{0.62}O_y$, and RuO_2. (b) Transmittance of $In_{0.38}Ru_{0.62}O_y$ films as a function of thickness from 1 to 10 nm, a 150-nm-thick ITO film, and an ITO (150 nm)/ ultrathin $In_{0.38}Ru_{0.62}O_y$ (3 nm) bilayer. 89

Figure 5.6: Specific resistivity of In_2O_3, RuO_2, $In_{0.95}Ru_{0.05}O_y$, $In_{0.38}Ru_{0.62}O_y$,
and ITO (150 nm)/ ultrathin $In_{0.38}Ru_{0.62}O_y$ (3 nm)bilayer as a function of
annealing temperature in 3% H_2 atmosphere 90

Figure 5.7: The specific resistivity and transmittance as a function of
Ru content in the 150-nm $In_{1-x}Ru_xO_y$ thin films. 91

Figure 5.8: Representative C-V curves for 150-nm-thick $In_{0.38}Ru_{0.62}O_y$-gated MOS capacitors with SiO_2 layers of different thicknesses 93

Figure 5.9: Relationship between V_{fb} and EOT of In_2O_3, RuO_2, $In_{0.95}Ru_{0.05}O_y$, $In_{0.38}Ru_{0.62}O_y$, and ITO (150 nm)/$In_{0.38}Ru_{0.62}O_y$ (3 nm) films. 94

จุฬาลงกรณ์มหาวิทยาลัย
CHULALONGKORN UNIVERSITY

LIST OF TABLE

Table 1.1: A list of the Max phase, in both bulk and thin film form 16

Table 1.2: Deposition condition and mechanical properties of

$Ti_{1-x}Al_xN$ films 17

Table 1.3: Visual inspection records from immersion testing in 0.5 NaCl 19

Table 3.1: PVD magnetron sputtering parameters 49

Table 3.2: Final depth, h_f, measured at same displacement 60

Table 4.1: Chemical composition of AISI H13 steel 66

Table 4.2: Tafel calculation data of (Ti,Cr)N film prepared at different

growth temperature 70

Table 4.3: EIS data obtained by equivalent circuit simulation of the (Ti,Cr)N film

at different growth temperatures. 77

Table 4.4: BET surface analysis of (Ti,Cr)N at 190 °C-grown film

and RT-grown film. 78

Table 5.1: PVD magnetron sputtering parameters of oxide films. 83

Table 5.2: Co-sputtering conditions and $In_{1-x}Ru_xO_y$ composition 84

Table 5.3: Characteristics of $In_{1-x}Ru_xO_y$ and ITO (150 nm)/$In_{0.38}Ru_{0.62}O_y$ (3 nm)

films. 94

CHAPTER 1
INTRODUCTION AND LITERATURE REVIEW

1.1 Surface modification

Currently, surface coating has become a popular technique. The hard coating originated from the two deposition processes, physical vapor deposition (PVD) and chemical vapor deposition (CVD). At present, hard coating deposition on substrate can be done by several process such as physical vapor deposition (PVD), chemical vapor deposition (CVD), evaporation, and spay pyrolysis etc. In present, physical vapor deposition (PVD) has become a well-known process and a preferable process to produce hard coating in the coating industries due to no effect to matrix of materials and its low environmental burden.

1.1.1 Physical Vapor deposition (PVD)

PVD is a part of vacuum deposition method which is used to deposit thin hard coating film on materials. The terms "physical vapor deposition" seem to have been beginning since 1996 [1]. The hard coating can be formed on substrate by the condensation of a vaporized form of the ceramic or metal target on to various work piece surface. PVD is a well-known process which used to prepare hard coating with desired film properties. The hard coating is utilized for protective coating of surface materials from corrosion environment such as AlN, CrN etc. In addition, nitride and carbide hard coating were employed to resist abrasive wear because of its high hardness. There are several techniques of PVD process such as evaporative deposition, cathodic arc deposition and sputtering deposition and so on.

จุฬาลงกรณ์มหาวิทยาลัย
Chulalongkorn University

Sputtering is a technique used to create vapor for thin film deposition of materials on to surface or substrate. An importance advantage of sputter technique is that material with high melting points can be easily sputtered. Films were produced by sputter technique have a composition close to that the source target including with having a better adhesion on substrate (lower macro-particles) than evaporated films. Therefore, sputtering technique was selected to fabricate hard coating contains various properties requirement in this research. Sputtering technique is divided into two types: direct and reactive sputtering. Direct sputtering was widely used in industry but there are some problems concerning expensive ceramic target and discrepancy in chemical compositions. Therefore, reactive sputtering is a better choice for replacement to avoid those drawbacks. Reactive sputtering is a common process used to fabricate compound thin film coating on a wide variety of different substrate and produce correctness chemical composition of film. Direct and reactive sputtering will be discussed on the next section. Fig. 1.1 shows a system of typical reactive sputtering process.

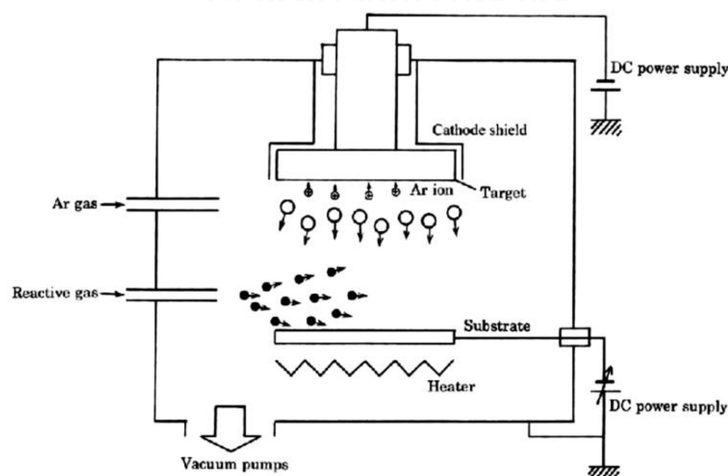

Fig. 1.1 Schematic of reactive sputtering [2]

Fig. 1.1, metals (e.g., Cr, Al, Cu and Ti) were used as a sputtering target in reactive gas atmosphere (O_2, N_2, CO_2 etc.) to form ceramics film on the substrate. Sputtering source for thin film deposition can be categorized in two ways: glow discharge (diode, triode and magnetron) and ion beam. In this research, magnetron sputtering was used because of its high deposition rate and there is easily to control the chemical compositions of the deposited film.

In magnetron sputtering, magnet is placed behind the sputtering source or target in order to control electron movement resulting in higher ionization efficiency. This can increase amount of sputtering ions resulting in increasing of deposition rate (Fig.1.2)

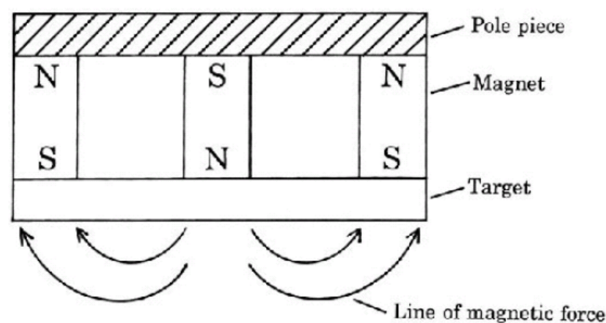

Fig. 1.2 Schematic of magnetron sputtering cathode. [1]

จุฬาลงกรณ์มหาวิทยาลัย
CHULALONGKORN UNIVERSITY

1.1.2 Sputtering

Sputtering technique was used to deposit thin films of a desired material on a work piece surface. At the beginning, gaseous plasma is created and then the ions from this plasma are accelerated into some source material or target. The target is eroded by the arriving ions via energy transfer hence, atoms at surface are ejected in form of neutral particles, molecules etc. [3] As these neutral particles are ejected they will travel in the chamber and come into contact with other particles or a nearby surface. If a substrate is placed in the path of these ejected particles it will be coated by a thin film

of the source material. The sputtering technique can be produced the film with different compositions. These film were fabricated from direct sputtering and reactive sputtering method.

1.1.3 Direct sputtering method

Thin films are deposited by direct sputtering method for applications in industries by using several ceramic targets. Ceramic film such as oxides, nitrides, and carbides can be grown by magnetron sputtering techniques from a compound target of desired composition. Sputtering by using compound target is a complicated way because it's hard to control chemical composition of deposition film due to different in physical properties. Moreover, experience with compound targets showed a number of disadvantages; the expensive ceramic target and the most importance problem is hard to control film compositions. The complexity of deposition thin film from compound target is reported in previously literatures. For example, composition in the films have large deviation from the sputtering source [4-7] .

To overcome these disadvantages, reactive sputtering is applied to produce thin film deposition. Reactive sputtering was introduced since 1953 and was employed to deposit hard coatings on tools until they became commercially available technique in the early 1980.

1.1.4 Reactive sputtering method

Reactive sputtering is normally used to fabricate compound thin films. Thin film was deposited on substrate by sputter from metallic (not nonmetallic) targets. The target of one chemical composition (e.g. elemental Ti) is sputtered in the presence of a reactive gas atmosphere (e.g. O_2, $Ar+N_2$). After that, the reaction took place and then formed

coating with different chemical composition (e.g. compound TiO_2). Argon gas is always used as main gas introduced into a chamber. Reactive gas is a type of gas which undergoes chemical reactions with materials in contact. Gases that are inert in ambient condition (e.g. molecular N_2) become reactive when present in plasma discharge due to collisions with energetic particles and subsequent dissociation into excited atomic neutral and charged components. The reactive sputtering method is often employed to fabricate various hard coating type. Oxides films were produced from O_2 as reactive gas, for example Al_2O_3, SiO_2, In_2O_3 and TiO_2 [8-11]. The applications of oxide film was applied to semi-conductor materials. Nitride film were produced from N_2 or ammonia as reactive gas. Types of nitride films are Si_3N_4, TiN, CrN, and AlN [12-15]. The nitride film are wildly used in machine part, milling cutter, plastic mould, and punching etc. Carbide film were produced from methane, acetylene and propane as reactive gas for example TiC, WC, and SiC [16-18]. Finally, sulfides film was produced from H_2S gas. Reactive sputtering give various film types and small deviation of film compositions can be obtained.

จุฬาลงกรณ์มหาวิทยาลัย
CHULALONGKORN UNIVERSITY

1.1.5 Nitride films

Nitride films are interesting thin films to modify surface of materials because their properties and applications. Many types of nitride films were applied in machine parts, drilling tools, and moulds in plastic transformation for matrix prevention in order to extend lifetime by minimize wear and corrosion. In service lifetime under severe corrosion and abrasion environment. Surface modification is an interesting method for improving both corrosion and mechanical properties. TiN, CrN and ZrN films are the keys and they had been developing until now [19-21]. Although, they are the answer as protective layers of those equipment, they are some drawback.

S. Rudenja et al.[22] studied corrosion behavior of AISI 304 stainless steel after duplex treatment, which consist of pre- nitriding followed by TiN coating. They stated that duplex TiN coating had lower corrosion resistance than the nitride substrate as shown in Fig.1.3 Lower corrosion resistance of duplex treatment and PVD samples is due to defects such as "pinholes". The pinhole may act as an area for initiation of localized corrosion.

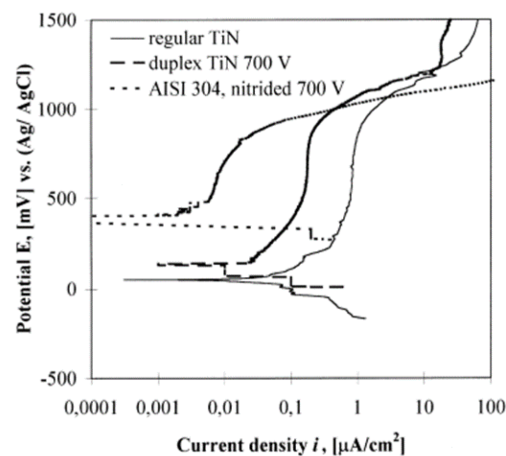

Fig. 1.3 Polarization curves of ordinary and duplex TiN coating deposited on to AISI 304 substrate in a solution of 0.1 M H_2SO_4 + 0.05 M HCl [22]

จุฬาลงกรณ์มหาวิทยาลัย
Chulalongkorn University

The TiN film normally exhibits a columnar growth and contains micro-pores as shown in Figure 1.4 [23]. These pores can be considered as defects of film which permit solution penetration to the substrate resulting in corrosion under the film [24-27] with a lot of voids in film, adhesion can be reduced due to decreasing contact surface area between film and substrate [28].

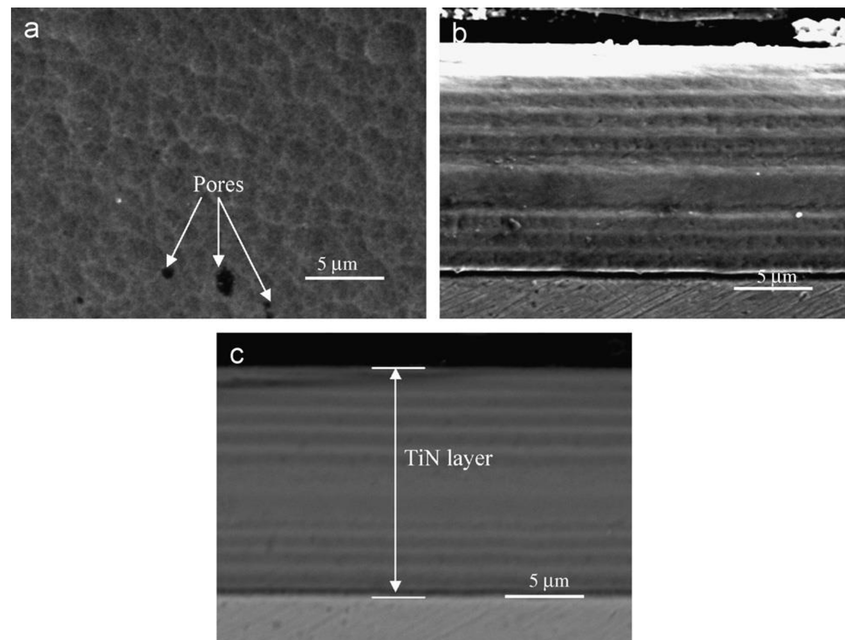

Fig. 1.4 TiN coated SS410, (a) TiN coating surface, (b) Cross-sectional view of TiN coating on SS410, (c) Cross-section view of TiN coating on SS410 [23].

Although, TiN film contains a lot of pores, their advantages could be seen. TiN film had both high hardness and high endurance in scratch as shown in previously research [29]. Therefore, TiN films is a popular film type used to protect surface of cutting and sliding tools. Moreover, TiN film was developed for decoration work due to its beautiful color.

In order to create an excellent performance of TiN film, (few pores, dense film, and high corrosion resistance) adding third elements into TiN film is interesting way. Currently, the ternary compound was synthesized and fully characterized as known as MAX phase. The MAX phase are layer which formed of ternary carbides or nitrides with the general formula $M_{n+1}AX_n$, where n = 1 to 3, m is an early transition metal, A is an A-group element (mostly IIIA and IVA, or group 13 and 14), and X is C and/or N (Fig.1.5). The list of Max phase was characterized as shown in Table1.10. These

characteristic film of the MAX phase promising candidates for many industrial applications, e.g., at high temperature and/or corrosion environment etc.

Fig. 1.5 Elements in the periodic table that react together to form the MAX phase [30]

Table 1.1 list of the max phase, in both bulk and thin film form. [31]

211 Phase	312 Phase	413 phase
Ti_2CdC, Sc_2InC, Ti_2AlC, Ti_2GaC, Ti_2InC, Ti_2TlC, V_2AlC,	Ti_3AlC_2,	Ti_4AlN_3,
V_2GaC, Cr_2GaC, Ti_2AlN, Ti_2GaN, Ti_2InN, V_2GaN, Cr_2GaN,	V_3AlC_2,	V_4AlC_3,
Ti_2GeC, Ti_2SnC, Ti_2PbC, V_2GeC, Cr_2AlC, Cr_2GeC, V_2PC,	Ti_3SiC_2,	Ti_4GaC_3,
V_2AsC, Ti_2SC, Zr_2InC, Zr_2TlC, Nb_2AlC, Nb_2GaC, Nb_2InC,	Ti_3GeC_2,	Ti_4SiC_3,
Mo_2GaC, Zr_2InN, Zr_2TlN, Zr_2SnC, Zr_2PbC, Nb_2SnC, Nb_2PC,	Ti_3SnC_2,	Ti_4GeC_3,
Nb_2AsC, Zr_2SC, Nb_2SC, Hf_2InC, Hf_2TlC, Ta_2AlC, Ta_2GaC,	Ta_3AlC_2,	Nb_4AlC_3,
Hf_2SnC, Hf_2PbC, Hf_2SnN, Hf_2SC		Ta_4AlC_3,

For example, TiN film was improved properties by add aluminum to form the ternary compound as (Ti,Al)N, which was studied as shown in the Max phase. Material properties were changed due to ternary compound. Ternary compound makes lattice

becomes more complex and/or change the crystal structure. Ternary film compound can be a single-phase solid solution [32, 33]. P.W. Shum et al. [34] reported that (Ti, Al)N film has superior mechanical properties than TiN film as showed in Table 1.2

Table 1.2 Deposition conditions and mechanical properties of $Ti_{1-x}Al_xN$ films [34]

Samples	Ti target current (A)	Al target current (A)	Hardness (GPa)	Elactic modulus (GPa)	$\lvert E_f - E_s \rvert$ [a]	L_{C1} (N) [b]	L_{C2} (N) [b]	Indentation tests [c]
TiN	5	0	230	245	55	>90	32	HF1
$Ti_{0.91}Al_{0.09}N$	5	1	25.4	263	38	>90	45	HF1
$Ti_{0.83}Al_{0.17}N$	5	2	26.1	277	24	>90	47	HF1
$Ti_{0.75}Al_{0.25}N$	5	3	27.3	288	12	>90	52	HF1
$Ti_{0.67}Al_{0.33}N$	5	4	27.3	296	5	>90	55	HF1
$Ti_{0.59}Al_{0.41}N$	5	5	31.4	312	12	>90	53	HF1
$Ti_{0.52}Al_{0.48}N$	5	6	28.5	305	4	55	29	HF2
$Ti_{0.43}Al_{0.57}N$	5	7	26.4	289	11	42	21	HF3
AlN	0	7	13.8	180	120	29	12	HF5
M42	–	–	12.0	301	–	–		–

[a] The difference of elastic modulus between $Ti_{1-x}Al_xN$ films (E_f) and M42 substrates (E_s).
[b] L_{C1} is defined as the load where the substrate is revealed on the scratch track, whereas L_{C2} is defined as the load where the first chipping occurs.
[c] HF1–HF6: HF1–HF3 define a sufficient adhesion whereas HF4–HF6 represent insufficient adhesion

Not only mechanical properties of (Ti,Al)N film were improved but also corrosion properties. L. Cunha et al. [35] reported that (Ti,Al)N film give corrosion rate (I_{corr}) $\sim 4.3 \times 10^{-4} \mu A/cm^2 - 1.6\ \mu A/cm^2$, depending on grown film method which is lower than that of uncoated samples. This result shows the same trend with other researches [36-38]. In addition, the best corrosion protection found in fine grained coating.

From results above, improving of TiN film properties can be done by the same idea by adding third element into TiN film. Therefore, we focus on element which successfully support these properties: high hardness, high endurance scratch, high corrosion resistance, and smooth surface. The interesting element is chromium and/or chromium nitride (CrN). CrN film is increasingly used in tribology applications, automotive components, and forming dies because CrN film exhibit superior ductility, dense film, and corrosion resistance [39-42]. Research was studied by C. Liu et al. [43], states that CrN film succeed to improve corrosion resistance owing to their dense

non-columnar structure and contained a mixture of three phases: Cr (b.c.c.), Cr_2N (hexagonal) and CrN (f.c.c.) as show in Fig.1.6

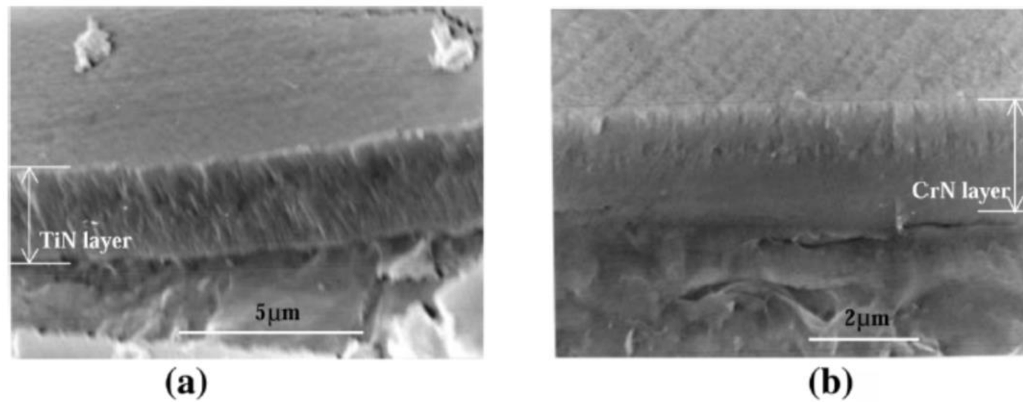

Fig. 1.6 Cross-sectional SEM micrographs of single (a) TiN (b) CrN coatings[43]

Minor of corrosion appeared in CrN coated steel during electrochemical tests in aqueous salt solution meanwhile severe corrosion occurs on TiN coated after the same periods of immersion. For example, after 3.5 days exposure, there is heavy rust spreading from the site of localized corrosion of TiN, but very little rust in the pit could be seen of CrN as show in the Table 1.3. The high performance of corrosion resistance which observing in CrN is as might be expect from their microstructure. Dense film and non-columnar structure of CrN coating yields much better corrosion resistance than TiN. Therefore, we would like to purpose combining of CrN and TiN to be (Ti,Cr)N film with controlling growth parameters for control film microstructure in order to get novel nitride film. This film is aimed to have of high corrosion resistance, high hardness, high adhesion and low surface roughness.

Table 1.3 Visual inspection records from immersion testing in 0.5 NaCl [43]

Immersion time	TiN/MS	CrN/MS
50 min	Trace of pits (white points) surrounded with dark gold	Trace of pits (white points) surrounded with dark grey
3 h	Several pits extended, one of them severely developed, numbers slightly increased	Slightly extended, all pits developed almost evenly, numbers apparently increased
0.5 day	Pits further propagated badly, became black points	Pits remained, but more new pits initiated
1.5 days	Rust plugged and spread out, new pits initiated	Little rust, no spread More pits growing
3.5 days	Rust piled up to cover exposed area, locally delaminated	Almost remained unchanged, slightly rust coverage
7 days	Spreading rust, overall coverage, continual plugging	Insignificant plugging, pit propagation retarded

There are several ways to reduce pores: Increase the coating thickness, modification the film structure from columnar to equiaxed, controlling the bias potential during film deposition, and multilayering. In this research, we intend to modify the film structure by controlling growth parameters. Growth parameters depend on substrate temperature and deposition rate [44-49]. The substrate temperature is an interesting parameter to study because the substrate temperature strongly result in three different modes of the film growth as following below.

1. Volmer-Weber mode (island growth): small clusters are nucleated directly on the substrate surface and then grown to be islands of the condensed phase. Atoms (or molecules) of the deposit are more strongly bound to each other than to the substrate.

2. Frank-van der Merwe mode (layer-by-layer growth): displays the opposite from. Atoms are more strongly bound to the substrate than to each other, the first atoms to condense form a complete monolayer on the surface.

3. In Stranski - Krastanov mode after forming the first monolayer subsequent layer growth is unfavorable and islands are formed on top of this ‘intermediate’ layer. There are many possible reasons for this mode to occur, and almost any factors which disturb the monotonic growth decrease in binding energy, characteristic of layer growth, may be the cause. For example, the lattice parameter or crystal orientation in

the intermediate layer may not be able to grow into film. This results in a high free energy of the deposit intermediate-layer interface which favors subsequent island formation.

The film microstructure depends on the growth parameters. By controlling of film microstructure, we can obtain desirable properties such as mechanical properties and electrical properties. The microstructure of sputtered film is usually classified into four zones [50] as shown in Fig.1.7

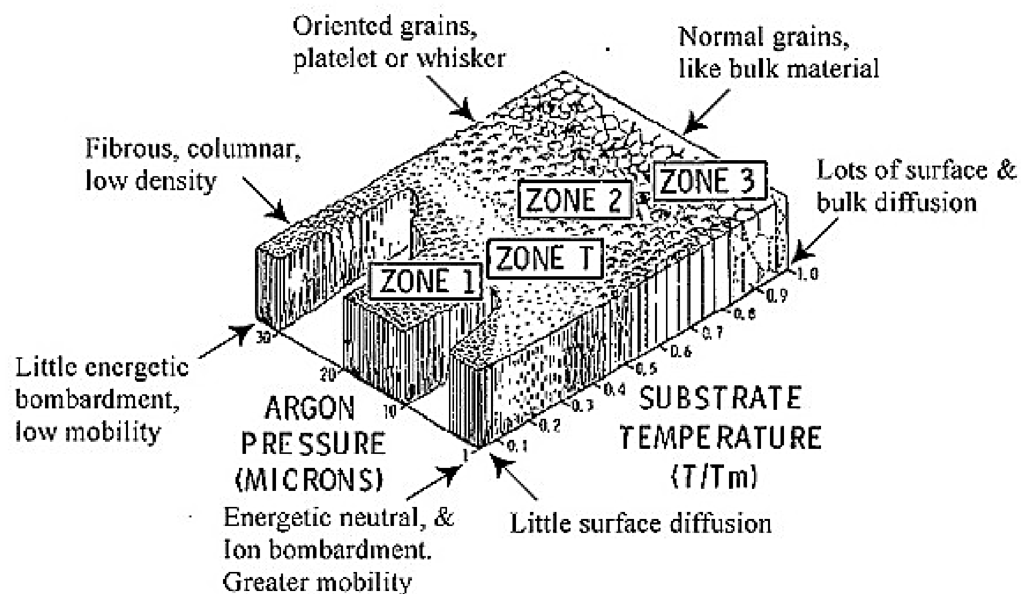

Fig. 1.7 Structure Zone Model by Thorton [50, 51]

Zone 1 structure, composes of tapered columns and significant voids between columns, which the ratio T/T_m is less than about 0.3, where T is the growth temperature and T_m is the melting point of the deposited material with this low temperature, the diffusion of adatoms is very limited. Zone 1 structure tends to be associated with rough surface, pores stability, and properties that are far from those of the bulk material [52]. Zone 2 is usually found when $0.3 < T/T_m < 0.5$, which is associated with adatom diffusion on grain surface. Zone 2 structure consists of columnar, platelet, or whisker

grains separated by dense intercrystalline boundaries surface is smoother that those films in zone 1 structure. In many compound semiconductors, an optimum growth situation is necessary due to structure sensitive properties, such as surface smoothness[53]. Zone 3 occurs at high temperature, T/T_m >0.5, enhancing diffusion in both surface and bulks diffusion. For zone 3, diffusion within the grains or bulk diffusion can be considered as a main mechanism of film growth. Therefore, zone 3 is associated with equiaxied grains and epitaxial growth on the substrate. By elevating the substrate temperature during film growth, semiconductor material such as GaAs and Si have been epitaxial grown [54]. The "transition" zone (zone T which located between zone I and II), is the result of bombardment induced surface mobility. Films that would have been expected to be Zone 1 structure on the basis of T/T_m can be grown with a very smooth surface and high density by bombarding the growing film with energetic particles during film growth [29, 55-60]. The main bombarding species of importance in the case of magnetron source are ions and energetic neutrals. The latter species originate from the target either as positive ions neutralized or reflected from the target surface[61], or as sputtered negative ions that are accelerated in the dark space and then neutralized in the gas[62] . Film material is moved into the spaces between grains by forward sputtering [28, 63] and by energy deposited locally by the bombarding particles (i.e., thermal spikes). This movement of material leads to tightly packed fibrous grains.

The corrosion resistance of single nitride film could be improved by add elements to form complex nitride; for example, adding Cr into TiN to form Cr-Ti nitride. Not only corrosion resistance, but also mechanical properties of metal nitride can be improved by formation of complex nitride instead of single element nitride. Complex nitride film can be prepared by co-deposition by using two or more metal type

in the same chamber during sputtering. It can be seen that adding metal element into metal nitride together with controlling parameter could be manage film properties not only chemical composition but also physical morphology of film as well.

1.1.6 Oxide films

A large number of researchers try to modify the properties of metal oxide film for a long time because metal oxide film have a wide range of applications in transparent semiconducting materials. Transparent conducting film are widely used to produce gas sensors, thin-films transparent transistors, planar displays, electro chromatography devices, solar cells, and anode material for organic electroluminescence, etc.[64]. The properties were required in transparent semiconducting film including of wide band gap energy 3.55-3.75 eV, good electrical conductivity, high work function, excellent in surface contact, and high transmittance in the UV region [65-67]. In recent years, many of methods for preparation indium oxide (In_2O_3)-based films have been developed and studied for application transparent semiconducting film.

จุฬาลงกรณ์มหาวิทยาลัย
Chulalongkorn University

An anode material in organic electroluminescence was fabricated by In_2O_3-based films. Currently, indium tin oxide ($In_{0.9}Sn_{0.1}O_y$, ITO) is the most attractive anode material. Previous research [68] reported that titanium was doped in In_2O_3 transparent conductive films; the results showed the lowest resistivity of 1.2×10^{-4} Ωcm (Fig.1.8) and average optical transmittance of 75% in the wave length range of the visible spectrum (Fig.1.9)

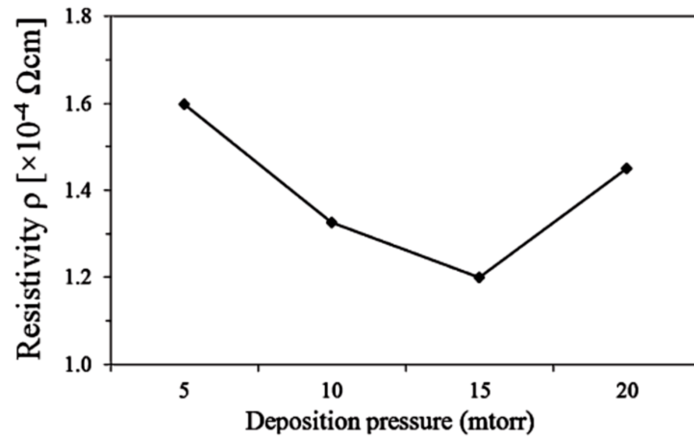

Fig. 1.8 Resistivity of ITiO film with variation of Ar gas pressure [68].

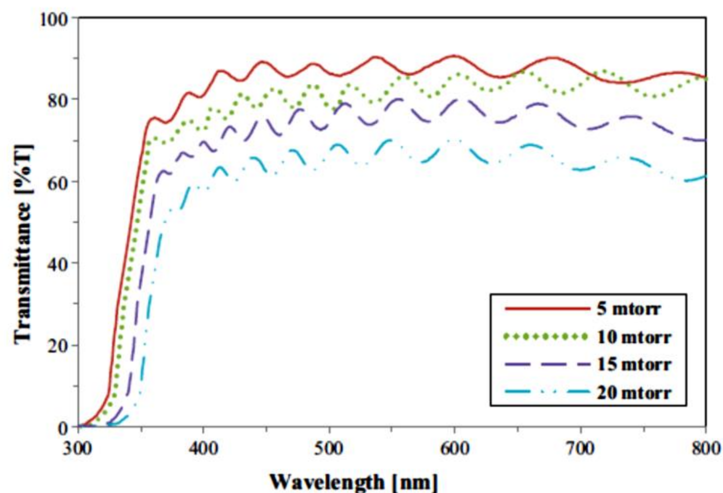

Fig. 1.9 Optical transmittance spectra of ITiO film with different Ar gas pressure [62].

However, ITO has a low work function of 4.7 eV [69]. The work function of anode material is required to be over 5 eV because the highest occupied molecular orbital of the hole transport layer is usually over 5 eV. In addition, anode with high work function can reduce the potential barrier allowing efficient hole carrier injection, which decrease the operating voltage of the device. For these reasons, several researchers proposed methods to improve work function of ITO together with developing new anode

material. Doping with high work function elements such as Mo, Ni, W, and Pt into In_2O_3 film is popular method to enhance high work function value [70-72].

There are several researches concerning metal-doping in In_2O_3 for anode materials. Elangovan et al. [70] studied doping of Molybdenum (Mo) into indium oxide (IMO) films by RF magnetron sputtering method using target consisted of In_2O_3 98 wt%: Mo 2 wt%. Films obtained wide range of work function as 4.61- 4.93 eV depending on oxygen partial pressure during sputtering. Although the highest work function obtained in this research was 4.93 eV, it was not sufficient for organic electroluminescence (OEL). Hence, other dopant elements could be more appropriate. J.H. Kim et al. [73] reported that the effective doping of Ni in In_2O_3 (INO) led to a work function of 5.02 eV after annealing by rapid thermal annealing (RTA) furnace at 600 °C. Although the high work function was found in INO, INO film exhibited excessive surface roughness (RMS about 2.89 nm). A Pt-W co-doped In_2O_3 thin film as the anode of OEL devices was also investigated to produce high work function value [74]. This method is successfully increase work function up to 5.5 ev, low electrical resistivity, and high transmittance, However, success of an excellent surface contact is not clarify. To archive excellent performance of operating voltage and luminescence of OEL devices, the surface contact of the interface between transparent conductive oxides film and organic layer must be considered. To increase surface contact, it can be done by decreasing degree of surface roughness of anode material. Chenet al. [75] reported that by surface roughness can be reduced since In_2O_3 could suppress the grain growth of TiO_2 crystals.

Recently, Ruthenium (Ru) is an interesting element for doping into In_2O_3 to increase work function since Ru has work function over the wide range of 4.6 -5.3 eV

[76-80]. In addition, T. Nabatame et al. [81] reported high effective work function value of Ru or RuO_2 after annealing in oxidation condition. The effective work function values of oxidation samples are estimated to be 5.58 ± 0.05 eV as show in Fig.1.10. However, detail of studies on the characteristic, both electrical and physical of Ru doped In_2O_3 ($In_{1-x}Ru_xO_y$) films have not been reported elsewhere. To obtain the oxide film use for anode material, oxide film must has low specific resistivity, high transmittance, high work function, and smoothness surface. Ruthenium is an interesting element to dope into In_2O_3 film. Alloying elements have a great an effect on properties both of nitride film and oxide film. Therefore, this research we would to add chromium in TiN film with controlling growth parameter (substrate temperature) for improving film properties for application in machine part, drilling, and cutting tools. Another purpose is add ruthenium in In_2O_3 film for improving their properties to obtain low resistivity, high work function, high transmittance and smoothness surface as apply for anode materials.

1.2 Effect of metal alloying on the films properties

CHULALONGKORN UNIVERSITY

PVD is a coating process used for improving the properties of materials. Major film properties, which we to achieve in industries, are high hardness such as TiN, ZrN, TiCN films with high wear resistance such as CrCN, CrAlN, TiAlN films and low friction coefficient such as h-BN, CN, MoS_2 films. However, there are some individual film properties which are currently studying in the laboratory scale due to limitation of each individual film for example; anti-reflective coating (ARC), corrosion resistance, self-cleaning and decoration.

TiN has good properties which are high hardness and high wear resistance but it has film porosity and high friction coefficient.

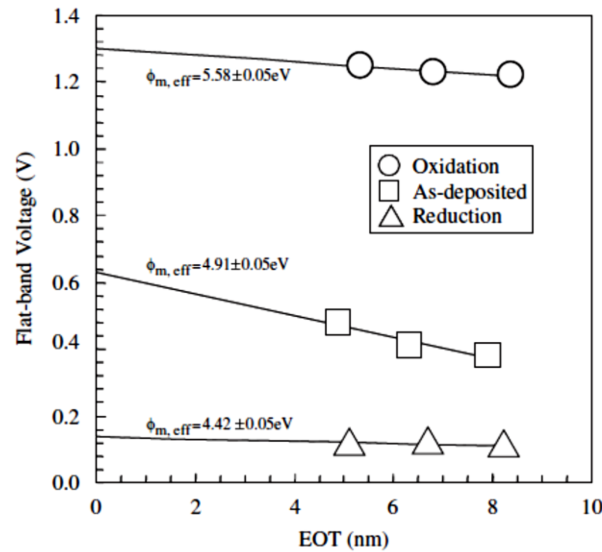

Fig. 1.10 Flat-band voltage as a function of EOT for Ru gate MOS capacitor with SiO_2. Three capacitors were the As-deposited (square), Oxidation (circle) and Reduction (triangle). [81]

AlN is a high density film with high corrosion resistance but it has low hardness and low wear resistance comparing to TiN. In order to combine these merits of two materials, Fabrication of ternary nitride by adding the third element is one option. After adding the third element, it is possible to get main properties similar to matrix with some strongly properties improved by third element [82-84]. In addition, it was found that properties of complex nitride or mixed phase depend on solubility, coating parameters and chemical compositions (stoichiometry) [32, 85-87]. Moreover, adding third elements provides indirect advantage since the third element can suppress grain growth of film, for example, add TiN in CoCr biomedical film [88] and add In_2O_3 in to TiO_2 film [75] as shown in Fig. 1.11 and Fig. 1.12 respectively. The surface roughness also decrease when grain growth was suppressed by adding the third element.

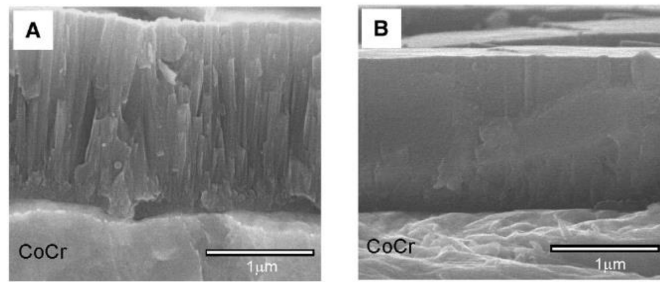

Fig. 1.11 TiN deduced surface roughness of CoCr biomedical (a) CoCr film (b) surface roughness after adding TiN into CoCr film.

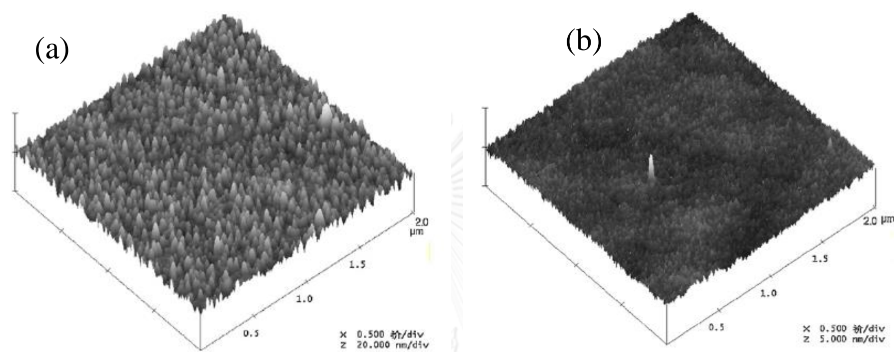

Fig. 1.12 In_2O_3 deduced surface roughness of TiO_2 (a) TiO_2 film (b) surface roughness after adding In_2O_3 into TiO_2 film.

Several advantages of adding the third element draw our attention to improve properties of coating film in order to improve mechanical properties, corrosion resistance, and electrical properties of film, therefore, improving of film properties by adding the third element into nitride film and oxide film is the aim of this research.

จุฬาลงกรณ์มหาวิทยาลัย
CHULALONGKORN UNIVERSITY

1.3 Objectives of dissertation

This research aims to improve properties of nitride and oxide film coated by sputtering. The key to improve properties of the coating film is to add the third element into nitride or oxide film.

Nitride film is normally used to improve surface hardness and wear resistance. Adding third element to achieve ternary nitride of (Ti,Cr)N at various coating conditions to improve mechanical properties and corrosion resistance is studied in this research.

For oxide film, electrical properties and surface morphology can be varied by adding the third element. In this research, ruthenium was added into indium oxide, surface morphology, structure and electrical properties of $In_{1-x}Ru_xO_y$ is investigated.

1.4 Scopes of investigation

The experiment will proceed as follow:

1.4.1 Co-depositions of transition metal coating films including TiN : CrN (Ti, Cr) N and In_2O_3: Ru (IRO) were performed by DC magnetron sputtering .

1.4.2 All coating layer, were characterized by Optical microscope (OM), Scanning electron microscope (SEM), Field emission scanning electron microscopy (FE-SEM), Glancing incident angle X-ray diffractrometer (GIXD) and Atomic force microscope (AFM).

1.4.3 Mechanical properties of nitride coating layer were studied by Nano-indentation hardness testing and Scratch adhesion tester.

1.4.4 Corrosion resistance of nitride coating layer were tested by Potentiodynamic Polarization method and the Electrochemical Impedance Spectroscopy (EIS).

จุฬาลงกรณ์มหาวิทยาลัย
Chulalongkorn University

1.4.5 Physical and electrical properties of oxide coating layer will be studied by Spectroscopic ellipsometer, Four-terminal specific resistance tester and Semiconductor parameter analyzer.

1.5 Advantages of research

1.5.1 To achieve the suitable transition- metal nitride film of protective layer for improving mechanical properties and corrosion resistance on AISI H13.

1.5.2 To achieve a new anode materials for application in organic electroluminescence.

จุฬาลงกรณ์มหาวิทยาลัย
Chulalongkorn University

CHAPTER 2

CHARACTERIZATION TEACHNIQUES

2.1 Scanning electron microscopy (SEM)

SEM is employed in microanalysis and failure analysis of solid materials. The signals generated during analysis reveal information about the sample, external morphology (texture), chemical composition (when used with EDS), and orientation of material sample. EDS component of the system is equipped with SEM analysis to determine amount of elements in the sample for qualitative information and/or to measure elemental compositions for semi-quantitative results. Other substances those are not organic in nature and coatings on metal can also be identified through EDS. A schematic of the typical SEM is shown in Figure 2.1

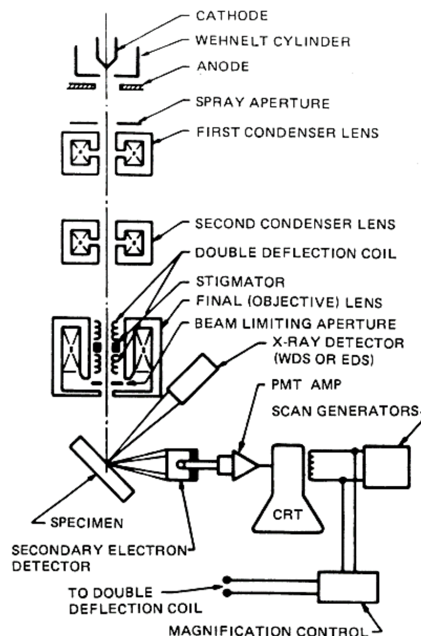

Fig. 2.1 Schematic of the scanning electron microscope. [89]

2.2 Glancing incident angle X-ray diffraction (GIXRD) and X-ray diffraction

X-ray are electromagnetic radiation with wavelength in the range of 0.5-0.25 Å. Because this is the same order of magnitude as the interatomic distance in solids, X-ray are used to study the internal (crystalline) structure of materials. The condition for constructive interference are easily derived from the simple geometrical picture for the scattering of an X-ray beam by planes of atoms in the crystal as shown in Figure 2.2 and Figure 2.3 The peak in an X-ray diffraction pattern are related to the atomic distances. Consideration an incident X-ray beam interaction with the atoms arranged in a manner as shown in two dimensions. The atoms, represented as back spheres, can be seen as pattern different sets of planes in the crystal. For a given set of lattice plane with an inter-plane distance of d, the condition for a diffraction (peak) to occur could be written as $2dsin\theta = n\lambda$ which is known as the Bragg's law.

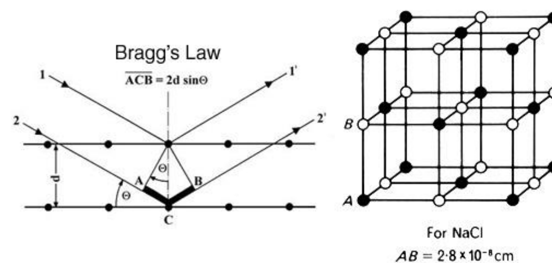

Fig. 2.2 X - ray diffraction (a) Bragg's Law and the structure of NaCl [90]

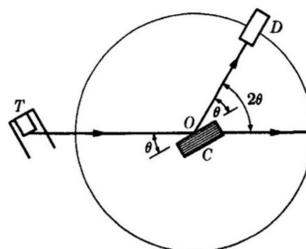

Fig. 2.3 The X-ray spectrometer [91]

The Bragg's law can be utilized into two ways. First, using X-rays with known wavelength λ and measuring θ for determination of spacing d of various planes in the crystal: this is structure analysis. Alternatively, using a crystal with planes of known spacing d, measure θ, and thus determine the wavelength λ of the radiation used: this is X-ray spectroscopy [91].

2.3 Atomic force microscopy (AFM)

The principle of AFM (Fig. 2.4) relies on a scanning technique to produce high resolution 3-D images of sample surface. The AFM measures ultrasmall forces (less than 1 nN) between the AFM tip surface and a sample surface. These small forces are measured by measuring the motion of very flexible cantilever beam with an ultrasmall mass [92]. Every variation of the surface height varies the force acting on the tip and therefore varies the bending of cantilever. This bending is measured by an integrated stress sensor at the base of the cantilever spring and recorded line by line in the electronic memory. The AFM can be used either in the static or dynamic mode. In the static mode, also referred to as the repulsive or contact mode [93], a sharp tip at the end of the cantilever is brought into contact with the surface of sample. During initial contact, the atoms at the end of the tip experience a very weak repulsive force due to electronic orbital overlap with the atoms on the surface of the sample. In the dynamic mode, also referred to as attractive force imaging or noncontact imaging mode, the tip is brought into close proximity to a few nanometers but not in contact with the sample. The cantilever is vibrated in either amplitude modulation (AM) mode [94] or frequency modulation (FM) mode [94-97] Very weak van der Waals attractive forces are present at the tip-sample interface.

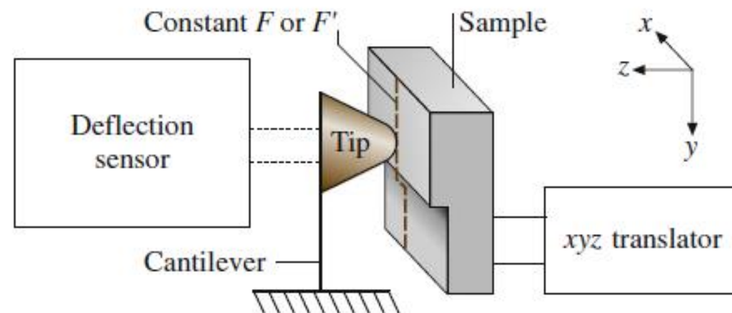

Fig. 2.4 Principle of operation of the AFM. [92]

2.4 Nanoindentation

PVD coating layer has the thickness in nanometer - micrometer range. In order to achieve the hardness of thin film coating without any effect from matrix, it is necessary to use nanoindentation testing. This technique has been designed to provide surface mechanical data by indenting to depths in nanometer-micron range as show in Fig 2.5. In this research, advance mode was employ to measure the hardness with controlling penetration depth up to100 nm from surface. Every measurement used loading-unloading rate of 30 mN/min and pressed 10 times. Young's modulus of coating layer was also calculated from nanoindentation test.

จุฬาลงกรณ์มหาวิทยาลัย
CHULALONGKORN UNIVERSITY

Fig. 2.5 Nano-indentation Tester [98]

2.5 Scratch tester

Adhesion of film was investigated by measurement of critical load to detect film from substrate. The critical load was measured by scratch adhesion tester as show in Figure 2.6. Measurement result showed scratch track and ability of adhesion between coating film and surface material as refer in ASTM C1624. The progressive mode from 1 N to 20 N with loading rate of 7600 mN/min was used to measure for 5 times by similar condition in this research.

จุฬาลงกรณ์มหาวิทยาลัย
CHULALONGKORN UNIVERSITY

Fig. 2.6 Revetest Scratch Tester [99]

2.6 Autolab PGSTAT 302N galvanostat/potentiostat

Samples were corrosion tested by PGSTAT 302N. Experiment was performed in 400 ml of 3.5% NaCl solution. The tree-electrode (potentiostatic) mode using an Ag/AgCl as a reference electrode and as a counter electrode platinum plate as show in Fig 2.7. Corrosion test was carried out at room temperature. The open-circuit potential (E_{ocp}) will be registered as a function of time during 30 min and anodic potential sweep with scan rate of 1 mV/s. The start potential and stop potential are -0.5V and 1.5 V respectively. Electrochemical Impedance Spectroscopy (EIS) is used to evaluate the electrochemical behavior of electrode and/or electrolyte materials. A multitude of fundamental microscopic process took place throughout the cell when it was electrically stimulated, and then showed the overall electrical response.

Fig. 2.7 PGSTAT 302N for corrosion testing

The analysis included the transport of electrons through the electronic conductors, the transfer of electrons at the electrode-electrolyte interface to form charged or uncharged atomic species which originate from the cell materials and its atmospheric environment (oxidation or reduction reactions), and the flow of charged atoms or atom agglomerates

via defects in the electrolytes. The flow rate of charged particles (current) depends on the ohmic resistance of the electrodes and electrolyte at the electrode-electrolyte interface [100].

The electrical resistance is the ability of a circuit element to resist the flow of electrical current. Ohm's law defines resistance in terms of the ratio between voltage, V and current, I.

$$R \equiv \frac{V}{I} \tag{2.1}$$

while this is a relationship, it's usage is limited to only one circuit element, the idea resistor. However, the realistic situation contains circuit elements that exhibit much more complicate with complex behavior. So, impedance (Z) can be measured to show the ability of a circuit to resist the flow of electrical current, but unlike resistance (R).

Electrochemical impedance is measured by applying an alternating current (AC) voltage to an electrochemical cell and then measuring the current through the cell as shown in Figure 2.8

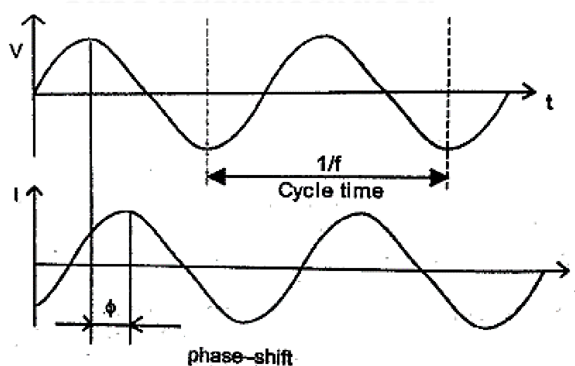

Fig. 2.8 Impedance experiments: sinusoidal voltage input *V* at a single frequency *f* and current response *I*. [101]

The electrochemical impedance is measured using excitation *AC* voltage signal *V* with small amplitude V_A (expressed in volts) applied at frequency *f* (expressed in Hz or

1/sec). The voltage V(t), expressed as a function of time t, can be written in form of [102] :

$$V(t) = V_A \sin(2\pi f t) = V_A \sin(\omega t) \qquad (2.2)$$

In this case a "radial frequency" ω of the applied voltage signal (expressed in radians/second) parameter is introduced, which is related to the applied AC frequency f as $\omega = 2\pi f$.

In a linear or pseudolinear system, the current response to a sinusoidal voltage input will be a sinusoid at the same frequency but "shifted in phase", that is defined by ratio of capacitive and resistive components of the output current (Fig.2.8). In a linear system, the response current signal I(t) is shifted in phase (Φ) and has a different amplitude, I_A:

$$I(t) = I_A \sin(\omega t + \Phi) \qquad (2.3)$$

An expression analogous to Ohm's Law allows to calculate the complex impedance of the system as the ratio of input voltage V (t) and output measured current I(t) as shown below:

จุฬาลงกรณ์มหาวิทยาลัย
CHULALONGKORN UNIVERSITY

$$Z^* = \frac{V(t)}{I(t)} = \frac{V_A \sin(\omega t)}{I_A \sin(\omega t + \Phi)} = Z_A \frac{\sin(\omega t)}{\sin(\omega t + \Phi)} \qquad (2.4)$$

Therefore, the impedance is performed in term of a magnitude (absolute value), $Z_A = |Z|$, and a phase shift, Φ. By plotting the applied sinusoidal voltage signal on the x-axis of graph and the sinusoidal response signal I(t) on the y-axis, an oval know as a " Lissajous figure" will appear (Figure 2.9 A).

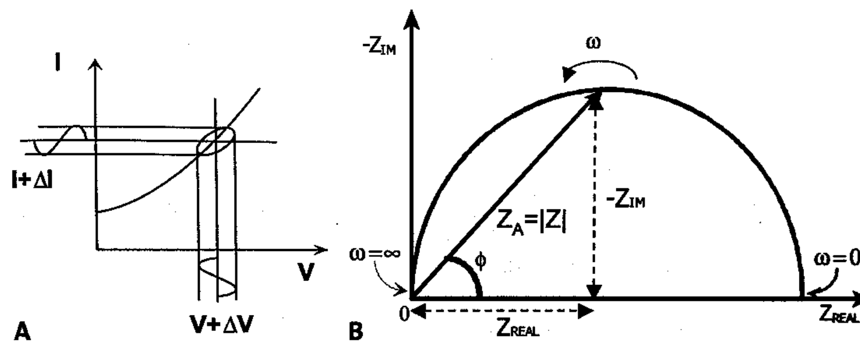

Fig. 2.9 Impedance data representations: (A) Lissajous figure; (B) Complex impedance plot [101].

Modern equipment permit automation in applying. The voltage input with variable frequencies and collecting. The output impedance (and current) responses as the frequency was scanned from very high (MHz –GHz) values while timescale of the signal was in micro-and nanoseconds to very low frequencies (μHz) with timescales of the order of hours.

Using Euler's relationship:

$$\exp(j\Phi) = \cos\Phi + j\sin\Phi \quad (2.5)$$

The impedance can be expressed as a complex function. The potential V (*t*) is described as:

$$V(t) = V_A e^{j\omega t} \quad (2.6)$$

and the current response is:

$$I(t) = I_A e^{j\omega t - j\Phi} \quad (2.7)$$

The impedance is represented as a complex number that can be expressed in complex mathematics as a combination of "real", or in-phase (Z_{REAL}), and "imaginary", or out-of-phase (Z_{IM}), part (Fig. 2.9 B) :

$$Z^* = \frac{V}{I} Z_A e^{j\Phi} = Z_A\,(cos\Phi + jsin\Phi) = Z_{REAL} + jZ_{IM} \quad (2.8)$$

and the phase angle Φ at a chosen radial frequency ω is a ratio of the imaginary and real impedance components:

$$\tan \Phi = \frac{Z_{IM}}{Z_{REAL}} \quad or \quad \Phi = \arctan \frac{Z_{IM}}{Z_{REAL}} \qquad (2.9)$$

Electrochemical Impedance Spectroscopy technique (EIS) result was exhibited in 3D projection as shown in figure 2.10 Nyquist plot is the relation between imaginary part (-Z″ (Ω)) of impedance and real part (Z′ (Ω)) of impedance. Bode modulus is the relation between real part (Z′ (Ω)) of impedance and frequency (Hz). Bode phase is the relation between frequency (Hz) and phase angle (°).

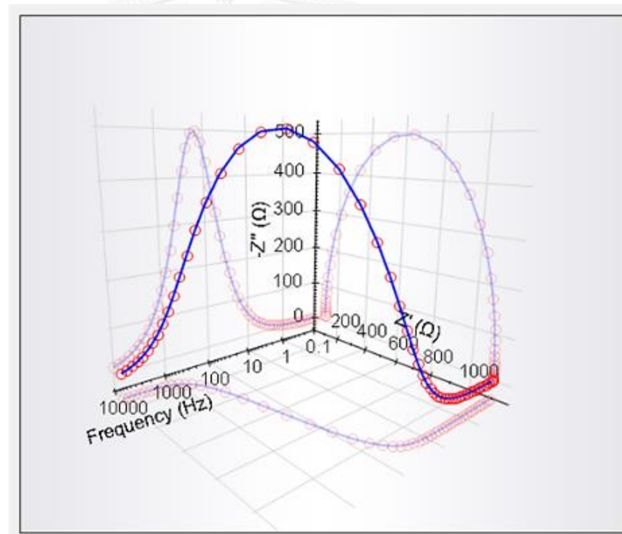

Fig. 2.10 EIS show the result in 3D projection.

Corrosion refers to electron loss from materials, hence, it relates to electricity. From the circuit of Fig 2.11, which is the example of EIS result we can lean the corrosion behavior of films during corrode in solution and/or investigation of diffusion mass transport at the interface by interpretation from circuit feature and parameter in the circuit. The definitions of each parameters are as following; solution resistance (R_e or R_{sol}) is the resistance to ionic migration current in aqueous bulk solution. Charge

transfer resistance of film (R_p or R_{CT}) is the pore electrical resistance to the ionic current through the pores. Constant phase element (CPE or Q) is non ideal capacitance. Diffusion impedance [O] is the diffusion mass transport process (finite diffusion case). Substrate resistance (R_s) is polarization resistance.

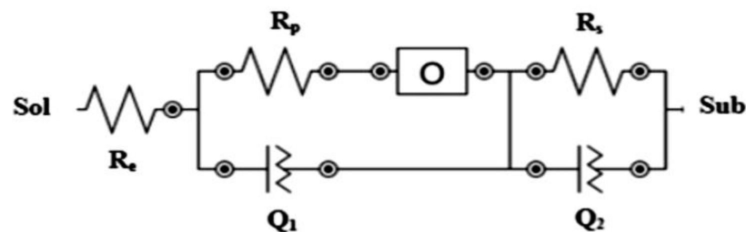

Fig. 2.11 EIS equivalent circuit model.

2.7 Inductively coupled plasma atomic emission spectroscopy (ICP-AES)

ICP-AES was used for the multi-element analysis of materials in gaseous, liquid, powdered, or solid state. Because of its high resolution and the increasing variety of excitation source available, AES is the most universally used method for multi-element analysis. There are many ways in which AES can be perform, and each of these ways has many variation. Generally, each method involves excitation, dispersion, detection, and data processing. The schematic summary as show in Fig. 2.12 and the chain of events leading form sample to emission is described in Fig 2.13 [103]

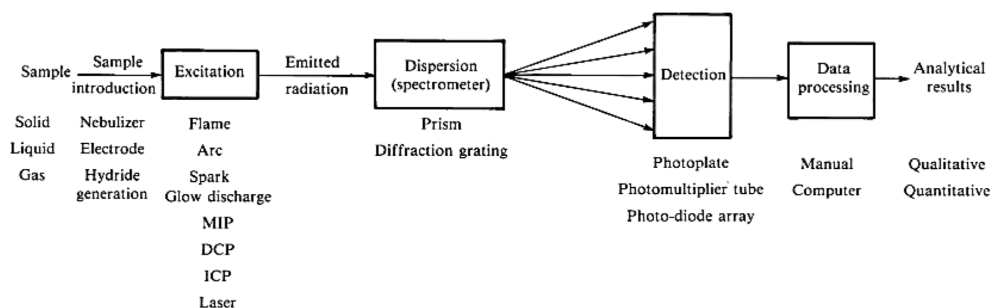

Fig. 2.12 Atomic emission spectroscopy: a schematic summary of how analytical results are obtained from a sample [103].

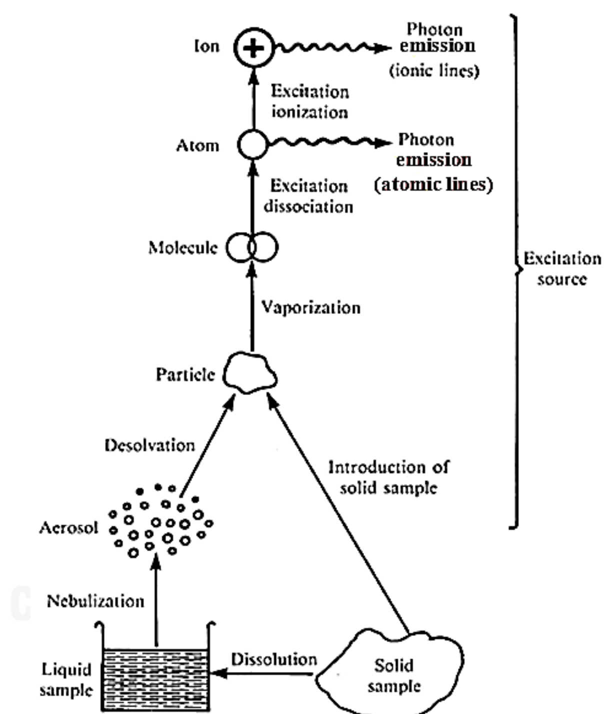

Fig. 2.13 Atomic emission [103]

2.8 Spectroscopic ellipsometer (M-2000^{TM} XLS-100 D2)

Ellipsometry is an optical measurement technique that characterizes light reflection (or transmission) from sample[104-107] The main feature of ellipsometery is that it measures the change in polarized light upon light reflection on a sample (or

light transmission by a sample). In spectroscopic ellipsometry, spectra are measured by changing the wave length of light. There is carried out in ultraviolet/visible region, but measurement in the infrared region has also been performed widely. For semiconductor characterization, the incidence angle is typically 70-80°. Note that, at normal incident, the ellipsometry measurement becomes impossible, since p- and s-polarization cannot be distinguished anymore at this angle. Figure 2.14 explain the measure principle of ellipsometry [108].

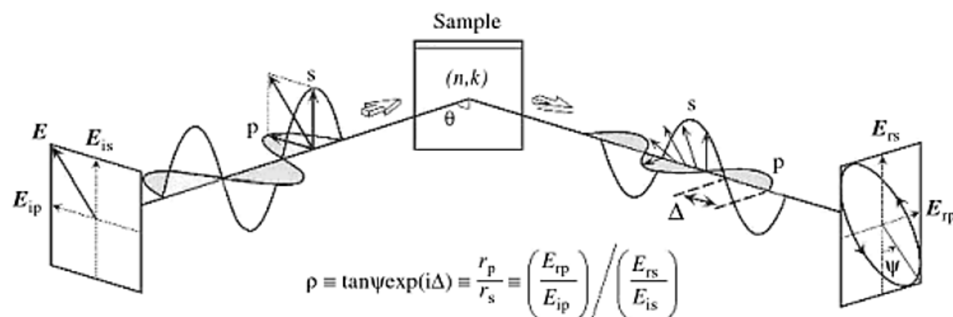

Fig. 2.14 Measurement principle of ellipsometry [108]

จุฬาลงกรณ์มหาวิทยาลัย
CHULALONGKORN UNIVERSITY

2.9 Four-terminal specific- resistance tester

The four-point probe is a apparatus used to measure the semiconductor resistivity. By passing a current through two outer probes and measuring the voltage through the inner probes allows the measurement of the substrate resistivity. The illustrate diagram for the measurement of semiconductor sheet resistance by using the four-point probe is shown in Figure 2.15

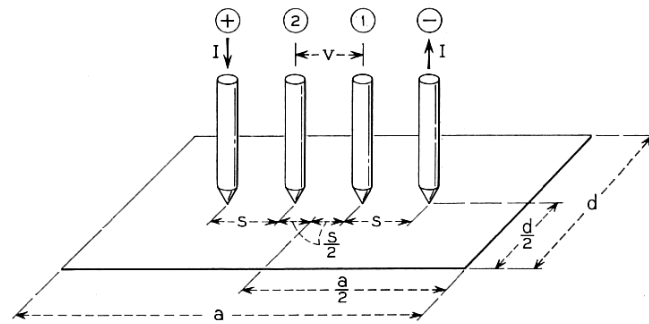

Fig. 2.15 Arrangement of a four-point probe on rectangular sample[109]

K.X. Chen et al. and Dieter K. Schroder [110] state that using the four- point probe method, the semiconductor sheet resistivity can be calculated:

$$R_s = F\frac{V}{I} \tag{2.10}$$

where V is the voltage reading from the voltmeter, I is the current by two current carrying probes, and F is a correction factor. For collinear or in-line probes with equal probe spacing, the correction factor F can be written as a product of three separate correction factors:

จุฬาลงกรณ์มหาวิทยาลัย
CHULALONGKORN UNIVERSITY

$$F = F_1F_2F_3 \tag{2.11}$$

F_1 corrects for finite sample thickness, F_2 corrects for finite lateral sample dimensions, and F_3 corrects for placement of the probes with finite distances from the the sample edges. In the case of very thin sample with the probes being far from the sample edge, F_2 and F_3 are approximately equal to one (1.0), and the expression of the semiconductor sheet resistance becomes:

$$R_s = \frac{\pi}{ln2}\frac{V}{I} \tag{2.12}$$

The four-point probe method can eliminate the effect introduced by the probe resistance, probe contact resistance and spreading resistance. Therefore, it has more accuracy than the two point probe method.

2.10 Semiconductor parameter analyzer (Keithley 4200 SCS)

Capacitance - voltage (C-V) measurement is widely used to determine semiconductor parameters, particularly in MOSCAP and MOSFET structures. The fundamental nature of these measurements makes them relevant to a wide range of applications. They are used in the research labs and semiconductor manufactures to evaluate new materials, process, device, and circuit [111].

C-V Characteristics of MOS structures and pn junctions

Doping profile, flat band voltage (V_{fb}), and threshold voltage (V_{th}) are essential parameters used for process monitoring and for new semiconductors can be derived from C-V measurements.

C-V characterizations of MOS (metal oxide semiconductor) structures.

The capacitance of the MOS structure (Fig.2.16) consist of oxide-layer capacitance (C_{ox}) and depletion layer capacitance (C_d). Total capacitance is obtained from the equation below:

$$C = \frac{C_{ox}C_d}{C_{ox} + C_d} \tag{2.13}$$

Figure 2.17 shows swept bias C-V characteristics of an n type MOS structure. Curves (a), (b), and (C) show the characteristics of the structure at low frequency, high frequency, and high frequency with pulsed bias. The carrier distribution in the MOS structure during accumulation, depletion, and inversion is shown in Figure 2.18.

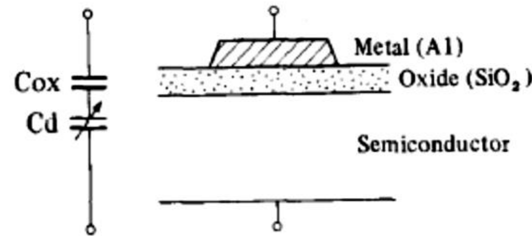

Fig. 2.16 MOS Structure [112]

(1) Accumulation region

When positive voltage is applied to the gate, majority carriers (electron) accumulate on the Si - SiO_2 surface. In this state, C_d is negligible and MOS capacitance is equal to C_{ox}.

(2) Depletion

When the applied voltage goes negative, the majority carriers are repelled from the SiO_2 surface. Donor ions remain as fixed charges, forming the depletion layer. In this state, MOS capacitance consists of C_{ox} and C_d, which varies with the applied gate voltage. The MOS capacitance is calculated from the equation (2.1).

(3) Inversion

As the applied gate voltage become more negative, the density of the minority carrier (hole) becomes greater than the density of electron at the surface of the depletion layer, forming the inversion layer. When a state of deep inversion is reached, the width of the depletion layer becomes constant. Holes in the inversion layer are supplied by the generation of electron-hole pairs caused by normal thermal agitation. This electron-hole generation is relatively slow. However, holes cannot be generated fast enough at high frequencies, so MOS capacitance decreases and becomes constants as shown in Figure 2.17 (b). But at lower frequencies, holes can be generated fast enough to replenish the inversion layer. Thus MOS capacitance becomes equal to C_{ox}, as shown

in Figure 2.17 for curve (a). When high frequency pulsed bias is applied, minority carriers are generated even more slowly than when high frequency is applied. This causes MOS capacitance to decrease even further, as shown in Figure 2.17(c)

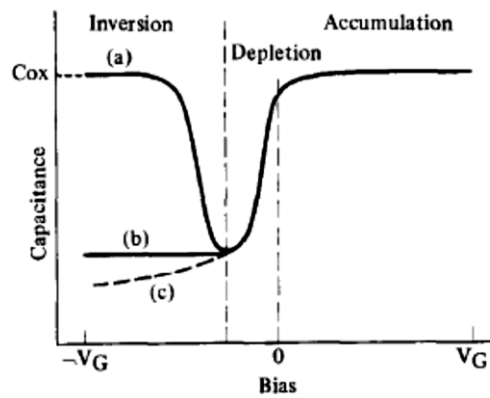

Fig. 2.17 C-V Characteristic of a MOS Structure [112]

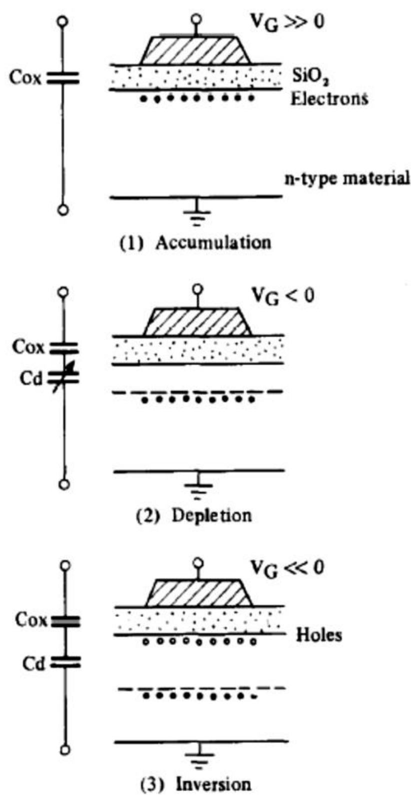

Fig. 2.18 Carrier Distribution of a MOS Structure [112]

CHAPTER 3
DC SPUTTER DEPOSITION AND MECHANICAL PROPERTIES OF (Ti,Cr)N FILM

3.1 Introduction

AISI H13 tool steel has been widely used in die casting, extrusion dies and large machining parts, due to several outstanding properties such as: high hardness, heat treatability and good maintenance of strength and hardness at elevated temperature. However, H13 steel is prone to corrosion especially after heat treatment. In case of nitriding process, this process induces formation of CrN compound resulting in depletion of Cr in the matrix and consequently lowing corrosion resistance [113-116]. Further surface modification by formation of protective layer, such as high hardness and corrosion resistance transition metal nitride film, should be employed. Due to the necessary heat treatment such as nitriding as mentioned above, temperature for any further surface modification after heat treatment must be controlled to be approximately less than 500°C. Too high surface modification temperature can induce embrittlement and can also reduce hardness and strength of H13 tools steel [117]. In order to establish protective coating layer by PVD process, low temperature less than 200ºC is preferred to maintain high matrix hardness and strength achieved by heat treatment [118]. Various methods have been reported to form transition metal nitride films such as cathodic arc deposition, thermal evaporation, ion beam assisted deposition and DC magnetron sputtering. Among these techniques, DC magnetron sputtering at low temperature offers high density ion and homogeneous films with accurate chemical composition. Binary metal nitrides such as CrN, TiN and ZrN have been reported to

improve both mechanical and corrosion resistance of steels. Each substance show outstanding unique properties, for example, TiN show high hardness value with excellent wear resistance but low corrosion resistance due to its porous structure [119]. On the other hand, other metal nitrides such as CrN and AlN exhibit good corrosion resistance with moderate wear resistance. There have been several attempts to investigate these nitride by combining two or three types of transition metals. Formation of (Ti,Al)N significantly improve both corrosion and wear resistance[35, 120]. This work show given high density of the film has potential to increase hardness and protect the matrix from corrosives penetrating through the film, this research involves mixing dense CrN into porous TiN at low temperatures to achieve dense complex (Ti,Cr)N films.

3.2 Experimental procedure

3.2.1 Sample preparation

AISI H13 steels were used as substrates in this work with a specific composition. The chemical composition of specimen (wt.,-%) is 0.43 C, 1.02 Si, 0.45 Mn, 4.71 Cr, 1.32 Mo, 0.8 V and balance Fe. The substrates were cut into disk- shape with diameter of 25 mm and thickness of 3 mm. They were polished with SiC paper down to 4000 grit followed by alumina powder (mesh size of 1 mm). The polished substrates were ultrasonic-cleaned in acetone and stored in desiccator prior to coating.

3.2.2 Deposition process

The film deposition process was conducted by using magnetron sputtering system with the background parameter of 5×10^{-5} torr. The film was deposited on both AISI H13 steel and silicon wafer. Pure Ti (99.9%) and pure Cr (99.95%) were employed as target

materials for reactive magnetron co-deposition. The substrates were heated by halogen lamp to achieve different growth temperature during coating. After the pressure and temperature reached the desired values, Ar gas was fed into the chamber with a flow rate of 40 sccm until the pressure reach to 3.2×10^{-4} torr. After the constancy of Ar, plasma was ignited, and pre-sputtering process started for duration of 5 minutes. N_2 gas as a reactive gas was then filled into the chamber with a ratio of 5% by total pressure. The nitride layer started to coat on the substrate with a deposition time of 60 minutes. The current was controlled to remain constant at 0.4 A at 370 V throughout the coating process. The relevant parameter are summarized in Table3.1

Table 3.1 PVD magnetron sputtering parameters of nitride film

Target	Ti,Cr
base pressure	5 x 10^{-5} torr
working pressure	3.2 x 10^{-4} torr
pre- sputtering	Ar gas, 5 minutes
PVD sputtering time	60 minutes
pure Ar	99.99%
pure N_2	99.99%
reactive gas	95% Ar + 5% N_2
current	0.4 A
voltage	370 V
distance	140 mm.
growth temperature	room temperature, 130°C, 190°C

3.2.3 Characterization

Both film surfaces and cross-section microstructures were investigated by scanning electron microscope (SEM). Surface morphology and roughness were observed by atomic force microscope (AFM). The chemical compositions of the coated films were determined by energy dispersive spectroscopy (EDS). Glancing incident angle X-ray diffractrometer (incident angle of 1 degree and CuKα tube) was employed to examine the crystal structure and phase formation. Mechanical properties of the coated films

were characterizing by using nanoindentation and scratch test for hardness and adhesion values.

3.3 Results and discussion

3.3.1 *Microstructure and film properties at room temperature*

Pure CrN and TiN samples as-deposition are shown in Figure 3.1 The surface color of these coated samples changed from H13 steel to silver and gold color for CrN and TiN film respectively. After co-deposition at room temperature, the color become dark metallic silver. The chemical composition was analyzed by EDS, we found that this film composed of Cr approximately 49 atomic%, Ti approximately 8 atomic %, and the rest is N. Observation of cross-section film at show in the figure 3.2 (c), the film has thickness 1 micron with a columnar structure and we expected that it has low film density. Pore size was measured by surface analysis (BET) approximate 40.71 angstrom.

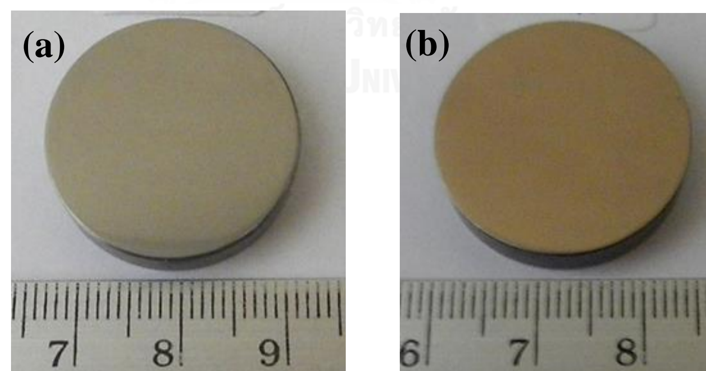

Fig. 3.1 AISI H13 samples after PVD sputtering: (a) CrN, (b) TiN.

Then, Phase of the films were determined by XRD as shown in Figure3.3. XRD peaks showed only one set of FCC crystal structure and no evident showing separation of TiN

and CrN peak can be seen. Only one set of FCC structure peaks of (111) (200) and (220) located between CrN and TiN peaks could be observed. There is no indicator of phase reparation between CrN and TiN. The XRD profiles of (Ti,Cr)N also show a small shift to TiN from CrN peaks might be due to stress appearance caused by solution in complex nitride formation and difference lattice parameters[121]. According to crystal structure, both TiN and CrN have FCC structure with lattice parameters of 4.24 Å and 4.14 Å, respectively [122, 123]. Due to similarity of FCC crystal structure and close lattice parameters, complex nitride (Ti,Cr)N which has lattice parameter close to CrN, is possible to form solid solution as agreement in previous study [85]. They indicated that the (Ti,Cr)N could formed solid solution at room temperature. The (Ti,Cr)N lattice parameters calculated from extrapolation method are found in the range of 4.18 - 4.19 Å [91]. Hardness of the coating films was measured by nanoindentation testing with Berkovich tip. The indentation depth was controlled through the advanced mode to 100 nm to eliminate the effect of substrate hardness. The speeds of loading and unloading were fixed at 30 mN/min for hardness measurement, loading was done using a diamond tip to reach a displacement depth of 100 nm. This distance includes both elastic and plastic deformation and is less than 10% of the film thickness (about 1 μm) in order to avoid the effect from the substrate. Hardness of (Ti,Cr)N film is 16.12 GPa which this value is between of CrN and TiN film hardness as a result in Figure 3.4. The elastic modulus value is about the same.

CHULALONGKORN UNIVERSITY

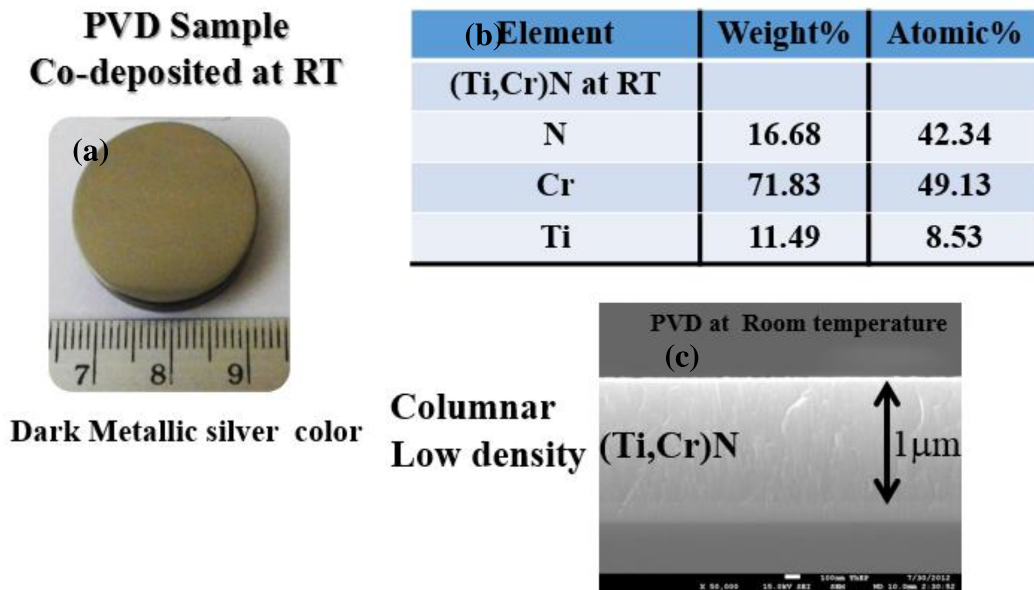

(b) Element	Weight%	Atomic%
(Ti,Cr)N at RT		
N	16.68	42.34
Cr	71.83	49.13
Ti	11.49	8.53

Fig. 3.2 Co-deposition sample growth at room temperature (a) film color (b) composition by EDS, (c) cross-sectional film.

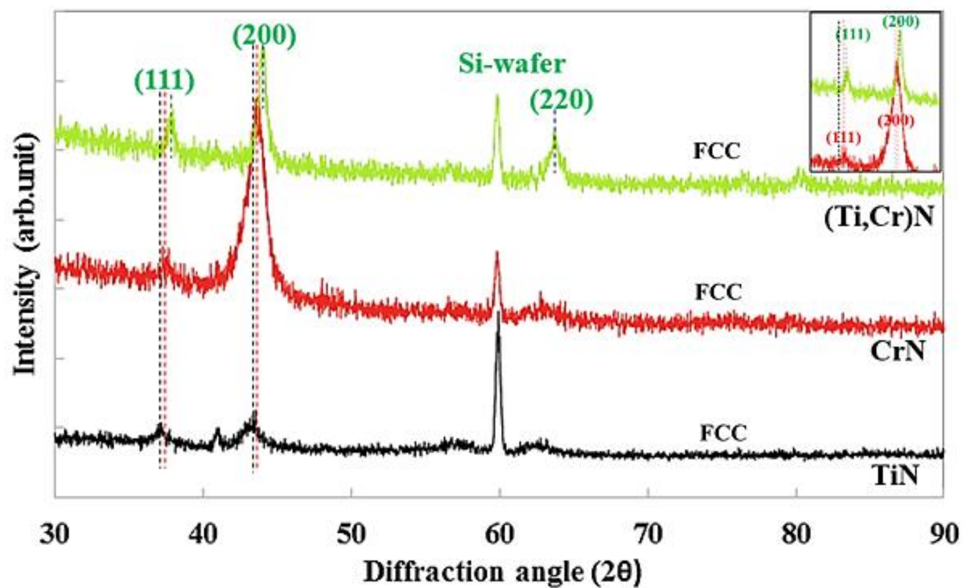

Fig. 3.3 XRD pattern of PVD sample of CrN, TiN, and (Ti,Cr)N

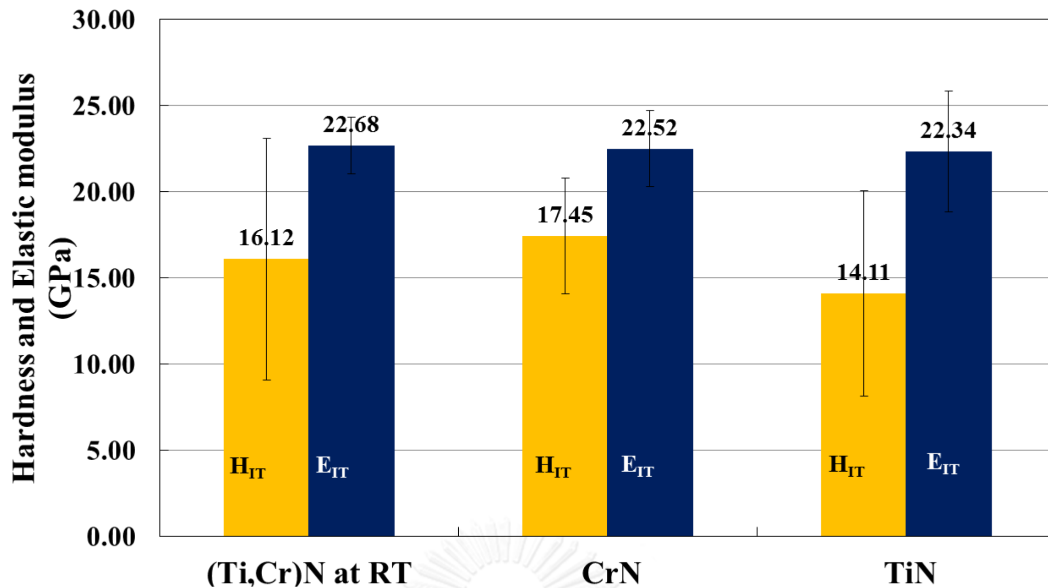

Fig. 3.4 Hardness of CrN, TiN, and (Ti,Cr)N films tested by Nano-indentation.

The roughness value (RMS or R_q) of CrN, TiN, and (Ti,Cr)N films were showed in Figure 3.5. As comparing, CrN film (1.36 nm) has lower surface roughness than TiN film (1.65 nm). After co-deposition of TiN and CrN, results showed remarkable increasing of surface roughness to 2.35 nm. Film adhesion was characterized by the scratch tester with spherical diamond tip stylus (120 degree angle and 200 mm radius) in progressive mode with increasing force from 1-20 N. With increasing loading force along the scratch distance “progressive mode”, a small crack starts to form in the (Ti,Cr)N layer. This force that induced crack formation is defined crack formation is defined as L_{c1} with continuously increasing loading, severe cracks occurred resulting in full delamination of the (Ti,Cr)N layer. The force which causes full delamination is defined as L_{c2} [124]. Scratch results are also showed decreasing of endurance scratch when compare to individual films cause may be lower of surface contact area at interface between substrate and film as a results showed in Figure 3.6. Both of roughness and adhesion results indicated that co-deposition of both film do not always

get the good property. In order to improve both of properties, controling growth parameters must be concerned.

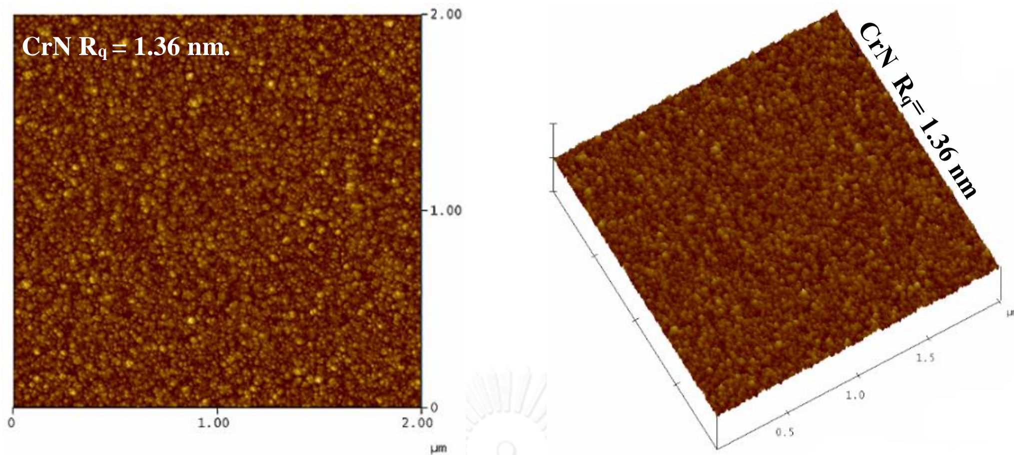

(a) CrN film roughness

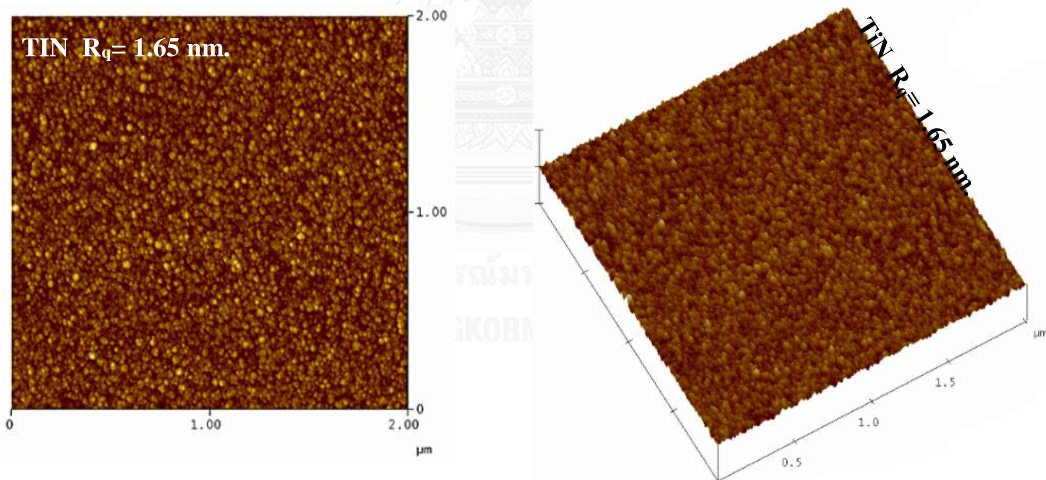

(b) TiN film roughness

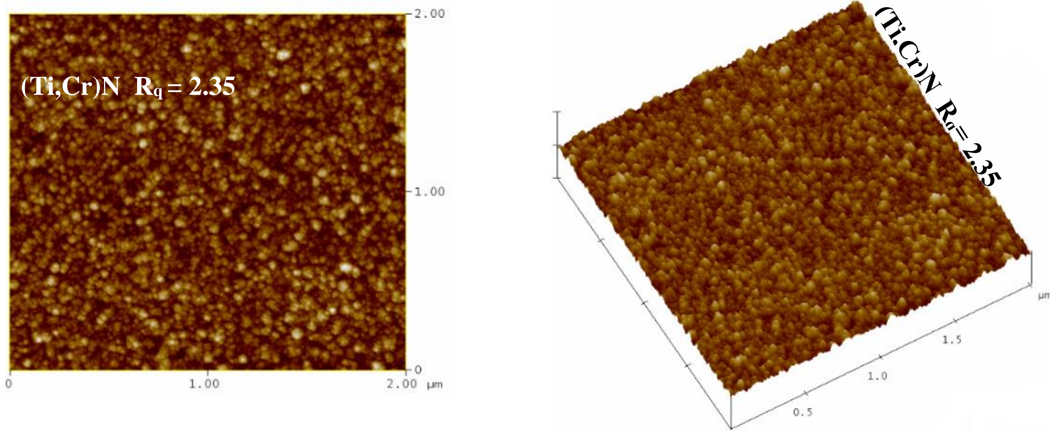

(c) (Ti,Cr)N film roughness

Fig. 3.5 AFM image of film growth at room temperature: (a) CrN film roughness, (b) TIN, and (c) (Ti,Cr)N film roughness.

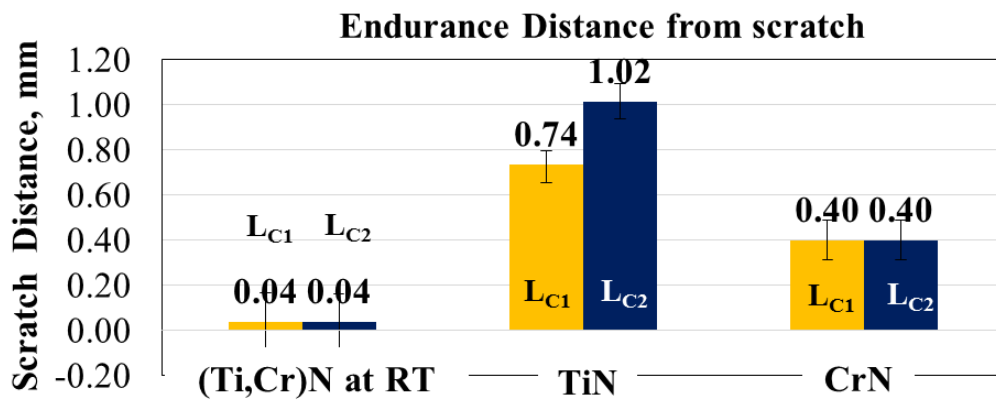

Fig. 3.6 Distance and critical load of scratch testing (L_{c1}, L_{c2}) which film growth at room temperature

Adhesion is obtained when the following these mechanisms occur. There are molecular adsorption, diffusion or penetration across the interface and form interfacial bonds, and forming chemical bond with the interface molecules. The addition property

can be improved by increasing temperature during grown film. The increasing temperature leads to surface faster mobility resulting in higher nucleation density, and then, interfacial bonds is possibly produced. Therefore, we will investigate effect of temperature on film properties on next section.

3.3.2 Microstructure and film properties after growth film with increase substrate temperature

After increasing substrate temperature, the film color does not change. The chemical composition analyzed by EDS of film growth at 190 °C had nearly value as film growth at room temperature. It can be seen that all coating layers were composed of Cr, Ti and N. The ratio of Cr:Ti:N were roughly similar for all samples regardless the coating temperature.

PVD sample
Co-deposition at 190 °C

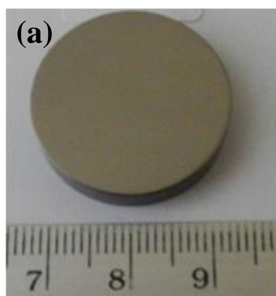

Dark metallic silver color
(film color is not change)

(b) Element	Weight%	Atomic%
(Ti,Cr)N at 190 °C		
N	17.89	44.42
Cr	70.32	47.02
Ti	11.79	8.56

Equiaxed
High density

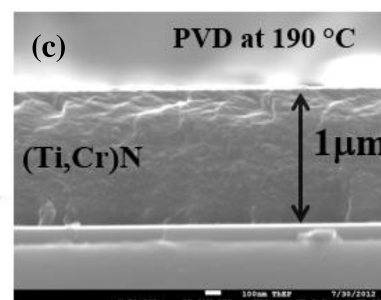

Fig. 3.7 Co-deposition sample growth at 190°C (a) Film color (b) Composition by EDS, (c) Cross-sectional film.

Amount of Cr was in the range of 47- 49 at.-% and amount of Ti was approximately 8 at.-% while the rest were N. Hence, the coating layer, which can be in the form of $(Ti_{0.15}Cr_{0.85})$ N, which is rich in chromium. Observation of cross-section film as shown in the figure 3.7, the film has thickness 1 micron with an equiaxed structure and we expected that it has high film density with small pore size. The equiaxed film should has pore size of equiaxed sample measured by surface analysis is approximate 30.47 angstrom which is smaller than columnar structure film.

Then, all samples were checked crystal structure which coated film at different growth temperature as shown in Figure. 3.8. These results showed only one set of FCC structure similar to XRD profile of sample coated at room temperature indicating that growth temperature did not affect on crystal structure.

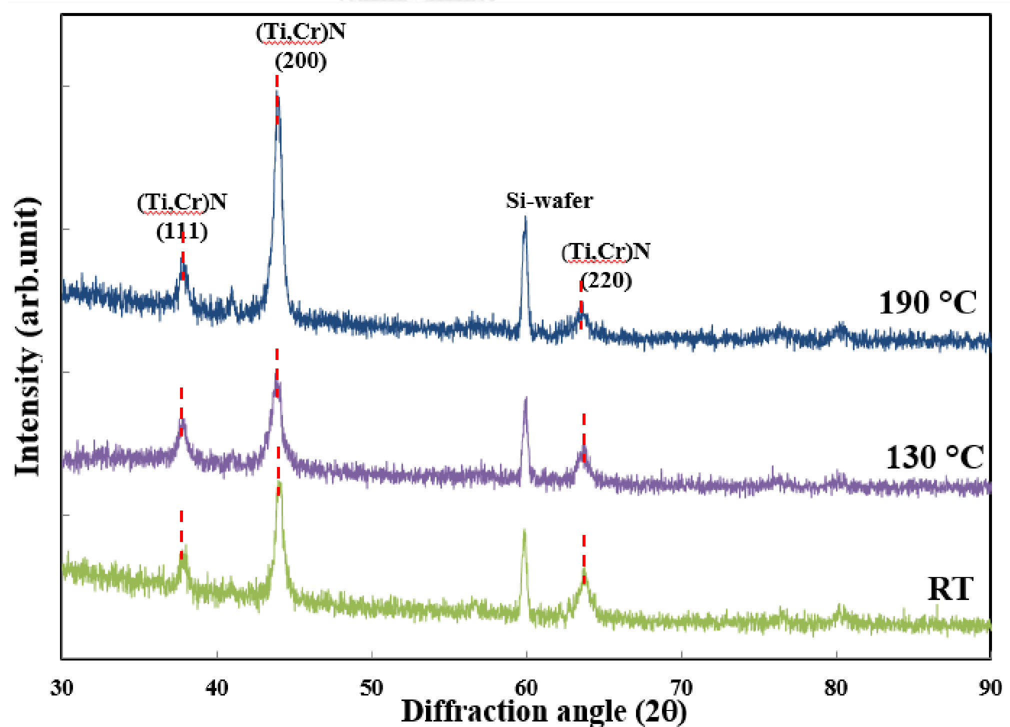

Fig. 3.8 XRD profiles of coated samples at different growth temperature.

The surface morphology of samples coated at different growth temperatures, were examined by AFM. The film coated at the growth temperature 190 ºC has lower surface roughness than those samples coated at lower temperature (130 ºC and room temperature). Roughness value (RMS or R_q) decreases from 2.35 (room temperature) to 2.17 nm, and 1.93 nm for coating temperature of 130 ºC to 190 ºC, respectively. As comparing the films growths at room temperature, 130 ºC and 190 ºC, it has to be noted that the roughness of the film varies as the growth temperature changes.

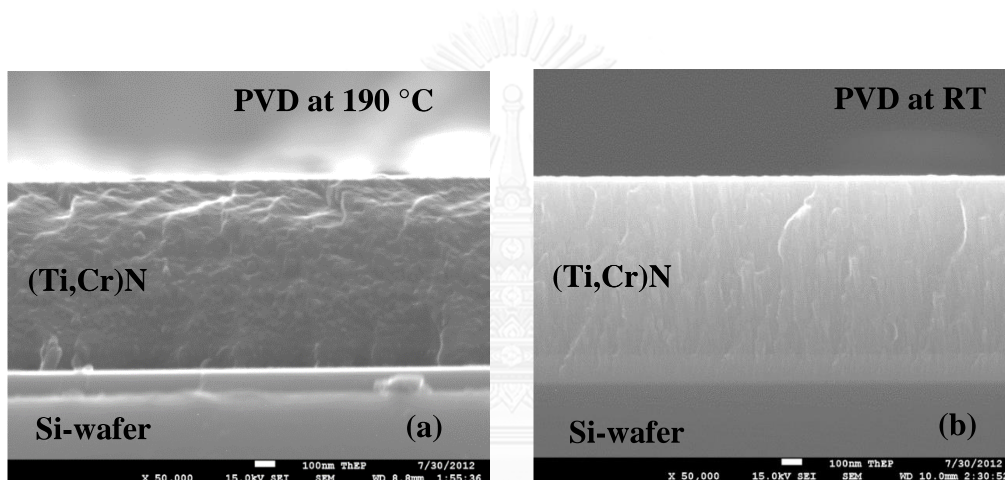

Fig. 3.9 SEM image of cross-section PVD films (a) 190 °C, (b) room temperature

CHULALONGKORN UNIVERSITY

Figure 3.9 shows the cross-sectional microstructure of the film comparing film growth at room temperature and 190 °C. The thickness of the coating layer of both sample was approximately 1 μm and was not significantly affected by difference growth temperatures. However, the temperature has a great influence on the structure of the coating layer; dense and smooth equiaxed grains are obtained by coating at 190 ºC while coating at room temperature produces large columnar structure. Combining with equiaxed structure in Fig.3.9 (a), it can be indicated that the structure of the coating layer at 190 ºC is in SMZII of Thornton model. On the other hand, the coating layer at

low temperature shows a rough and low density film with columnar structure (Fig.3.9 (b)), hence, it can be indicated as SZM I [125, 126]. The increasing growth temperature induces higher kinetic energy of adatoms on the surface resulting in higher nucleation density on the surface which leads to agglomeration of nuclei and growth of film in layer mode (FvdM mode)[127], therefore, dense smooth surface with equiaxed structure coating layer can be achieved.

According to loading-unloading curve of nanoindentation measurement in Figure 3.10 the measured P_{max} and h_f were recorded as shown in Table 3.2. The growth temperature strongly affected the hardness of the coating layer in spite of similarity in composition. The P_{max} at 4.4 mN (190 ºC) was highest at comparing to 3.6 mN and 3.2 mN for 130 ºC and room temperature respectively.

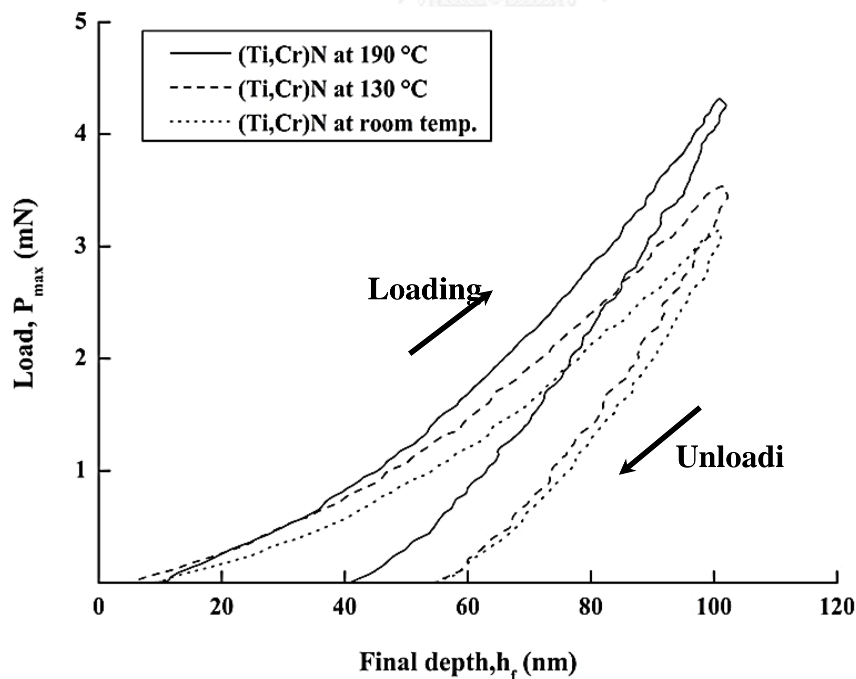

Fig. 3.10 Representative load of final depth of (Ti, Cr)N at difference growth temperatures

Table 3.2 Final depth, h_f, measured at same displacement

Condition	**Peak load P_{max} (mN)**	**Final depth h_f (nm)**
(Ti,Cr)N at room temp.	**3.2**	**52.3**
(Ti,Cr)N at 130 °C	**3.6**	**52.3**
(Ti,Cr)N at 190 °C	**4.4**	**40**

The final depth, which is the permanent depth after the indenter is fully unloaded [128], due to plastic deformation (h_f) followed the opposite trend. These results suggested that the coating layer at high temperature impeded the film to be deformed and had better penetration resistance. The hardness values and modulus of elasticity are displayed in figure 3.11. The hardness of the (Ti,Cr)N significantly increased from 16.12 GPa to 24.79 GPa while the modulus of elasticity small increased values when increasing the growth temperature from room temperature to 190 ℃.

จุฬาลงกรณ์มหาวิทยาลัย
Chulalongkorn University

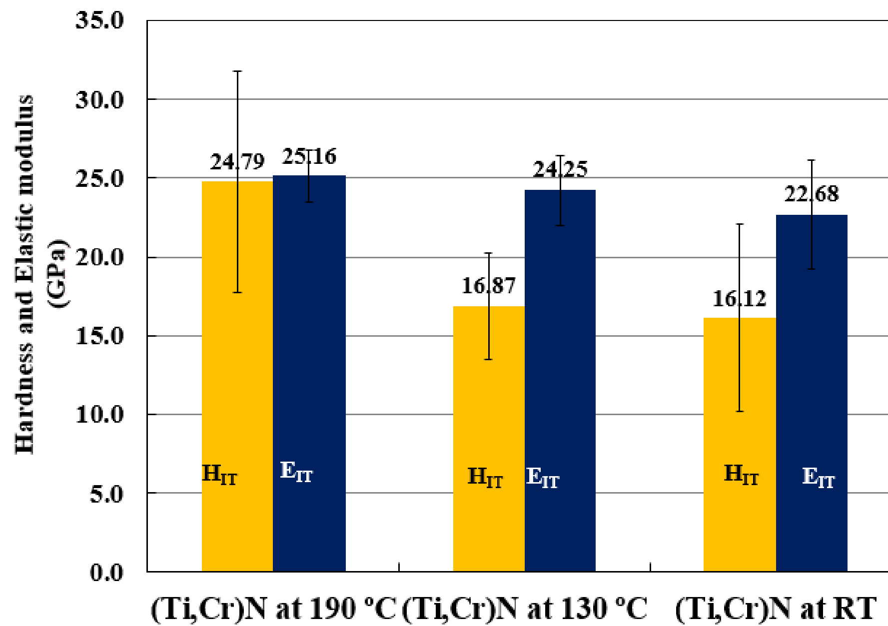

Fig. 3.11 Hardness of (Ti,Cr)N films growth at RT, 130°C, and 190 °C tested by Nano-indentation.

Compares scratch tracks of films coated at different growth temperatures. The (Ti,Cr)N layer coated at room temperature fully delaminated in less than 100 μm of scratch distance showing very low value of L_{c2} and very poor adhesion characteristic. Due to the very short distance prior to L_{c2}, the L_{c1} could not detected by an optical microscope. In contrast, the (Ti,Cr)N layer coated at 190 ºC showed better given the L_{c1} occurred after several hundreds of micron in scratch distance. The distance causing L_{c2} was too long to be seen in this Figure, as illustrated in Fig 3.12. The results of all filmss were collected in figure 3.13. It can be concluded that the adhesion properties was significantly improved by increasing growth temperature. The mobility and diffusion rate of adatoms were enhanced at higher temperatures. With higher diffusion rate, interface between substrate and film tends to change from abrupt interface to interdiffusion at interface to the substrate which normally exhibits excellent adhesion. Next section, we will discuss on the the corrosion resistance by using Tafel

extrapolation and electrochemical impedance spectroscopy (EIS) technique

(a) (Ti,Cr)N at room temperature

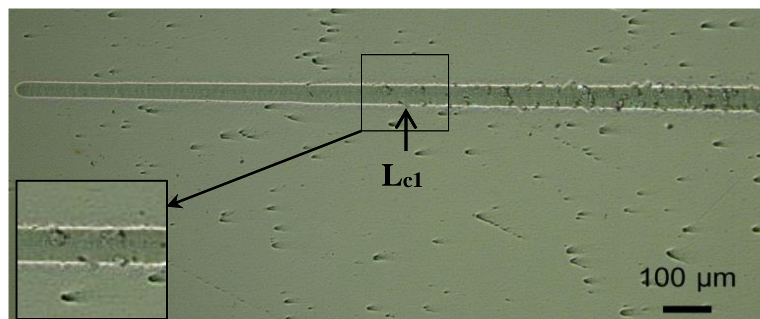

(b) (Ti,Cr)N at 190 °C

Fig. 3.12 Scratch track (a) (Ti,Cr)N at RT, (b) (Ti,Cr)N at 190 °C

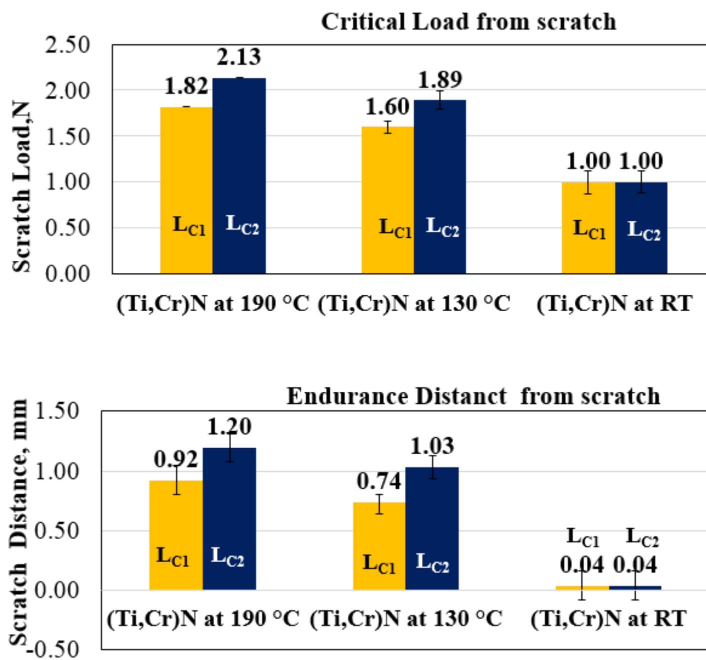

Fig. 3.13 Distance and critical load of scratch testing (L_{c1}, L_{c2}) which film growth at RT, (Ti,Cr)N at 130 °C, and (Ti,Cr)N at 190 °C

3.4 Summary of mechanical properties

(Ti,Cr)N film can be fabricated by co-deposition reactive magnetron sputtering. Mechanical properties of (Ti,Cr)N film lie between TiN and CrN film. However, adhesion of (Ti,Cr)N film is not as good as TiN or CrN. Adhesion and surface roughness of (Ti,Cr)N film can be improved by increasing substrate temperature. Critical load (Lc_2) and scratch distance (Lc_2) increase from 1 N with distance of 0.04 mm to 2.13 N with distance of 1.2 mm after increasing substrate temperature to 190 °C. Hardness of (Ti,Cr)N film remarkably increases from 16.12 GPa to 16.87 GPa and 24.79 GPa after increasing substrate temperature from room temperature to 130 °C and 190 °C respectively. The improvement of film properties is due to changing of film structure from low density columnar to high density equiax grain. This could be accommodated by higher nucleation density due to fast surface diffusion according to higher substrate temperature.

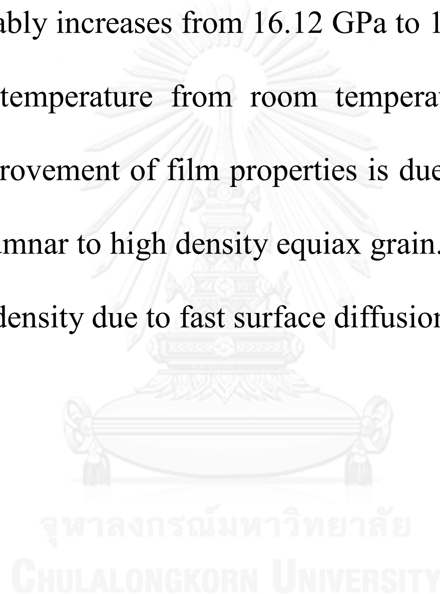
จุฬาลงกรณ์มหาวิทยาลัย
Chulalongkorn University

CHAPTER 4
DC SPUTTER DEPOSITION AND CORROSION PROPERTIES OF (Ti,Cr)N FILM

4.1 Introduction

Physical vapor deposition (PVD) has been widely used for surface modification of steel tools and machine parts [129-131]. A nitride fim prepared by PVD can significantly increase lifetime and service quality of steel parts due to enhanced wear and corrosion resistance [132, 133] . However, the corrosion behavior of nitride-coated steels is strongly dependent on the structure and defects in the films which could be influenced by coating condition. The film surface and grain boundary act as high diffusion paths for corrosion reagents to rapidly diffuse through the film and react with the steel substrate underneath.

The number and size of pores within the film have a great influence on corrosion resistance due to penetration possibilities. Transition metal nitride compounds, such as CrN, TiN and ZrN films have been reported to improve both corrosion and wear resistance of steels [119, 121, 134]. There have been many attempts to combine the merits of each nitride by utilizing two or more to form complex nitrides such as (Ti,Cr)N and (Ti,Zr)N [135-137]. The (Ti,Cr)N system has demonstrated improved mechanical properties; therefore, it would be interesting to investigate whether it might also improve corrosion resistance.

The corrosion behavior of PVD coated steels in an aqueous solution has received great attention recently [138, 139]. To obtain qualitative details of corrosion behavior, both Potentiodynamic Polarization and Electrochemical Impedance

Spectroscopy (EIS) techniques have to be employed together. The EIS, a well-known technique to investigate corrosion behavior of nitride film [22, 100, 102, 140], can also provide details on electrochemical mechanism and reaction kinetics. Interpretation of the EIS model is a key to extract information on electrochemical corrosion characteristics. In this work, the corrosion behavior of (Ti,Cr)N films on AISI H13 steel deposited by DC magnetron sputtering at difference growth temperatures was investigated. Growth temperature was demonstrated to influence the degree of corrosion protection as well as microstructural characteristics of the coating layer.

4.2 Experimental procedure

4.2.1 Sample preparation

H13 tool steel with chemical composition shown in Table 4.1 was used as the substrates. All samples were cut in to disk shape with diameter of 25 mm and 3 mm thickness. After that, they were polished with SiC paper down to 4000 grit following by alumina powder with mesh size of 1 μm. After polishing, all samples were rinsed in acetone using ultrasonic cleaner and stored in a desiccator before coating.

(Ti,Cr)N coating process was done by the DC magnetron sputtering. The (Ti,Cr)N film was deposited on both AISI H13 steel and silicon wafer. Targets used in this study are pure Ti (99.9%) and pure Cr (99.95%) with diameter of 7.62 cm for reactive magnetron co-deposition. The substrates were heated by halogen lamp to reach the desired growth temperatures which are kept constant during coating process. The substrate temperature was controlled by monitoring temperature of dummy sample placed next to the substrate. Before coating process, evacuation to minimize oxygen and moisture in the coating chamber was done until base pressure reach 5×10^{-5} torr.

During evacuation, the steel substrates and silicon wafer were heated simultaneously to the coating temperature. After pressure and temperature reach to the required values, Argon gas as a sputtering gas was added into the coating chamber with flow rate of 40 sccm until the pressure reach 3.2×10^{-4} torr. Argon plasma was ignited and pre-sputtering process was started to clean surface for 5 minutes. Then, nitrogen gas as a reactive gas was filled into the coating chamber with pressure ratio of 5% and the (Ti,Cr)N coating process was started. The holding time for coating process was fixed at 60 minutes. During coating process, the current was kept constant at 0.4 A with 370 V. The coating temperatures were room temperature (RT), 130 °C and 190 ºC. The coating parameters were already shown in chapter 3 [135].

Table 4.1 Chemical composition of AISI H13 steel

Element	C	Si	Mn	Cr	Mo	V	Fe
Wt.%	0.43	1.02	0.45	4.71	1.32	0.8	Bal.

4.2.2 Electrochemical corrosion tests

Electrochemical corrosion was investigated by potentiodynamic polarization and Electrochemical Impedance Spectroscopy (EIS). Corrosion testing was performed in 3.5%NaCl solution at room temperature (25 ± 1ºC) using the Potentiostat/Galvanostat (PGSTAT 302N). It was conducted in a three electrode cell using Ag/AgCl as reference electrode (RE), a Pt plate as counter electrode (CE) and sample as the working electrode (WE). The sample with surface area of 2.45 cm^2 was immersed in the solution for corrosion testing. The electrochemical measurements were carried out by at least 3 samples for each condition of sample preparation.

Before the polarization measurement, the coated samples were immersed in the solution for 30 minutes for stabilizing corrosion potential (E_{corr}) or open circuit potential

(E_{ocp}). The polarization curves of samples were performed in the potential range from the initial potential of 0.5 V vs. (Ag/AgCl) to the final potential of 1.5 V vs. (Ag/AgCl) with a scan rate of 1 mV/s. The corrosion potentials (E_{corr}), corrosion currents (I_{corr}), Tafel slopes (b_a, b_c) of all samples were evaluated from the polarization curves by the Tafel extrapolation method [25]. The ranges of standard deviations for potentiodynamic polarization is $2\text{-}8 \times 10^{-4}$. The polarization resistances (R_p) were calculated from I_{corr}, b_a, b_c through the equation; $R_p = b_a b_c / 2.3 I_{corr} (b_a + b_c)$ [141].

For EIS measurement, the samples were kept at their corrosion potentials. A small amplitude ac signal (10 mV) is applied to the cell. The frequencies (ω) were in the range of 0.05 Hz to 100,000 Hz. Response impedances were measured and shown in Nyquist plot and Bode plot. The equivalent circuit models were fitted and interpreted by the NOVA 1.7 software. The ranges of standard deviations for EIS is $2\text{-}5 \times 10^{-2}$.

4.2.3 Coating characterization

Surface morphology of film before and after corrosion test was observed by scanning electron microscope (SEM). In order to investigate the corrosion information of film obtained from electrochemical tests in relation with the film structure, the film surface area, film density in form of porosity number and average pore size were measured by the surface area analysis (BET).

4.3 Results and discussion

4.3.1 Film microstructure

In previous section, we discussed on the mechanical properties. We found that increasing of substrate temperature has a great effect on the film microstructure and

lead to improve mechanical properties, which are hardness and adhesion. Therefore, this section we will discuss on corrosion resistance. Figure 4.1 showed the different of film microstructure which is the interesting point to investigate the corrosion resistance. The possibility are dense film might be can retard solution penetrate to substrate (fig.4.1 a). Conversely, columnar film easily permit solution penetrate to substrate results in corrosive under the film (fig. 4.1 b). In order to study corrosion behavior during film corroded in electrolyte. This property can be studied by electrochemical impedance spectroscopy technique (EIS).

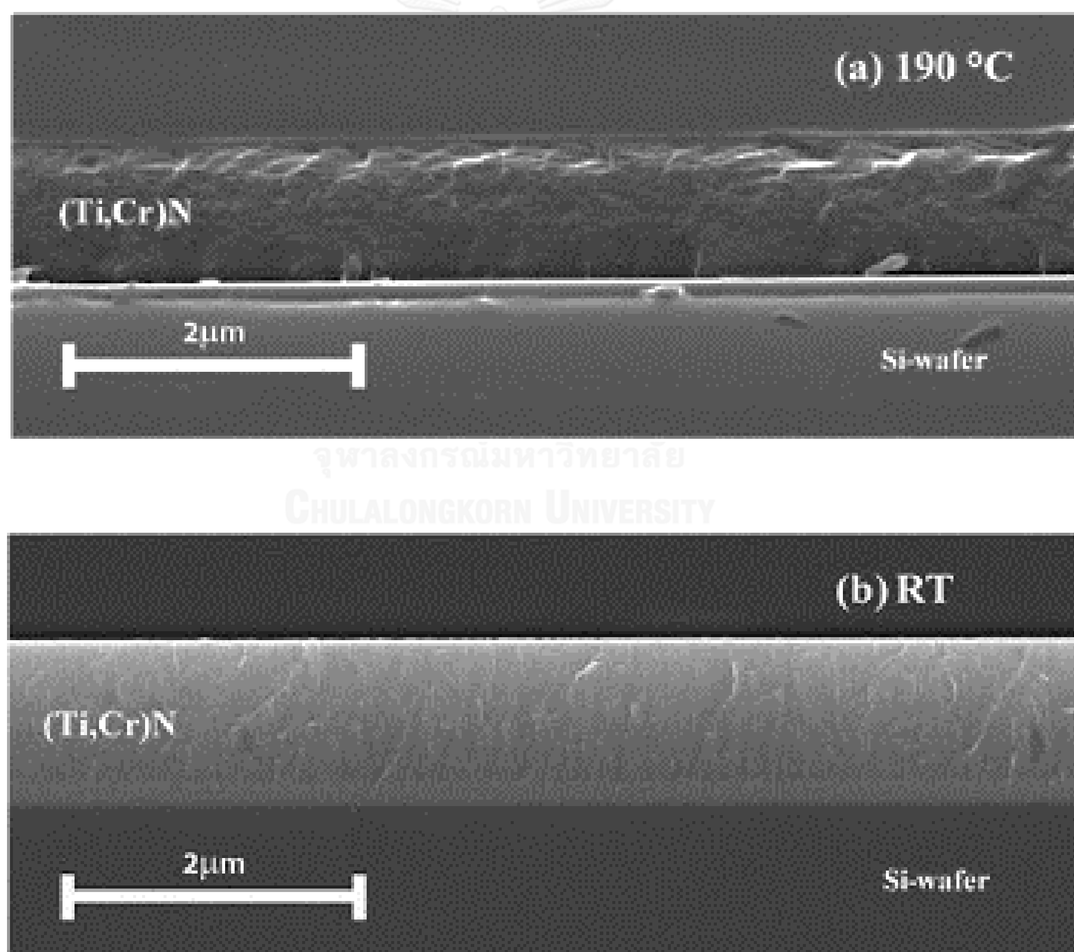

จุฬาลงกรณ์มหาวิทยาลัย
CHULALONGKORN UNIVERSITY

Fig. 4.1 SEM image of cross-sectional (Ti,Cr)N films (a) at 190 °C, (b) at RT

4.3.2 Polarization measurement

The analysis of anodic polarization curves is based on corrosion testing technique which could estimate corrosion resistance of materials. Therefore, this technique is used to preliminarily estimate corrosion resistance of film prior to EIS technique corrosion testing. Anodic polarization curve of each film conditions are shown in Figure4.2. In general, it appeared that the 190°C-grown film demonstrated the best corrosion potential. However, the clearer discussion can be pursued by considering Tafel calculation which the results of E_{corr}, I_{corr}, and R_p can be obtained (Table 4.2). Both R_p and E_{corr} of the 190ºC-grown film are the higher value more than other conditions. Moreover, the lowest I_{corr}, indicating the highest corrosion resistance was achieved in this sample. On the other hand, the sample coated at RT exhibited the lowest values of E_{corr} and R_p with the highest I_{corr} which implies the opposite trend in corrosion resistance. Therefore, the growth temperature was a key parameter affecting corrosion behavior. In order to shed light on the electrochemical corrosion behavior, the EIS results will be discussed next.

จุฬาลงกรณ์มหาวิทยาลัย
CHULALONGKORN UNIVERSITY

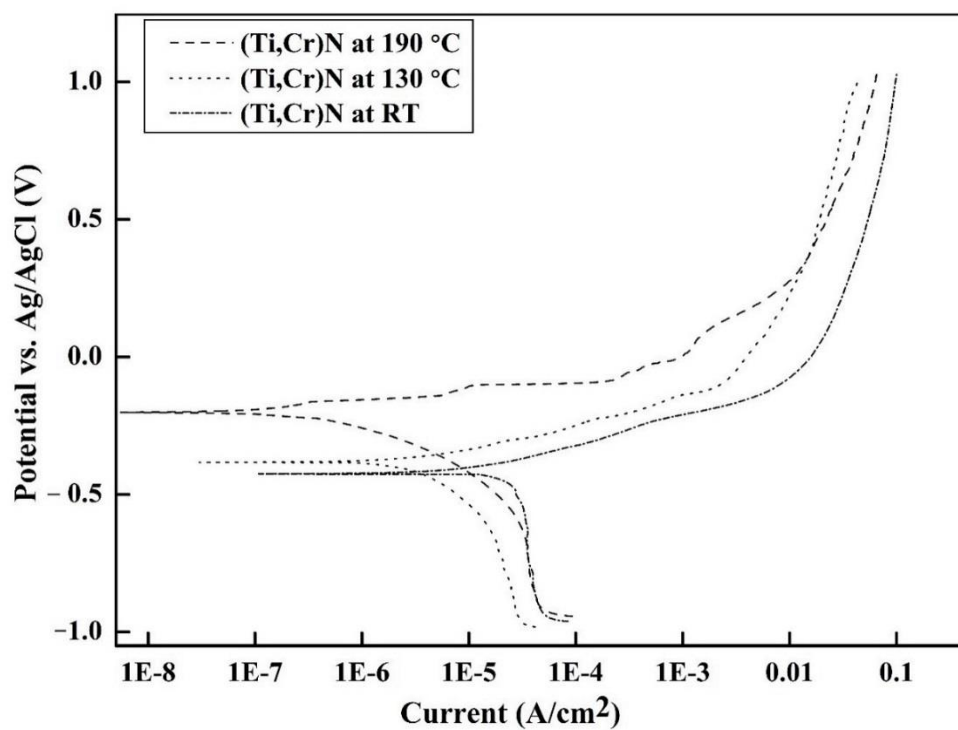

Fig. 4.2 Anodic polarization curves of (Ti, Cr)N film at different growth temperature.

Table 4.2 Tafel calculation data of (Ti,Cr)N film prepared at different growth temperature

PVD Coating	i_{corr} ($\mu A/cm^2$)	E_{corr} (mV)	b_c (mV)	b_a (mV)	R_p (kΩ)
190˚C-grown film	0.02	-320	123	402	10.13
130˚C-grown film	0.05	-453	176	458	4.47
RT-grown film	0.15	-460	151	609	1.65

จุฬาลงกรณ์มหาวิทยาลัย
Chulalongkorn University

4.3.2 Electrochemical impedance measurements (EIS)

The more information of corrosion kinetic could be obtained from EIS. Figure 4.3 shows the Nyquist plot of (Ti,Cr)N films grown at different temperatures. The appearance of semi-circle is related to degree of corrosion resistance. The features of high real part (Z_{Re}) and high imaginary part (Z_{Im}) implies high resistance to corrosives. The 190ºC-grown film exhibited the largest semi-circle among the three temperatures, indicating the highest corrosion resistance. The results yielded a similar trend of corrosion resistance to those earlier observed by potentiodynamic polarization. In addition, the 190ºC- and 130ºC- grown film show a single semi-circle (one time constant) [142]. However, it can be seen that the two semi-circles (two time constants) are found for the (Ti,Cr)N film at growth temperature of RT as shown in Figure 4.4. Bode plots of the (Ti,Cr)N film at difference growth temperature are shown in Figure4.5. The (Ti,Cr)N film at growth temperatures of 190ºC and 130ºC have similar features of Bode plots which show single semi-circle. The RT-grown film clearly shows two semi-circles and the lowest of phase angle. The homogeneous of surface can be interpreted from the phase angles of Bode plot. The higher phase angle indicates the more homogeneous surface[143]. The higher phase angle means the denser film resulting in the higher corrosion resistance[144]. From the results, the 190ºC-grown film shows the highest phase angle which is nearly 70ºC. Therefore, the degree of surface homogeneity and density increases with growth temperature.

Appearance of a single semi-circle suggests that corrosion occurs at the interface between the solution and the film surface. It is possible that short of exposure time in corrosion medium results in not sufficient to reveal the degradation of substrate[145]. On the other hand, two semi-circles reveal two difference interfacial

reactions at both the solution/film and the solution /substrate interfaces[146, 147]. Therefore, the RT-grown film in this study might contain defects, allowing penetration of corrosion electrolyte toward the substrate. The Bode plot results also suggested that the 190ºC-grown film yielded highest corrosion resistance which could be previously confirmed by both Nyquits plot and potentiodynamic polarization.

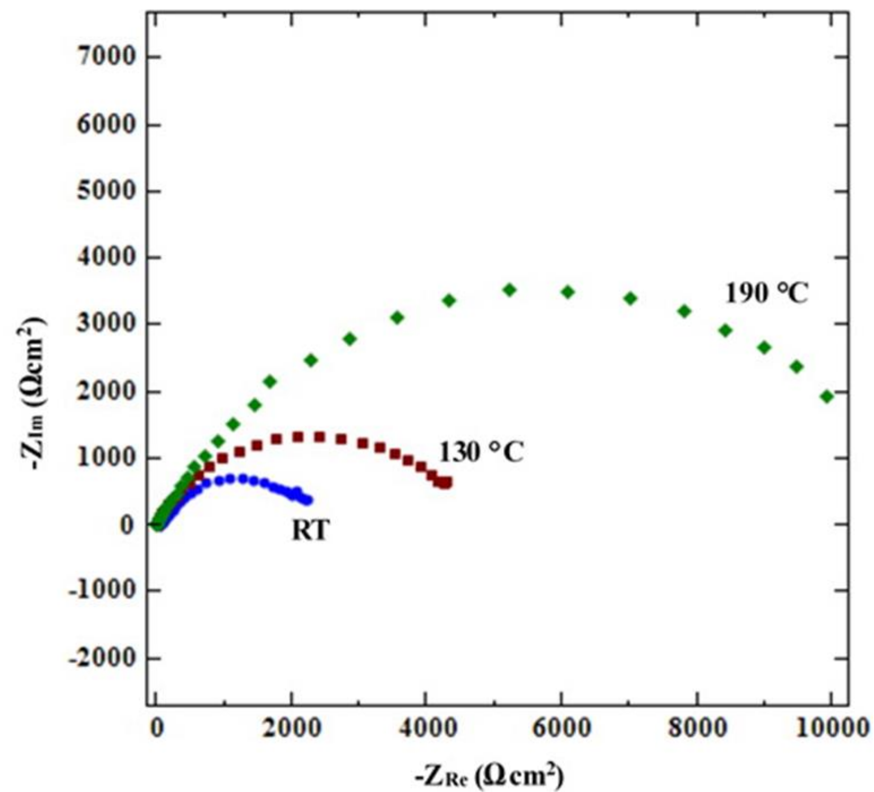

Fig. 4.3 Nyquist plot of the (Ti,Cr)N film at difference growth temperature.

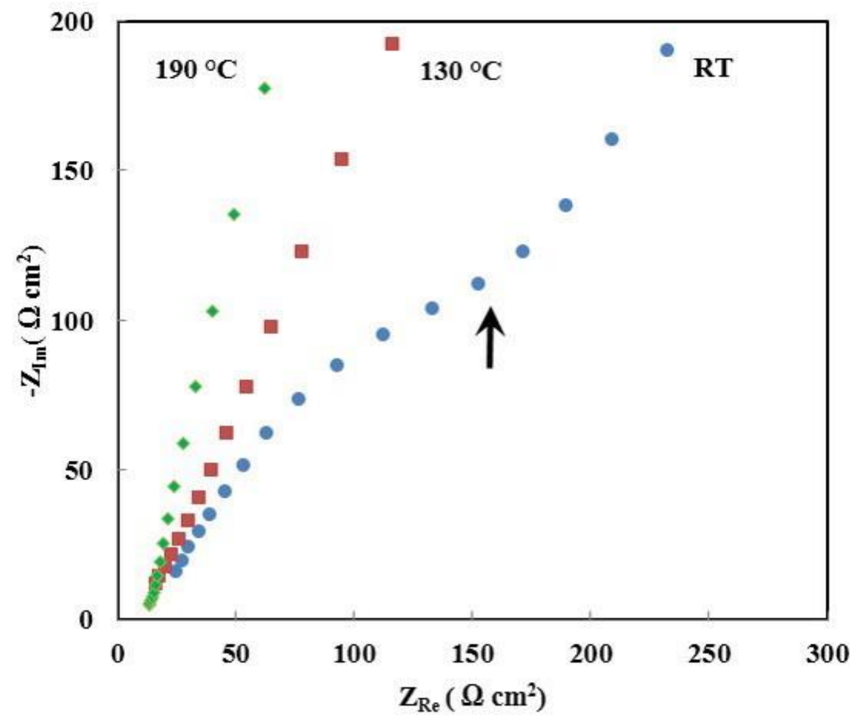

Fig. 4.4 Nyquist plot shows two semi-circles of the (Ti,Cr)N film at RT.

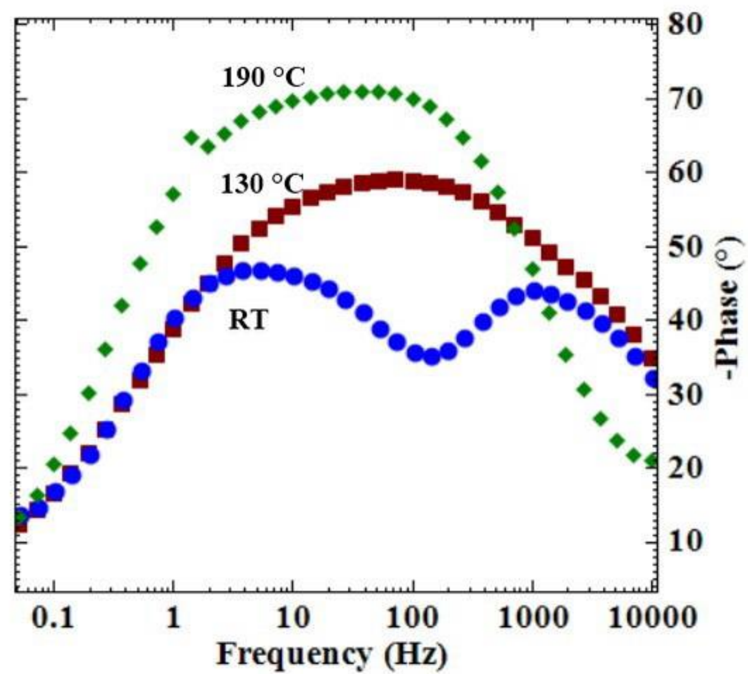

Fig. 4.5 Bode plots of (Ti,Cr)N film at different growth temperature.

The corrosion behavior of the 190 ºC-grown film in 3.5%NaCl solution for longer immersion time was also investigated. The transformation features of Bode plots at different immersion times (1 - 8 hours) are shown in Figure 4.6. Changes from single to two semi-circles with increase immersion time were observed, indicting the plausible penetration of electrolytes through defects such as pinholes toward the steel substrate. Determination of an equipment circuit types is key to gain better understanding on the electrochemistry at the interface of the system [148-151]. The equivalent circuit models for the three growth temperatures are shown in Figure 4.7. The RT-grown film yielded a two-circuit model type, comprising the first and second circuits due to corrosion in the film and substrate. The main component are solution resistance (R_e), the charge transfer resistance of (Ti,Cr)N film (R_p), capacitance (C) and/or constant phase element (CPE or Q), diffusion impedance [O], and the substrate resistance (R_s).The EIS circuit models in Figure 4.7 are [R_e(R_pQ)], [R_e([R_pO] Q)], and [R_e([R_pO]Q)(R_sQ)] for growth temperature of 190 °C, 130 °C and RT, respectively. Replacement of pure capacitance (C) by CPE was often employ for better fitting [152].

CHULALONGKORN UNIVERSITY

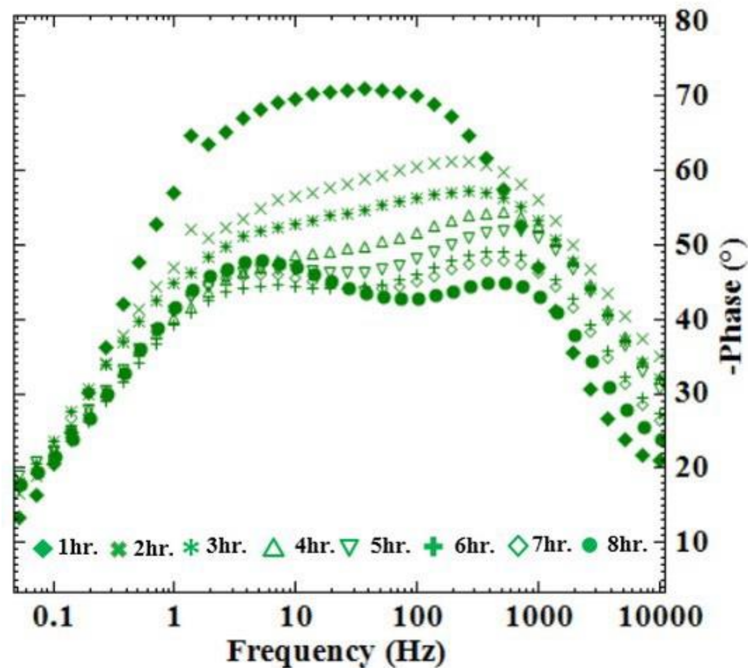

Fig. 4.6 Bode plots of the (Ti,Cr)N film at 190ºC - grown temperature at various immersion times.

The CPE is generally defined as[153]:

$$Z_{CPE} = \frac{1}{Y_0(j\omega)^n} \quad (4.1)$$

where Z is impedance of CPE, j is imaginary number ($j^2 = -1$) , Y_o is constant of CPE (Mho), ω is angular frequency (rad/s), n is a constant phase angle of CPE (rad). The values of n between 0.93 and 1 imply a pure capacitor, whereas those less than 0.93 indicate an impure one. From Figure 4.7, the cotangent - hyperbolic diffusion impedance (O) values describe the finite length diffusion inside the pores [154-156]. The impedance of O element [157] is

$$Z_0 = \frac{tanh\,(B\sqrt{(j\omega)}}{Y_o(\sqrt{(j\omega)})} \quad (4.2)$$

where, ω is the angular frequency (rad/s) , Y_o is the magnitude of O (Mho), and B is the time constant (sec ^{½}) ,which B $= \delta/\sqrt{D}$ where δ is the length of a layer (film thickness) and D is diffusion coefficient (m^2/s) [156, 158].

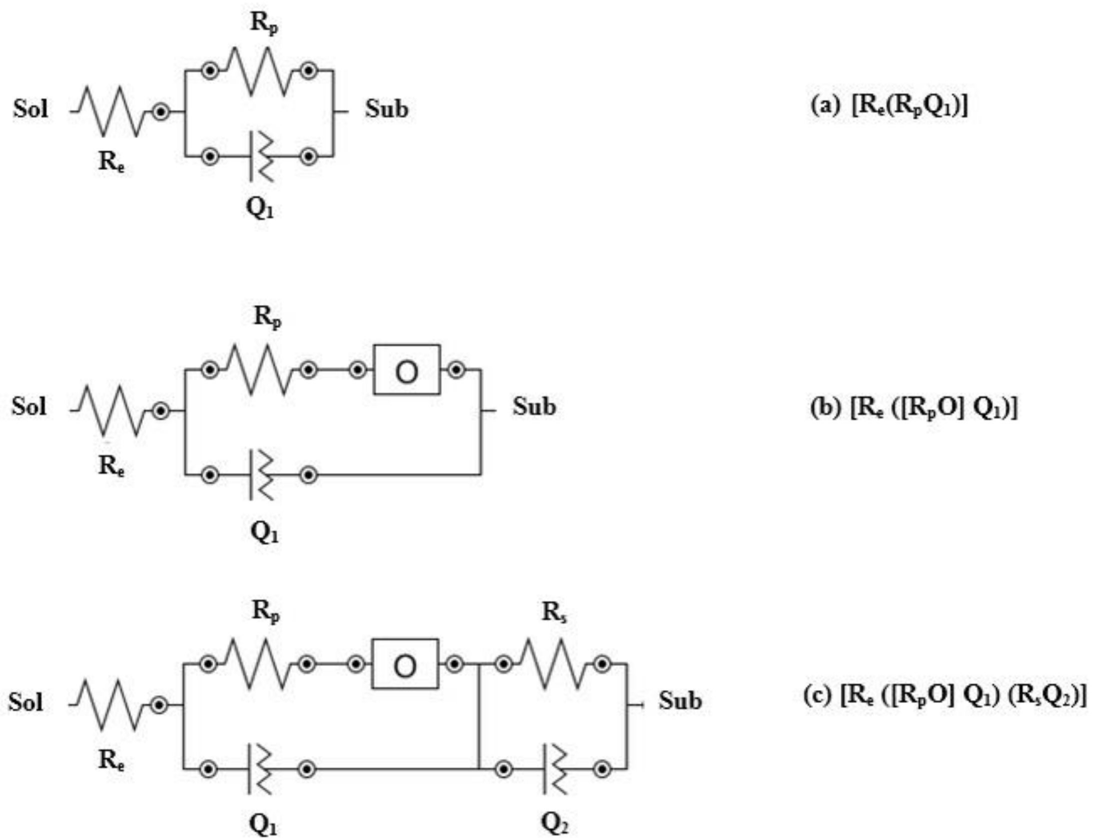

Fig. 4.7 EIS equivalent circuit model of the (Ti,Cr)N film at (a) 190ºC-grown film , (b) 130ºC- grown film (c) RT- grown film in 3.5% NaCl solution. Sol and Sub means solution and steel substrate, respectively.

Fitting results of the proposed circuit models are displayed in Table 4.3. The 190°C-grown film possessed highest film resistance (R_p: 16.95×10^3 Ω cm^2) which is

up to four orders of magnitude higher than other films. Hence, corrosion resistance could be seen to be proportional to the growth temperature. The 190°C-grown film also yielded the lowest constant of CPE (Y_o). However, the highest constant phase angle of CPE (n) was obtained in this film, implying the highest capacitance. No cotangent-hyperbolic characteristic was observed. This was also reflected by the B values as summarized in Table 4.3. The diffusion coefficient (D) were calculated to be 0.44 and 0.0009 m^2/s for RT-and 130°C-grown films, respectively. From these data, the degree of mass diffusion was higher for the RT-grown films, compared to that from 130 °C.

Table 4.3 EIS data obtained by equivalent circuit simulation of the (Ti,Cr)N film at different growth temperatures.

Grown temperature	R_e (Ωcm^2)	Q_1 or CPE_1		R_p ($\times 10^3$) (Ωcm^2)	Q_2 or CPE_2		R_s (Ωcm^2)	O	
		$Y_o(10^{-6})$ (Mho)	n		$Y_o(10^{-6})$ (Mho)	n		$Y_o(10^{-6})$ (Mho)	B ($sec^{1/2}$)
RT	11.52	240	0.68	4.80	96.5	0.67	147	0.0145	5×10^{-6}
130°C	11.64	103	0.69	9.63	-	-	-	1930	1.218
190°C	12.49	89	0.82	16.95	-	-	-	-	-

จุฬาลงกรณ์มหาวิทยาลัย
CHULALONGKORN UNIVERSITY

Movement of corrosive electrolytes toward the substrate could be facilitated by certain characteristic of porosity [159, 160]. BET revealed strong dependence of the growth temperature on the pore size as summarized in Table 4.4. The RT-grown film possessed a larger pore size (40.72 Å) compared to 30.47 Å of the 190°C-grown film. This parity in size was likely associated with the different degrees of penetration of corrosive electrolytes toward the substrate, which was in agreement with the previously reported EIS model in this study.

Table 4.4 BET surface analysis of (Ti,Cr)N at 190 °C-grown film and RT-grown film.

Grown temperature	Surface area (m^2/g)	Total pore volume (cm^3/g)	Average pore diameter (Å)
RT	1.57	0.0016	40.72
190°C	2.01	0.0015	30.47

4.3.3 SEM observation after corrosion

Differences in corrosion resistance among the three films can be reflected by the surface morphology show in Figure 4.8. It is obvious that a larger degree of localized corrosion (area and grain boundary) was observed in the RT- grown film. On the other hand, the 190°C-grown film exhibited only a small area of corrosion. These morphological nature further confirmed the earlier reported results on both the EIS circuit models and the effect of pore size on the penetration capability.

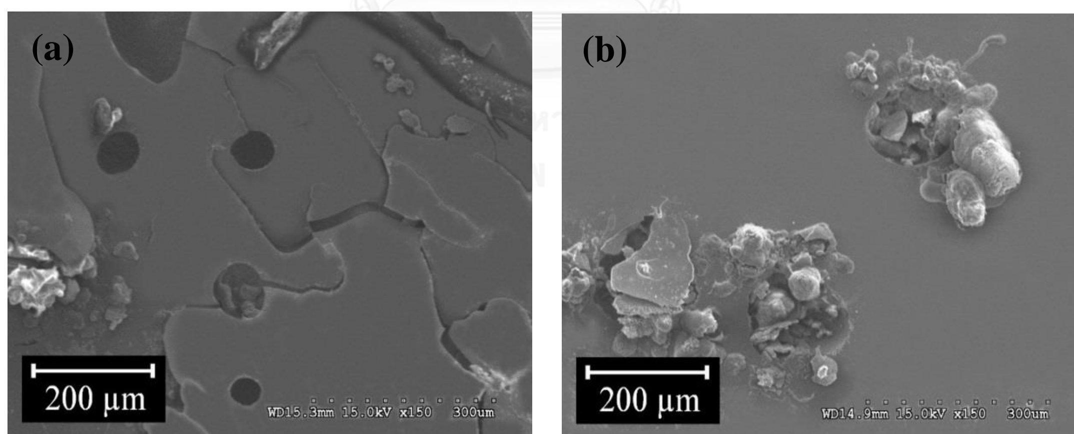

Fig. 4.8 SEM images of (a) RT-grown film, (b) 190 °C-grown film after polarization test

4.4 Summary of corrosion resistance

(Ti,Cr)N film grown at 190 °C exhibit better corrosion resistance comparing to film grown at 130 °C and room temperature. E_{corr} can be increased from -460 mV to -320 mV while I_{corr} decreases from 0.15 μA/cm^2 to 0.02 μA/cm^2 when increasing grown temperature from room temperature to 190 °C. The better corrosion resistance is due to changing of film microstructure and increasing film density which can be explained by EIS evaluation. According to EIS result, film grown at 190 °C shows only corrosion at solution/film interface while film grown at room temperature exhibit corrosion at solution/film interface and corrosion at H13 substrate. This indicates that solution can penetrate through (Ti,Cr)N film grown at room temperature. Therefore, (Ti,Cr)N grown at 190 °C can be considered as the better protective film than that grown at room temperature.

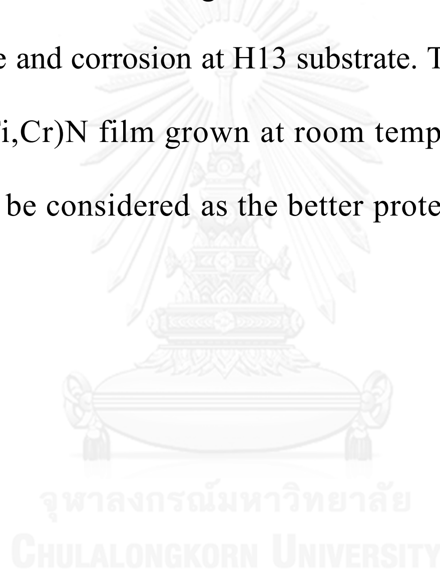

CHAPTER 5
DC SPUTTER DEPOSITION OF RUTHENIUM (Ru) DOPED INDIUM OXIDE (In_2O_3) AS TRANSPARENT CONDUCTING OXIDE FILM

5.1 Introduction

Transparent conductive oxides are commonly applied as anode material in organic electroluminescent (OEL) devices. Perfect properties were required in anode material. The required properties are low electrical resistivity, high transmittance in visible range, excellent surface contact, and the high work function (∅). Currently, indium - tin oxide ($In_{0.9}Sn_{0.1}O_y$, ITO) is the most attractive anode material, however, ITO has a low ∅ of 4.7 eV [69]. The ∅ of anode material is required over 5 eV because the highest occupied molecular orbital of the hole transport layer is usually over 5 eV. In addition, anode with high ∅ can reduce the potential barrier, allowing efficient hole carrier injection, which decrease the operating voltage of the device. For these reasons, several approaches have been proposed to improve ∅ of ITO and / or develop new anode material.

Doping with high work function elements such as Mo, Ni, W, and Pt into In_2O_3 film enhances the high ∅, Popular method, which In_2O_3 was doped by the precious metal has been reported [70, 71, 74]. Although this method effectively increases of ∅, low with electrical resistivity and high transmittance, Surface contact still is not as good as expected. Revision performance of operating voltage and luminescence of OEL devices, the surface contact of the interface between transparent conductive oxides and organic layer is attractive issue to consider. To increase surface contact, it can be done

by decreasing surface roughness degree of anode material. Chen et al. [75] reported that they succeeded increasing surface smoothness by addition of In_2O_3 into TiO_2 thin films In_2O_3 could suppress grain growth of TiO_2 crystals. Identical method (same way), possible to mixed elements, precious metal, into In_2O_3 in order to obtain the same result. Therefore, doping precious or element having of high work function into In_2O_3 for synthesis anode layer in organic electroluminescence material is aim of our objective.

Ruthenium oxide is an interesting material because of the effective work function ($\emptyset_{m,eff}$) over 5 eV [81]. Furthermore, detailed studies on the characteristic, both electrical and physical of Ru doped In_2O_3 ($In_{1-x}Ru_xO_y$) films have not been reported elsewhere. To consider the $\emptyset$ of $In_{1-x}Ru_xO_y$ film in this study, we employed the $\emptyset_{m,eff}$ estimation technique instead of the conventional UPS, XPS, and Kelvin probe technique, because $\emptyset$ obtained from these ways is easily changed by the presence of absorbed species on the surface of materials. The $\emptyset_{m,eff}$ value of the electrode materials was estimated from the capacitance-voltage (C-V) characteristics of electrode/insulator/Si capacitors [81, 161, 162]. The $\emptyset_{m,eff}$ of the $In_{1-x}Ru_xO_y$ films is only determined at the $In_{1-x}Ru_xO_y$ electrode/insulator interface rather than the top surface and bulk of the electrode. Therefore, the $\emptyset_{m,eff}$ estimation technique features to discuss real $\emptyset$ of anodes in OEL devices. In this paper, the influence of Ru content on the electrical and physical properties of the $In_{1-x}Ru_xO_y$ films is studied. In addition, we discuss usefulness of ITO/$In_{1-x}Ru_xO_y$ stack structure as transparent conductive oxides.

CHULALONGKORN UNIVERSITY

5.2 Experimental procedure

5.2.1 $In_{1-x}Ru_xO_y$ thin film preparation

P-type Si with a 100-nm-thick SiO_2 layer and synthetic quartz were used as substrates to evaluate the specific resistivity, transmittance and surface roughness of the samples. The $In_{1-x}Ru_xO_y$ thin films were deposited on substrates at room temperature under an Ar/O_2 (30/10 sccm) atmosphere at a pressure of 0.5 Pa by DC magnetron co-sputtering using In_2O_3 (99.99%) and pure Ru (99.90%) targets with sputtering parameters in table 5.1. The sputtering targets were 3 inches in diameter. The substrates were rotated at a rate of 18.5 rpm during sputtering. The composition of the $In_{1-x}Ru_xO_y$ thin films was varied by changing the sputtering power of each target as listed in Table 5.2. In addition, the pure In_2O_3 and RuO_2 samples after PVD sputtering as shown in Figure 5.1 respectively. The $In_{1-x}Ru_xO_y$ thin films were annealed at 100 – 200 °C in 3% hydrogen to examine their resistivity. A 150 nm-thick ITO film was also deposited on an $In_{0.38}Ru_{0.62}O_y$ thin film (3 nm) to fabricate an ITO/ultrathin $In_{0.38}Ru_{0.62}O_y$ bilayer by RF sputtering using an $In_{0.9}Sn_{0.1}O_y$ target. RF sputtering was performed at a sputtering power of 200 W under an Ar/O_2 (19.2/0.8 sccm) atmosphere at a pressure of 0.5 Pa.

Table 5.1 PVD magnetron sputtering parameters of oxide films.

Target	*In_2O_3 , Ru*
Base pressure	~ 6.5 x 10^{-4} torr
Working pressure	~ 3.75×10^{-3} torr
Pre- sputtering	Ar gas, 3 minutes
PVD sputtering time	Depend on composition
Pure Ar	99.99%
Pure N_2	99.99%
Reactive gas	30% Ar + 10% O_2
Current	Depend on composition
Voltage	Depend on composition
Distance	-
Sputtering power	Table

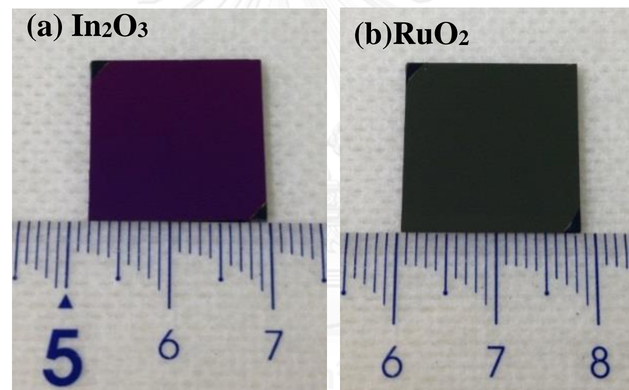

Fig. 5.1 P-type Si with a 100-nm-thick SiO_2 layer samples after PVD sputtering: (a) In_2O_3, (b) RuO_2.

CHULALONGKORN UNIVERSITY

Table 5.2 Co-sputtering conditions and $In_{1-x}Ru_xO_y$ composition.

Sputter power (W)		$In_{1-x}Ru_xO_y$ composition	
In_2O_3	Ru	Deposition rate	ICP-AES
200	0	In_2O_3	-
200	20	$In_{0.95}Ru_{0.05}O_y$	-
100	20	$In_{0.89}Ru_{0.11}O_y$	-
100	50	$In_{0.76}Ru_{0.24}O_y$	$In_{0.74}Ru_{0.26}O_y$
50	20	$In_{0.70}Ru_{0.30}O_y$	-
50	50	$In_{0.49}Ru_{0.51}O_y$	-
20	20	$In_{0.44}Ru_{0.56}O_y$	-
100	100	$In_{0.38}Ru_{0.62}O_y$	$In_{0.38}Ru_{0.62}O_y$
20	50	$In_{0.27}Ru_{0.73}O_y$	-
20	100	$In_{0.17}Ru_{0.83}O_y$	-
20	100	$In_{0.07}Ru_{0.93}O_y$	-
0	100	RuO_2	-

5.2.2 Fabrication of $In_{1-x}Ru_xO_y/SiO_2$ MOS capacitors

$In_{1-x}Ru_xO_y$-gate metal-oxide-semiconductor (MOS) capacitors were fabricated on p-Si substrates as shown in Figure 5.2. The pattern number 80 was used to measure CV curve in this experiment. Thermal SiO_2 layers of varying thicknesses (5.7, 7.1, 9.2, 10.9 and 12.4 nm) were formed using a conventional furnace at 950 °C in an O_2 atmosphere. Then, 150 nm-thick $In_{1-x}Ru_xO_y$ films were deposited on the SiO_2 layers and patterned using a lift-off process. ITO (150 nm)/$In_{0.38}Ru_{0.62}O_y$ (3 nm) gate MOS capacitors were also prepared.

Chulalongkorn University

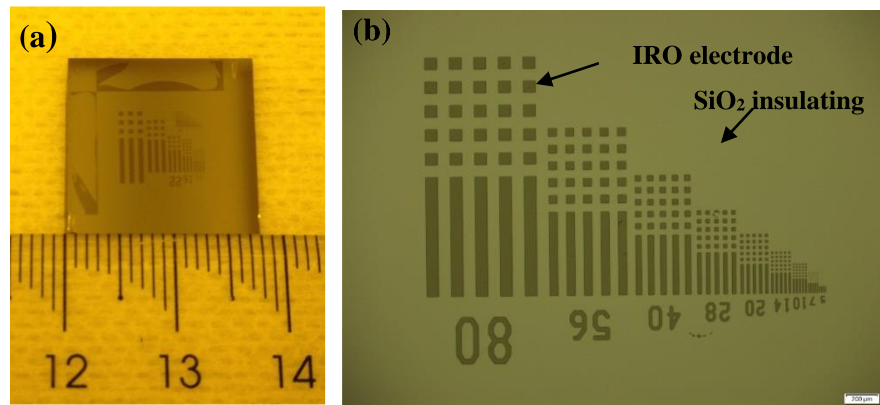

Fig. 5.2 Fabrication of: (a) MOS capacitor (b) Pattern no. 80 of MOS capacitor.

5.2.3 Characterization of the $In_{1-x}Ru_xO_y$ thin films

The chemical composition of the $In_{1-x}Ru_xO_y$ thin films was determined by inductively coupled plasma atomic emission spectroscopy (ICP-AES). An X-ray diffractometer (XRD Bruker D8 discover: Kanagawa, Japan) using CuKα radiation was employed to examine the crystal structure and phase formation of the films. Surface morphology and roughness were observed by atomic force microscopy (AFM, SI-DF40P2). The transmittance of the oxide films was measured using a spectroscopic ellipsometer (M-2000^{TM} XLS-100 D2: Tokyo, Japan) with a quartz tungsten halogen light source. The specific resistivity of the oxide films was studied by a four-terminal specific- resistance tester (four-point probe resistivity processor, Σ-5+). The electrical properties of the MOS capacitors were determined using C-V measurements performed with a semiconductor parameter analyzer (Keithley 4200 SCS). Flat-band voltage (V_{fb}) and equivalent oxide thickness (EOT) were estimated from C-V characteristics using MIRAI-ACCEPT software [163] to determine $\emptyset_{m,eff}$.

5.3 Results and discussion

5.3.1 Composition and phase of $In_{1-x}Ru_xO_y$ thin films

The chemical composition of the $In_{1-x}Ru_xO_y$ thin films was estimated from deposition rate and ICP-AES data summarized in Table 5.1. Several compositions of $In_{1-x}Ru_xO_y$ thin films were observed. The compositions of $In_{0.38}Ru_{0.62}O_y$ and $In_{0.74}Ru_{0.26}O_y$ estimated from ICP-AES data showed good agreement with the compositions of $In_{0.38}Ru_{0.62}O_y$ and $In_{0.76}Ru_{0.24}O_y$, respectively, determined from deposition rate. The surface roughness, transmittance, and electrical properties of In_2O_3, $In_{0.95}Ru_{0.05}O_y$, $In_{0.38}Ru_{0.62}O_y$, and RuO_2 films were then studied.

Figure 5.3 shows XRD profiles of the $In_{1-x}Ru_xO_y$ thin films on SiO_2/Si substrates. The structure of the pure In_2O_3 and RuO_2 films can be attributed to the body-centered cubic (BCC) crystal structure of In_2O_3 and tetragonal crystal structure of RuO_2, respectively [164-166]. The XRD peaks of the $In_{0.95}Ru_{0.05}O_y$ film are consistent with the (211), (222), and (332) planes of the BCC structure of In_2O_3. The XRD patterns revealed that increasing the content of Ru changed the phase structure of the films from BCC to amorphous. As Ru content was increased in the In_2O_3 films, the peaks from the BCC phase gradually decreased in intensity and eventually became broad. When the Ru content was increased to a composition of $In_{0.76}Ru_{0.24}O_y$, the peaks from the BCC phase of In_2O_3 started to disappear. Formation of amorphous phase may be caused by co-deposition of In_2O_3 and Ru. The presence of Ru atoms inhibited the growth of crystalline In_2O_3 by acting as an adatom that limited the diffusion time for atoms in In_2O_3 to arrange themselves to form a crystalline structure.

The surface morphology of the $In_{1-x}Ru_xO_y$ thin films was examined by AFM, as shown in Figure 5.4. The crystalline In_2O_3, $In_{0.95}Ru_{0.05}O_y$, and RuO_2 films exhibited

large RMS roughness of 4.83, 2.88, and 1.66 nm, respectively. In contrast, the surface roughness of the $In_{0.38}Ru_{0.62}O_y$ film was much lower (0.69 nm) because of its amorphous structure. The smooth surface of the $In_{0.38}Ru_{0.62}O_y$ film should increase the contact area with any overlayer to result in improved electroluminescence and current injection [167-169]. Therefore, surface roughness is an important factor influencing the performance of anode material.

5.3.2 Optical characteristics of $In_{1-x}Ru_xO_y$ thin films

Figure 5.5 a shows the optical transmittance of 150 nm-thick In_2O_3, $In_{0.95}Ru_{0.05}O_y$, $In_{0.38}Ru_{0.62}O_y$ and RuO_2 films on synthetic quartz substrates measured over the wavelength range of 250 – 1000 nm. The In_2O_3 film showed a maximum transmittance of approximately 92% at a wavelength of 600 nm because of its large bandgap (3.75 eV) [170, 171]. The maximum transmittance of the $In_{0.95}Ru_{0.05}O_y$ film was slightly lower than that of the In_2O_3 film; about 80% at 600 nm. The $In_{0.38}Ru_{0.62}O_y$ and RuO_2 films showed much lower transmittance of 8% and 0%, respectively. Considering their potential use as an anode material in OEL devices, the $In_{0.38}Ru_{0.62}O_y$ film has the advantage of possessing a smooth surface, although higher transmittance would be desirable.

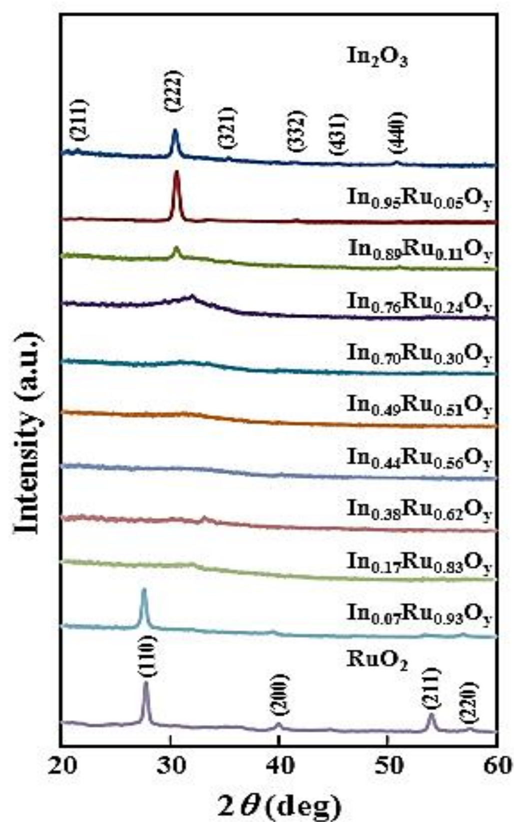

Fig. 5.3 XRD patterns of $In_{1-x}Ru_xO_y$ thin films on SiO_2/Si substrates. Ru content was varied from 0 to 1.0.

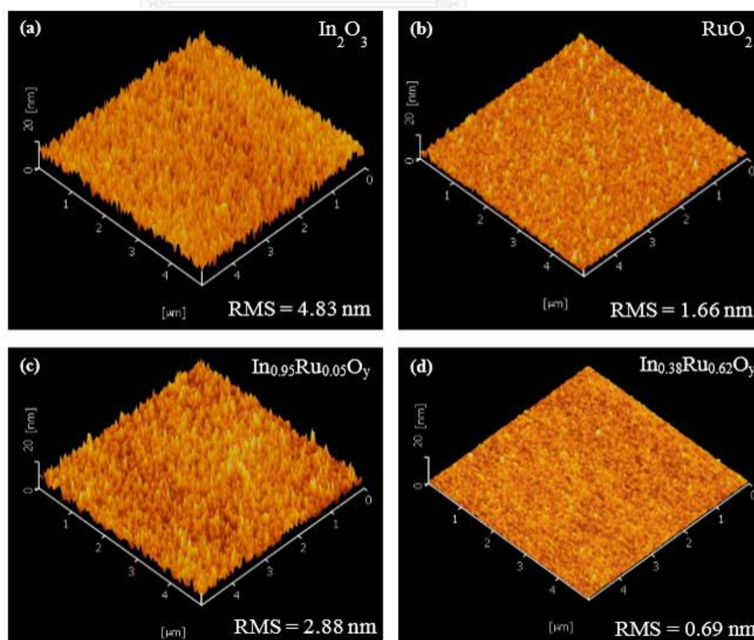

Fig. 5.4 AFM images of as-grown films of (a) In_2O_3, (b) RuO_2, (c) $In_{0.95}Ru_{0.05}O_y$, and (d) $In_{0.38}Ru_{0.62}O_y$

Next, we examined the thickness dependence of transmittance of the $In_{0.38}Ru_{0.62}O_y$ film, as shown in Figure 5.5b. The thickness of $In_{0.38}Ru_{0.62}O_y$ films was varied from 1 to 10 nm. The transmittance increased as the film thickness decreased. For thicknesses less than 3 nm, the maximum transmittance was more than 80%. The transmittance of 150 nm-thick ITO and ITO (150 nm)/$In_{0.38}Ru_{0.62}O_y$ (3 nm) films are also plotted in Fig. 3b. The ITO/$In_{0.38}Ru_{0.62}O_y$ film exhibited a high transmittance of 80%, nearly as good as that of the ITO film at 600 nm. These results indicate that the transmittance of an amorphous $In_{0.38}Ru_{0.62}O_y$ film can be improved by using an ITO (150 nm)/ultrathin $In_{0.38}Ru_{0.62}O_y$ (3 nm) bilayer.

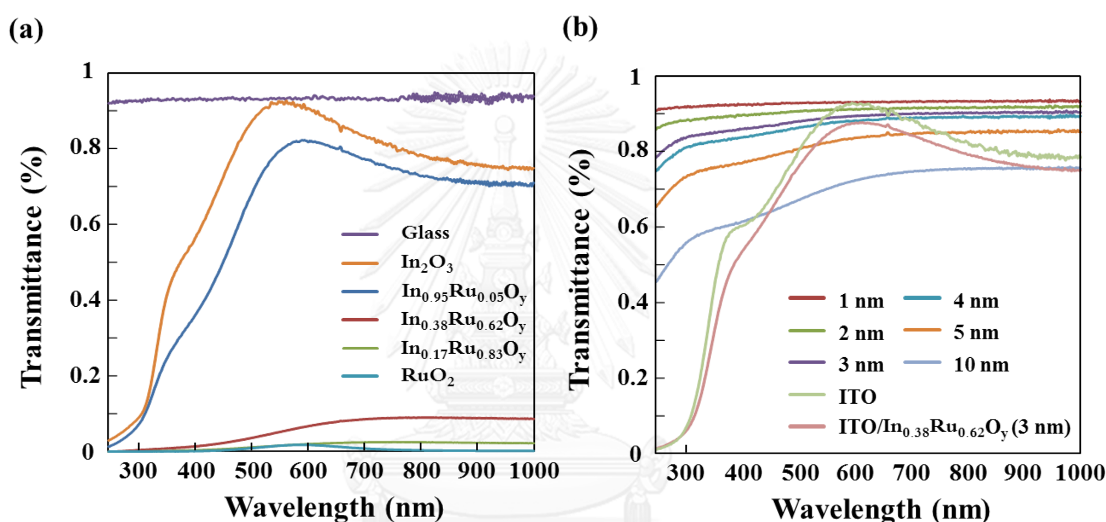

Fig. 5.5 (a) Transmittance of 150-nm-thick as-grown films of In_2O_3, $In_{0.95}Ru_{0.05}O_y$, $In_{0.38}Ru_{0.62}O_y$, and RuO_2. (b) Transmittance of $In_{0.38}Ru_{0.62}O_y$ films as a function of thickness from 1 to 10 nm, a 150-nm-thick ITO film, and an ITO (150 nm)/ultrathin $In_{0.38}Ru_{0.62}O_y$ (3 nm) bilayer.

5.3.3 Electrical properties of $In_{1-x}Ru_xO_y$ thin films

Figure 5.6 shows the specific resistivity behavior of five samples as a function of annealing temperature. Annealing was carried out for 10 min in 3% H_2 atmosphere. The specific resistivity of the as-grown In_2O_3 and $In_{0.95}Ru_{0.05}O_y$ films was too high to

measure, which indicated that these films are insulating. However, the In_2O_3 and $In_{0.95}Ru_{0.05}O_y$ films become conductive as the annealing temperature increases from 150 and 100 °C, respectively. This indicates that oxygen vacancies introduced by removing oxygen from the film generate electrons [172, 173]. Conversely, the $In_{0.38}Ru_{0.62}O_y$, RuO_2 and ITO (150 nm)/ultrathin $In_{0.38}Ru_{0.62}O_y$ (3 nm) bilayer show low resistivity of 1.60×10^{-4}, 1.79×10^{-5}, and 9.20×10^{-5} Ωcm, respectively. The specific resistivity of the $In_{0.38}Ru_{0.62}O_y$ film remained unchanged regardless of annealing temperature.

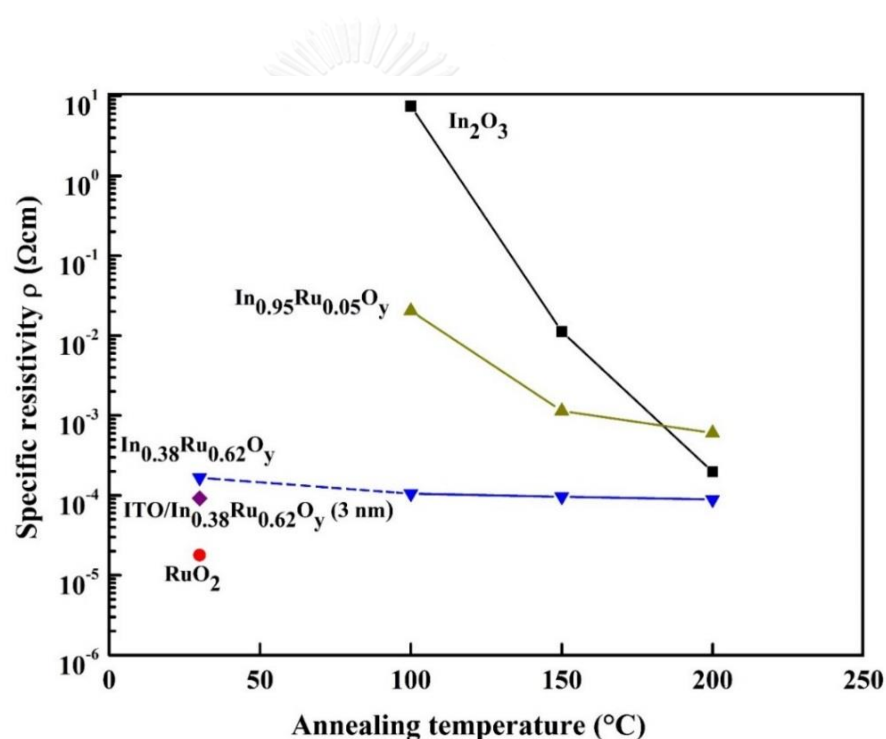

Fig. 5.6 Specific resistivity of In_2O_3, RuO_2, $In_{0.95}Ru_{0.05}O_y$, $In_{0.38}Ru_{0.62}O_y$, and ITO (150 nm)/ultrathin $In_{0.38}Ru_{0.62}O_y$ (3 nm) bilayer as a function of annealing temperature in 3% H_2 atmosphere.

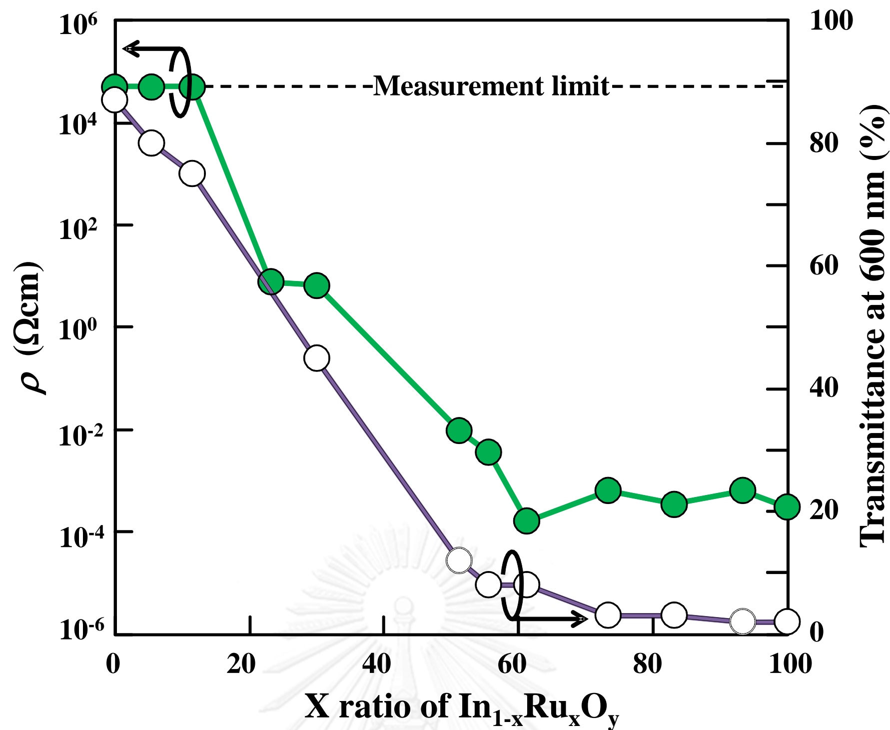

Fig. 5.7 The specific resistivity and transmittance as a function of Ru content in the 150-nm $In_{1-x}Ru_xO_y$ thin films.

Figure 5.7 shows the changes in ρ and the transmittance as a function of Ru content in 150 nm $In_{1-x}Ru_xO_y$ films. It is clear that ρ and the transmittance of the $In_{1-x}Ru_xO_y$ films decreases as the Ru content increases. The $In_{1-x}Ru_xO_y$ films with Ru content over 0.62 had significantly low ρ values of around 10^{-4} Ω cm. However, the transmittance decreases to less than 10% with Ru content over 0.51. These results indicate that the $In_{1-x}Ru_xO_y$ film satisfies the trade-off between ρ and the transmittance. We found that the low transmittance can be solved by decreasing the thickness to 5 nm or less. Also, the thick ITO (150 nm)/ultrathin $In_{0.38}Ru_{0.62}O_y$ (3 nm) bilayer had a low ρ value of 9.2 $\times$ 10^{-5} Ω cm. This suggests that there is a clear interface between the ITO and $In_{0.38}Ru_{0.62}O_y$ layers because there is the same dominant element of indium and because

of the amorphous structure of the $In_{0.38}Ru_{0.62}O_y$ layer. Therefore, the thick ITO and ultrathin $In_{1-x}Ru_xO_y$ bilayer is expected to be a good anode electrode because of the low ρ and high transmittance.

We next examined the C-V characteristics of $In_{1-x}Ru_xO_y$-gate SiO_2 MOS capacitors to estimate $\emptyset_{m,eff}$ of the $In_{1-x}Ru_xO_y$ films. Figure 5.8 illustrates C-V curves of $In_{0.38}Ru_{0.62}O_y$-gate MOS capacitors with different SiO_2 film thicknesses from 5.7 to 12.4 nm. The capacitance of the structures increased as the thickness of the SiO_2 film decreased. Figure 5.8 shows the relationship between V_{fb} and EOT for SiO_2 MOS capacitors with various electrodes such as In_2O_3, $In_{0.95}Ru_{0.05}O_y$, $In_{0.38}Ru_{0.62}O_y$, ITO/$In_{0.38}Ru_{0.62}O_y$, and as-grown RuO_2. The In_2O_3 and $In_{0.95}Ru_{0.05}O_y$-gated MOS capacitors were annealed at 300 °C in 3% H_2 for use as electrodes. The $In_{0.38}Ru_{0.62}O_y$ and ITO/$In_{0.38}Ru_{0.62}O_y$ capacitors were annealed at 300 °C in N_2 atmosphere to suppress the influence of fixed charges. The V_{fb} behaviors of the capacitors without a RuO_2 gate were very similar. The large slope observed for V_{fb} of the RuO_2 gated capacitor is caused by the fixed charges at the SiO_2/Si interface. Then, $\emptyset_{m,eff}$ values were determined by extrapolating the plots of V_{fb} versus EOT using following the equation [174]:

$$V_{fb} = (\emptyset_{m,eff} - \emptyset_{si}) - \emptyset_{ox} / (\varepsilon_0 \varepsilon_{ox}) \times EOT, \quad (5.1)$$

where $\emptyset_{si}$, $\emptyset_{ox}$, ε_0, and ε_{ox} are the fermi level of the silicon substrate, the fixed charges, the permittivity and the dielectric constant of SiO_2, respectively. The $\emptyset_{m,eff}$ of the RuO_2 film is slightly lower compared with reported values [81]. The In_2O_3 and $In_{0.95}Ru_{0.05}O_y$ films show the same $\emptyset_{m,eff}$ of 4.9 eV. In contrast, $\emptyset_{m,eff}$ of the $In_{0.38}Ru_{0.62}O_y$ film is 5.7 eV. The ITO (150-nm)/ultrathin $In_{0.38}Ru_{0.62}O_y$ (3 nm) bilayers also shows a high $\emptyset_{m,eff}$ of over 5.3 eV. Table 5.3 summarizes characteristics such as

the structure, roughness, transmittance, specific resistivity, and $\emptyset_{m,eff}$ of the $In_{1-x}Ru_xO_y$ thin films. We found that the poor transmittance of the $In_{0.38}Ru_{0.62}O_y$ film could be easily improved by decreasing film thickness from 150 nm to 3 nm. Considering to the requirements of anode materials for OEL devices, we suggest that ITO (150-nm)/ultrathin $In_{0.38}Ru_{0.62}O_y$ (3 nm) bilayers show potential as a new anode material.

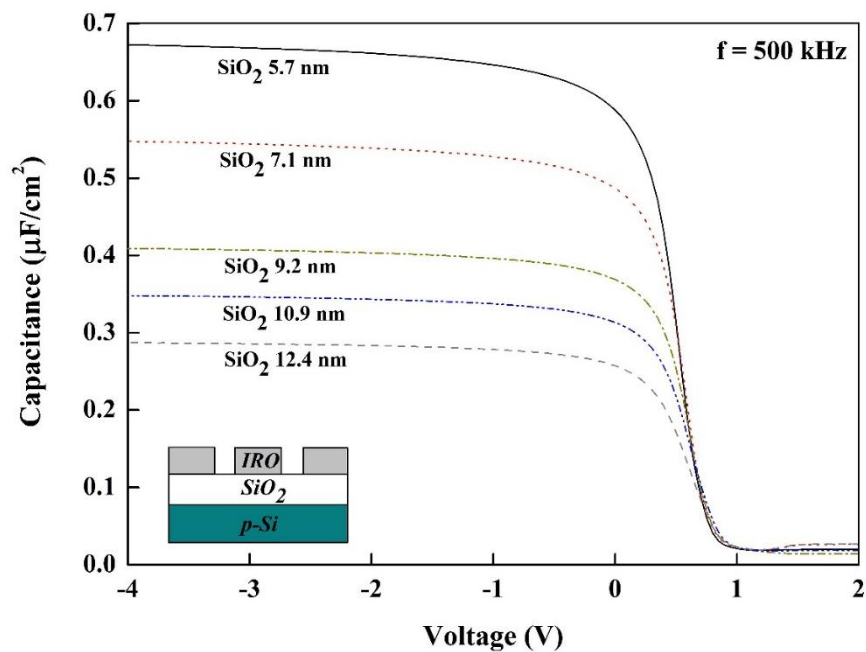

จุฬาลงกรณ์มหาวิทยาลัย
CHULALONGKORN UNIVERSITY

Fig. 5.8 Representative C-V curves for 150-nm-thick $In_{0.38}Ru_{0.62}O_y$-gated MOS capacitors with SiO_2 layers of different thicknesses.

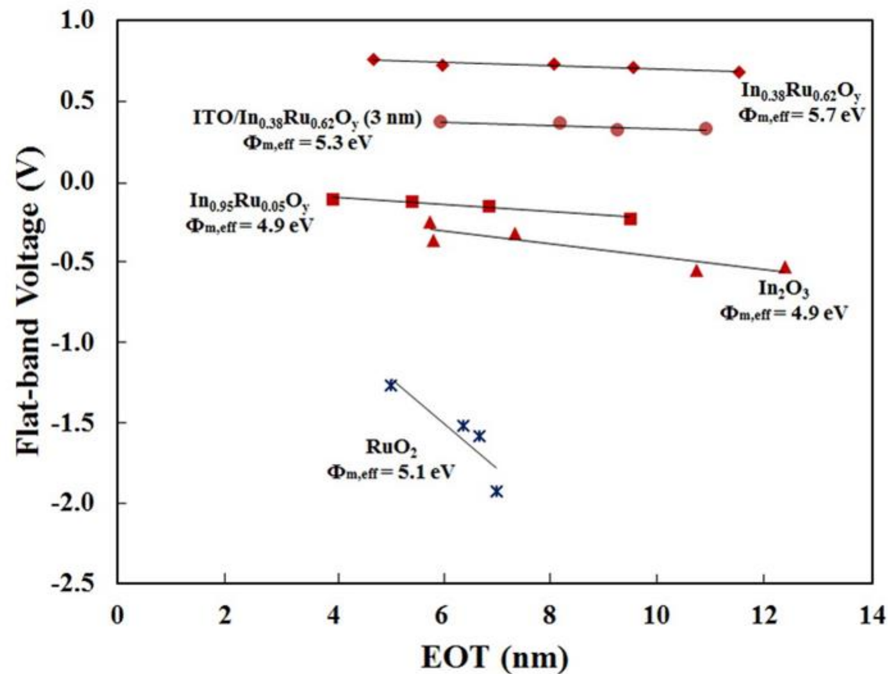

Fig. 5.9 Relationship between V_{fb} and EOT of In_2O_3, RuO_2, $In_{0.95}Ru_{0.05}O_y$, $In_{0.38}Ru_{0.62}O_y$, and ITO (150-nm)/ultrathin $In_{0.38}Ru_{0.62}O_y$ (3 nm) bilayers

Table5.3 Characteristics of $In_{1-x}Ru_xO_y$ film and ITO (150-nm)/ultrathin $In_{0.38}Ru_{0.62}O_y$ (3 nm) bilayers.

Sample	Structure	Roughness (RMS, nm)	Transmittance (%) (at 600 nm)		Specific resistivity ρ (Ωcm)	EWF (eV)
			150 nm	3 nm		
In_2O_3	Body center cubic (BCC)	4.83	92	-	N.D. *	4.9
$In_{0.95}Ru_{0.05}O_y$	Body center cubic (BCC) of In_2O_3	2.88	80	-	N.D. *	4.9
$In_{0.38}Ru_{0.62}O_y$	Amorphous	0.69	8	80	1.60×10^{-4}	5.7
RuO_2	Tetragonal	1.66	0	-	1.79×10^{-5}	5.1
ITO/$In_{0.38}Ru_{0.62}O_y$	-	-	-	80	9.20×10^{-5}	5.3

Remark; * Not determine

5.4 Summary of electrical properties

The electrical and physical properties of the $In_{1-x}Ru_xO_y$ films can be strongly modified by the Ru content. The 150-nm-thick $In_{1-x}Ru_xO_y$ films had an amorphous structure in the wide compositional range of x = 0.3–0.8, a low resistivity in the x = 0.62–1.0, and high transmittance in the narrow range of x = 0.0–0.11. The transmittance of the $In_{0.38}Ru_{0.62}O_y$ film was improved to over 80% when the film thickness was less than 5 nm. We found that thick ITO (150-nm)/ultrathin $In_{0.38}Ru_{0.62}O_y$ (3 nm) bilayers had an effective work function of 5.3 eV, high transmittance of 86%, and low ρ of 9.2 $\times 10^{-5}$ Ω cm. These data indicate that the amorphous thick ITO/ultrathin $In_{0.38}Ru_{0.62}O_y$ bilayers are useful for an anode of OEL devices.

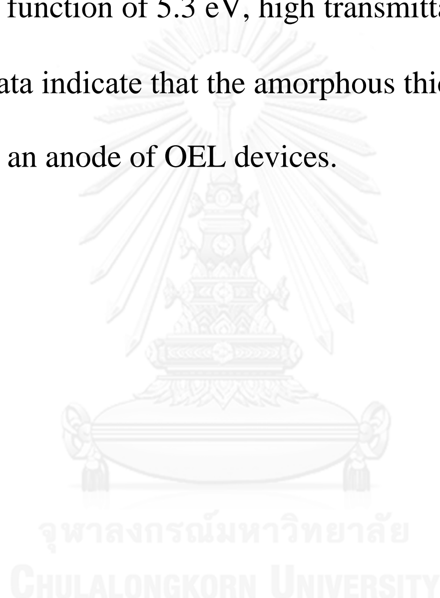

จุฬาลงกรณ์มหาวิทยาลัย
CHULALONGKORN UNIVERSITY

CHAPTER 6
CONCLUSIONS

Addition of the third element into nitride and oxide film to fabricate ternary compound can be done by co-deposition using reactive sputtering. By adjusting process parameters, characteristic of film such as grain structure, crystal structure, atomic ratio of the third element and surface roughness can be designed. With optimum condition, film with the desired properties including mechanical, corrosion, physical, and electrical properties can be produced.

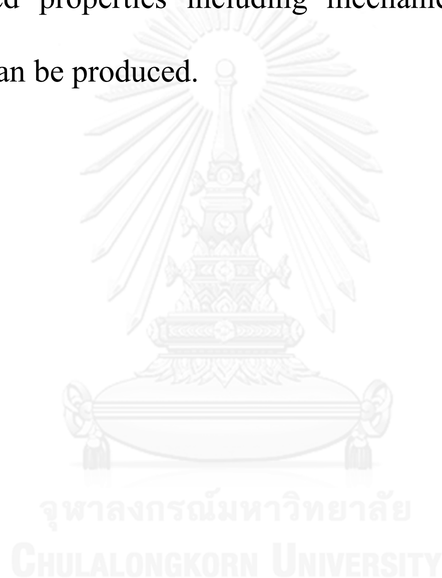
จุฬาลงกรณ์มหาวิทยาลัย
CHULALONGKORN UNIVERSITY

REFERENCES

[1] M. D. Mattox, *The foundation of vacuum coating technology*. New York: Management plus, 2003.

[2] K. Inagawa, "Thin-film preparation. Electric Refractory Materials, Chiba Institute for Super Materials," 2000.

[3] D. L. Smith, *Thin-Film deposition Principles & Practice*. Boston: McGraw Hill, 1995.

[4] C. Mitterer, J. Komenda-Stallmaier, P. Losbichler, P. Schmölz, W. S. M. Werner, and H. Störi, "Sputter deposition of decorative boride coatings," *Vacuum,* vol. 46, pp. 1281-1294, 11/1995.

[5] D. J. Li, J. Yang, X. H. Zhang, and M. Cao, "Nanoscale ZrC/ZrB2 multilayered coating prepared by magnetron sputtering," *J. Vac. Sci. Technol. B 9,* vol. 25, pp. 11-13, 2007.

[6] L. Voss, S. J. Pearton, F. Ren, and I. I. Kravchenko, "ZrB2-based Ohmic contacts to p-GaN," *Applied Surface Science,* vol. 253, pp. 1934-1938, 12/15/ 2006.

[7] J. S. Wright, R. Khanna, K. Ramani, V. Cranciun, R. Singh, D. P. Norton*, et al.*, "ZrB2/Pt/Au Ohmic contacts on bulk, single-crystal ZnO," *Applied Surface Science,* vol. 253, pp. 2465-2469, 12/30/ 2006.

[8] I. Radović, Y. Serruys, Y. Limoge, N. Bibić, S. Poissonnet, O. Jaoul*, et al.*, "Stoichiometric SiO2 thin films deposited by reactive sputtering," *Materials Chemistry and Physics,* vol. 104, pp. 172-176, 7/15/ 2007.

[9] A. S. Ryzhikov, R. B. Vasiliev, M. N. Rumyantseva, L. I. Ryabova, G. A. Dosovitsky, A. M. Gilmutdinov*, et al.*, "Microstructure and electrophysical properties of SnO2, ZnO and In2O3 nanocrystalline films prepared by reactive magnetron sputtering," *Materials Science and Engineering: B,* vol. 96, pp. 268-274, 12/1/ 2002.

[10] T. Kohara, H. Tamagaki, Y. Ikari, and H. Fujii, "Deposition of α-Al2O3 hard coatings by reactive magnetron sputtering," *Surface and Coatings Technology,* vol. 185, pp. 166-171, 7/22/ 2004.

[11] Y. Hoshi, D. shihara, T. Sakai, O. Kamiya, and H. Lei, "High rate reaction deposition of TiO2 films using two sputtering sources," vol. 84, pp. 1377-1380, 2014.

[12] V. Ezhil Selvi, V. K. William Grips, and H. C. Barshilia, "Electrochemical behavior of superhard nanocomposite coatings of TiN/Si3N4 prepared by reactive DC unbalanced magnetron sputtering," *Surface and Coatings Technology,* vol. 224, pp. 42-48, 6/15/ 2013.

[13] Q. Fang and J. Y. Zhang, "Nano-porous TiN thin films deposited by reactive sputtering method," *International Journal of Inorganic Materials,* vol. 3, pp. 1193-1196, 12/2001.

[14] E. Forniés, R. Escobar Galindo, O. Sánchez, and J. M. Albella, "Growth of CrNx films by DC reactive magnetron sputtering at constant N2/Ar gas flow," *Surface and Coatings Technology,* vol. 200, pp. 6047-6053, 5/22/ 2006.

[15] G. F. Iriarte, D. F. Reyes, D. González, J. G. Rodriguez, R. García, and F. Calle, "Influence of substrate crystallography on the room temperature synthesis of

AlN thin films by reactive sputtering," *Applied Surface Science,* vol. 257, pp. 9306-9313, 9/1/ 2011.

[16] N. C. Zoita, V. Braic, M. Danila, A. M. Vlaicu, C. Logofatu, C. E. A. Grigorescu*, et al.*, "Influence of film thickness on the morphological and electrical properties of epitaxial TiC films deposited by reactive magnetron sputtering on MgO substrates," *Journal of Crystal Growth,* vol. 389, pp. 92-98, 3/1/ 2014.

[17] A. V. Stanishevsky, M. J. Walock, Y. Zou, L. Imhoff, A. Zairi, and C. Nouveau, "Growth of WC–Cr–N and WC–Al–N coatings in a RF-magnetron sputtering process," *Vacuum,* vol. 90, pp. 129-134, 4/2013.

[18] A. Mahmood, S. Muhl, L. E. Sansores, and E. Andrade, "Dependency of reactive magnetron-sputtered SiC film quality on the deposition parameters," *Thin Solid Films,* vol. 373, pp. 180-183, 9/3/ 2000.

[19] M. Ürgen and A. F. Çakir, "The effect of heating on corrosion behavior of TiN- and CrN-coated steels," *Surface and Coatings Technology,* vol. 96, pp. 236-244, 11/25/ 1997.

[20] L. Cunha, M. Andritschky, K. Pischow, and Z. Wang, "Microstructure of CrN coatings produced by PVD techniques," *Thin Solid Films,* vol. 355–356, pp. 465-471, 11/1/ 1999.

[21] W.-J. Chou, G.-P. Yu, and J.-H. Huang, "Corrosion resistance of ZrN films on AISI 304 stainless steel substrate," *Surface and Coatings Technology,* vol. 167, pp. 59-67, 4/1/ 2003.

[22] S. Rudenja, C. Leygraf, J. Pan, P. Kulu, E. Talimets, and V. Mikli, "Duplex TiN coatings deposited by arc plating for increased corrosion resistance of stainless steel substrates," *Surface and Coatings Technology,* vol. 114, pp. 129-136, 5/12/ 1999.

[23] Y. Wang and D. O. Northwood, "An investigation of the electrochemical properties of PVD TiN-coated SS410 in simulated PEM fuel cell environments," *International Journal of Hydrogen Energy,* vol. 32, pp. 895-902, 5/2007.

[24] H. C. Barshilia, M. Surya Prakash, A. Poojari, and K. S. Rajam, "Corrosion behavior of nanolayered TiN/NbN multilayer coatings prepared by reactive direct current magnetron sputtering process," *Thin Solid Films,* vol. 460, pp. 133-142, 7/22/ 2004.

[25] D. A. Jones, *Electrochemical kinetics of corrosion*. Macmillan Publishing Company: New York 1992.

[26] F. Lang and Z. Yu, "The corrosion resistance and wear resistance of thick TiN coatings deposited by arc ion plating," *Surface and Coatings Technology,* vol. 145, pp. 80-87, 8/1/ 2001.

[27] H. A. Jehn, "Improvement of the corrosion resistance of PVD hard coating–substrate systems," *Surface and Coatings Technology,* vol. 125, pp. 212-217, 3/2000.

[28] M. D. Mattox, *Handbook of physical vapor deposition (PVD) processing*, 2 ed. USA: William Andrew, 2010.

[29] M. Nordin, M. Larsson, and S. Hogmark, "Mechanical and tribological properties of multilayered PVD TiN/CrN," *Wear,* vol. 232, pp. 221-225, 10/ 1999.

[30] "Max Phase." From wikipedia, the free encyclopedia ", [online], Ed., ed: Available: http://en.wikipedia.org/wiki/MAX_phases#mediaviewer/File:MAX_phases_periodic_table.png.

[31] P. Eklund, Beckers,M., Jansson, U., Hogberg, H.,Hultman,L.,, "The $M_{n+1}AX_n$ phase: Materials science and thin -film processing," *Thin solid films,* vol. 518, pp. 1851-1878, 2010.

[32] K. Chu, P. W. Shum, and Y. G. Shen, "Substrate bias effects on mechanical and tribological properties of substitutional solid solution (Ti, Al)N films prepared by reactive magnetron sputtering," *Materials Science and Engineering: B,* vol. 131, pp. 62-71, 7/15/ 2006.

[33] D. Li, J. Chen, C. Zou, J. Ma, P. Li, and Y. Li, "Effects of Al concentrations on the microstructure and mechanical properties of Ti–Al–N films deposited by RF-ICPIS enhanced magnetron sputtering," *Journal of Alloys and Compounds,* vol. 609, pp. 239-243, 10/5/ 2014.

[34] P. W. Shum, W. C. Tam, K. Y. Li, Z. F. Zhou, and Y. G. Shen, "Mechanical and tribological properties of titanium–aluminium–nitride films deposited by reactive close-field unbalanced magnetron sputtering," *Wear,* vol. 257, pp. 1030-1040, 11/2004.

[35] L. Cunha, M. Andritschky, L. Rebouta, and R. Silva, "Corrosion of TiN, (TiAl)N and CrN hard coatings produced by magnetron sputtering," *Thin Solid Films,* vol. 317, pp. 351-355, 4/1/ 1998.

[36] R. M. Souto and H. Alanyali, "Electrochemical characteristics of steel coated with TiN and TiAlN coatings," *Corrosion Science,* vol. 42, pp. 2201-2211, 12// 2000.

[37] S. Liscano, L. Gil, O. A. León, M. Cruz, and M. H. Staia, "Corrosion performance of duplex treatments based on plasma nitriding and PAPVD TiAlN coating," *Surface and Coatings Technology,* vol. 201, pp. 4419-4423, 12/20/ 2006.

[38] L. Cunha, M. Andritschky, L. Rebouta, and K. Pischow, "Corrosion of CrN and TiAlN coatings in chloride-containing atmospheres," *Surface and Coatings Technology,* vol. 116–119, pp. 1152-1160, 9/1999.

[39] H. Scheerer, H. Hoche, E. Broszeit, and C. Berger, "Tribological properties of sputtered CrN coatings under dry sliding oscillation motion at elevated temperatures," *Surface and Coatings Technology,* vol. 142–144, pp. 1017-1022, 7/ 2001.

[40] S. C. Tung and H. Gao, "Tribological characteristics and surface interaction between piston ring coatings and a blend of energy-conserving oils and ethanol fuels," *Wear,* vol. 255, pp. 1276-1285, 8/2003.

[41] J. Vetter, R. Knaup, H. Dweletzki, E. Schneider, and S. Vogler, "Hard coatings for lubrication reduction in metal forming," *Surface and Coatings Technology,* vol. 86–87, Part 2, pp. 739-747, 12/15/ 1996.

[42] B. Navinšek and P. Panjan, "Novel applications of CrN (PVD) coatings deposited at 200 °C," *Surface and Coatings Technology,* vol. 74–75, Part 2, pp. 919-926, 10/1995.

จุฬาลงกรณ์มหาวิทยาลัย
CHULALONGKORN UNIVERSITY

[43] C. Liu, A. Leyland, Q. Bi, and A. Matthews, "Corrosion resistance of multi-layered plasma-assisted physical vapour deposition TiN and CrN coatings," *Surface and Coatings Technology,* vol. 141, pp. 164-173, 6/18/ 2001.

[44] D. W. Hoffman and J. A. Thornton, "internal stresses in Cr, Mo, Ta, and Pt films deposited by sputtering from a planar magnetron source," *Journal of Vacuum Science and Technology* vol. 20, pp. 355-358, 1982.

[45] D. W. Hoffman and M. R. Gaerttner, "Modification of evaporated chromium by concurrent ion bombardment," *Journal of Vacuum Science and Technology* vol. 17, pp. 425-428, 1980.

[46] R. S. Berg and G. J. Kominiak, "Surface texturing by sputter etching," *Journal of Vacuum Science and Technology,* vol. 13, pp. 403-405, 1976.

[47] P. Ziermann and E. Kay, "Model of bias sputtering in a dc-triode configuration applied to the production of Pd films," *Journal of Vacuum Science and Technology* vol. 21, pp. 828-832, 1982.

[48] J. M. E. Harper, J. J. Cuomo, R. J. Gambino, and H. R. Kaufman, *in "Ion Bombardment Modification of surface: Fundamentals and Application".* Amsterdam: Elsevier, 1984.

[49] J. L. Vossen and W. Kern, *Thin Film Process II: sputtering deposition process*. San Diego Academic press, 1991.

[50] J. A. Thornton, "High Rate Thick Film Growth," *Annual Review of Materials Science,* vol. 7, pp. 239-260, 1977.

[51] J. A. Thornton, "Influence of apparatus geometry and deposition conditions on the structure and topography of thick sputtered coatings," *Journal of Vacuum Science and Technology* vol. 11, pp. 666-670, 1974.

[52] A. G. Dirks and H. J. Leamy, "Columnar microstructure in vapor-deposited thin films," *Thin Solid Films,* vol. 47, pp. 219-233, 12/15/ 1977.

[53] P. S. Vincett, W. A. Barlow, and G. G. Roberts, "Structure and properties of vacuum-deposited thin films: A new basic relationship," *J. Appl. Phys. ,* vol. 48, pp. 3800-3806, 1977.

[54] M. H. Francombe, *in "Epitaxial Growth".* New York: Academic Press, 1975.

[55] R. Messier, A. P. Giri, and R. A. Roy, "Revised structure zone model for thin film physical structure," *Journal of Vacuum Science and Technology,* vol. A2, pp. 500-503, 1984.

[56] R. Messier, "Toward quantification of thin film morphology," *Journal of Vacuum Science and Technology,* vol. A4, pp. 490-495, 1986.

[57] R. D. Bland, G. J. Kominiak, and M. D. Mattox, "Effect of ion bombardment during deposition on thick metal and ceramic deposits," *Journal of Vacuum Science and Technology* vol. 11, p. 671, 1974.

[58] M. D. Mattox and G. J. Komuniak, "Structure modification by ion bombardment during deposition," *Journal of Vacuum Science and Technology* vol. 9, pp. 528-531, 1972.

[59] G. J. Kominiak and M. D. Mattox, "Physical properties of thick sputter-deposited glass films," *J. Electrochem* vol. 120, p. 1535, 1973.

[60] J. A. Thornton, "Influence of substrate temperature and deposition rate on structure of thick sputtered Cu coatings," *Journal of Vacuum Science and Technology* vol. 12, pp. 830-835, 1975.

[61] D. W. Hoffman and J. A. Thornton, "The compressive stress transition in Al, V, Zr, Nb and W metal films sputtered at low working pressures," *Thin Solid Films,* vol. 45, pp. 387-396, 9/1/ 1977.

[62] K. Tominaga, S. Iwamura, Y. Shintani, and O. Tada, "Energy analysis of high-energy neutral atoms in the sputtering of ZnO and BaTiO3," *Jpn. J. Appl. Phys.* , vol. 21, p. 688, 1982.

[63] J. A. Thornton, "The influence of bias sputter parameters on thick copper coatings deposited using a hollow cathode," *Thin Solid Films,* vol. 40, pp. 335-344, 1/1977.

[64] I. A. Tambasov, V. G. Myagkov, A. A. Ivanenko, I. V. Nemtsev, L. E. Bykova, G. N. Bondarenko*, et al.*, "Structure and optical properties of thin In2O3 films produced by auto wave oxidation," *Semiconductors,,* vol. 47, pp. 569-573, 2013.

[65] T. Kukano, T. Motohiro, and H. Hashizume, "Enhanced carrier densities in indium thin oxide films covered with nanoparticles of fluorine-doped tin oxide for transparent conducting electrodes," *Jpn. J. Appl.Phys,* vol. 44, pp. 8747-8752, 2005.

[66] H. Kim, J. S. Horwitz, G. P. Kashto, S. B. Qadri, Z. H. Kafafi, and D. B. Chrisey, "Transparent conducting Zr-doped In2O3 thin films for organic light-emitting diodes," *Appl. Phys. Lett,* vol. 78, pp. 1050-1052, 2001.

[67] T. J. Coutts, D. L. Young, and X. N. Li, "Characterization of transparent conducting oxides," *Mater. Res. Bull,* vol. 25, pp. 58-65, 2000.

[68] A. Chaoumead, B.-H. Joo, D.-J. Kwak, and Y.-M. Sung, "Structure and electrical properties of sputtering power and gas pressure on Ti- dope In2O3 transparent conductive films by RF magnetron sputtering," *Applied Surface Science* vol. 275, pp. 227-232, 2013.

[69] L. Chkoda, C. Heske, M. Sokolowski, E. Umbach, F. Steuber, J. Staudigel*, et al.*, "Work function of ITO substrates and band-offsets at the TPD/ITO interface determined by photoelectron spectroscopy," *Synthetic Metals,* vol. 111–112, pp. 315-319, 6/1/ 2000.

[70] E. Elangovan, G. Gonçalves, R. Martins, and E. Fortunato, "RF sputtered wide work function indium molybdenum oxide thin films for solar cell applications," *Solar Energy,* vol. 83, pp. 726-731, 5/2009.

[71] J. H. Kim, T. Y. Seong, and H. K. Kim, "Effects of rapid thermal annealing on electrical, optical, and structural properties of Ni-doped In2O3 anodes for bulk heterojunction organic solar cells," *J. Vac. Sci. Technol.* , vol. A 31, 2013.

[72] G. F. Li, Q. Zhang, F. Yu, C. Liu, and H. R. Wu, "Organic light-emitting device with surface-modified tungsten-doped indium oxide anode," *Electron. Lett* vol. 44, p. 13, 2008.

[73] J. H. Kim, T. Y. Seong, and H. K. Kim, "Effects of rapid thermal annealing on electrical, optical, and structural properties of Ni-doped In2O3 anodes for bulk heterojunction organic solar cells," *J. Vac. Sci. Technol.,* vol. A 31, 2013.

[74] G. F. Li, Q. Zhang, F. Yu, C. Liu, and H. R. Wu, "Organic light-emitting device with surface-modified tungsten-doped indium oxide anode," *Electronic Letters* vol. 44, p. 13, 2008.

[75] Y. Chen, X. Zhou, X. Zhao, X. He, and X. Gu, "Crystallite structure, surface morphology and optical properties of In2O3–TiO2 composite thin films by sol–

gel method," *Materials Science and Engineering: B,* vol. 151, pp. 179-186, 6/25/ 2008.

[76] E. V. Jelenkovic and K. Y. Tong, "Thermally grown ruthenium oxide thin film", *J. Vac. Sci. Technol.,* vol. B22, p. 2319, 2004.

[77] K. J. Park, J. M. Doub, T. Gougousi, and G. N. Parsons, "Microcontact patterning of ruthenium gate electrodes by selective area atomic layer deposition," *Applied Physics Letters* vol. 86, p. 51903, 2005.

[78] R. Jha, J. H. Lee, B. Chen, H. Lazar, J. Gurganus, N. Biswas*, et al.*, "Evalution of Fermi level pining in low mid gap and high workfunction metal gate electrodes on ALD and MOCVD HfO2 under high temperature exposure," presented at the International Electron Devices Meeting, 2004.

[79] K. Fröhlich, K. Husekova, D. Machajdik, J. C. Hooker, N. Perez, M. Fanciulli*, et al.*, "Ru and RuO2 gate electrodes for advanced CMOS technology," *Materials Science and Engineering: B,* vol. 109, pp. 117-121, 6/15/ 2004.

[80] Y.-S. Suh, H. Lazar, B. Chen, J. H. Lee, and V. Misra, "Electrical characteristics of HfO2 dielectrics with Ru metal gate electrodes," *Journal of The Electrochemical Society,* vol. 152 (9) pp. F138-F141, 2005.

[81] T. Nabatame, K. Segawa, M. Kadoshima, H. Takaba, K. Iwamoto, S. Kimura*, et al.*, "The effect of oxygen in Ru gate electrode on effective work function of Ru/HfO2 stack structure," *Materials Science in Semiconductor Processing,* vol. 9, pp. 975-979, 12/ 2006.

[82] C. Chantharangsi, S. Denchitcharoen, S. Chaiyakun, and P. Limsuwan, "Structure and Surface Morphology of Cr-Zr-N Thin Films Deposited by Reactive DC Magnetron Sputtering," *Procedia Engineering,* vol. 32, pp. 868-874, /2012.

[83] D.-Y. Wang, C.-L. Chang, C.-H. Hsu, and H.-N. Lin, "Synthesis of (Ti, Zr)N hard coatings by unbalanced magnetron sputtering," *Surface and Coatings Technology,* vol. 130, pp. 64-68, 8/1/ 2000.

[84] J. V. Ramana, S. Kumar, C. David, and V. S. Raju, "Structure, composition and microhardness of (Ti,Zr)N and (Ti,Al)N coatings prepared by DC magnetron sputtering," *Materials Letters,* vol. 58, pp. 2553-2558, 8/2004.

[85] S. M. Aouadi, K. C. Wong, K. A. R. Mitchell, F. Namavar, E. Tobin, D. M. Mihut*, et al.*, "Characterization of titanium chromium nitride nanocomposite protective coatings," *Applied Surface Science,* vol. 229, pp. 387-394, 5/15/ 2004.

[86] Y. Lee, H. Terashima, Y. Shimodaira, K. Teramura, M. Hara, H. Kobayashi*, et al.*, "Zinc germanium oxynitride as a photocatalyst for overall water splitting under visible light," *The Journal of physical chemistry C,* vol. 7, pp. 1042-1048, 2007.

[87] S. Ulrich, H. Ehrhardt, T. Theel, J. Schwan, S. Westermeyr, M. Scheib*, et al.*, "Phase separation in magnetron sputtered superhard BCN thin films," *Diamond and Related materials* vol. 7, pp. 839-844, 1998.

[88] V.-H. Pham, S.-W. Yook, Y. Li, G. Jeon, J.-J. Lee, H.-E. Kim*, et al.*, "Improving hardness of biomedical Co–Cr by deposition of dense and uniform TiN films using negative substrate bias during reactive sputtering," *Materials Letters,* vol. 65, pp. 1707-1709, 6/15/ 2011.

[89] M. Ohring, *Materials Science of Thin film: Deposition & Structure (2nd)*. USA: Academic Press, Inc., 2002.

[90] Microbeam techniques in geology. [Online]. Available: http://www4.nau.edu/-microanalysis/microprobe-sem/history.html

[91] B. D. Cullity and S. R. Stock, *Elements of X-ray diffraction: Precise parameter measurements*. New Jersey Prentice Hall, 2001.

[92] B. Bhushan, *Nanotribology and Nanomechanics I; measurement techniques and nanomechanics*, 1 ed. Ohio: Springer, 2011.

[93] G. Binnig, C. F. Quate, and C. Gerber, "Atomic force microscope," *Phys. Rev. Lett.* , vol. 56 pp. 930–933., 1986.

[94] Y. Martin, C. C. Williams, and H. K. Wickramasinghe, "Atomic force microscope-force mapping and profiling on a sub 100 Å scale," *J. Appl. Phys,* vol. 61, pp. 4723–4729, 1987.

[95] D. Sarid and V. Elings, "Review of scanning force microscopy," *J. Vac. Sci. Technol. B 9,* pp. 431–437, 1991.

[96] F. J. Giessibl, "Atomic resolution of the silicon (111)–(7×7) surface by atomic force microscopy," *Science 267,* pp. 68–71, 1995.

[97] B. Anczykowski, D. Kreuger, K. L. Babcock, and H. Fuchs, "Basic properties of dynamic force spectroscopy with the scanning force microscope in experiment and simulation," *Ultramicroscopy,* vol. 66, pp. 251–259, 1996.

[98] CSM Instruments Revetest Scratch Tester, CSM Instruments [Online]. Available: http:// www. azonano. com /equipment-details.aspx

[99] CSM Instruments Nanoindentation Tester (NHT), CSM Instruments [Online]. Available: http:// www. csm- instructurements.com/en/ttx

[100] E. Barsoukov and J. Ross Macdonald, *Impedance spectroscopy*, second ed. New Jersey: Jon Wiley & Sons, 2005.

[101] F. V. Lvovich, *Impedance spectroscopy: Applications to electrochemical and dielectric phenomena*: New Jersey, 2012.

[102] J. A. Bard and R. L. Faulkner, *Electrochemical methods: Fundamentals and applications* 2ed. USA John Wiley & Sons, 2001.

[103] G. L. Moore, *Analytical Spectroscopy library; Introduction to Inductively Coupled Plasma Atomic Emission Spectrometry*. New York: Elsevier Science publisher B.V., 1989.

[104] R. M. A. Azzam and N. M. Bashara, *Ellipsometry and polarized Light*. Amsterdam: North-Holland, 1997.

[105] H. G. Tompkins and W. A. McGahan, *Spectroscopic Ellipsometry and reflectometry: A user's Guide*. New York John Wiley & Sons, Inc., 1999.

[106] H. G. Tompkins and E. A. Irene, *Handbook of Ellipsometry*. New York Willian Andrew, 2005.

[107] M. Schubert, *Infrared Ellipsometry on Semiconductor Layer Structures; Phonons, Plasmons, and Polaritions*. Heidelberg: Springer, 2004.

[108] H. Fujiwara, *Spectroscopic Ellipsometry: Principles and Applications*. English: John Wiley& Sons, Inc, 2007.

[109] F. M. Smits, "Measurement of sheet resistivity with the four-point probe," *Bell System Technical Journal* vol. 34, pp. 711-718, 1985.

[110] K. D. Schroder, *Semiconductor material and device characterization* New York John Wiley & Sons, Inc., 2006.

[111] L. Stauffer. (2014). *Fundamentals of semiconductor C-V measurements (KeithleyInstruments)*.Available:http://evaluationengineering.com/articles/200812/fundamentals-of-semiconductor-c-v-measurements.php
[112] Analysis of semiconductor capacitance characteristics (Using the HP 4280A 1MHz C Meter/ C-V plotter, Application Note 322) [Online]. Available: http://wiki.epfl.ch/carplat/documents/HP_AN_322.pdf
[113] R. L. O. Basso, H. O. Pastore, V. Schmidt, I. J. R. Baumvol, S. A. C. Abarca, F. S. de Souza*, et al.*, "Microstructure and corrosion behaviour of pulsed plasma-nitrided AISI H13 tool steel," *Corrosion Science,* vol. 52, pp. 3133-3139, 9/2010.
[114] T. Bell, "Ferritic nitrocarburizing," *Heat Treatment of Metals,* vol. 2, pp. 39-49, 1975.
[115] R. L. O. Basso, "Effect of carbon on the compound layer properties of AISI H13 tool steel in pulsed plasma nitrocarburizing," *Plasma Process and Polymers,* vol. 451, pp. 5728-5731, 2007.
[116] A. Suhadi, C. X. Li, and T. Bell, "Austenitic plasma nitrocarburising of carbon steel in N2–H2 atmosphere with organic vapour additions," *Surface and Coatings Technology,* vol. 200, pp. 4397-4405, 4/10/ 2006.
[117] L. C. F. Canale, R. A. Mesquita, and G. E. Totten, *Failure analysis in tool steels*. Ohio: Material Park, 2008.
[118] B. Navinšek, P. Panjan, and A. Cvelbar, "Characterization of low temperature CrN and TiN (PVD) hard coatings," *Surface and Coatings Technology,* vol. 74–75, Part 1, pp. 155-161, 9/1995.
[119] K. P. Purushotham, L. P. Ward, N. Brack, P. J. Pigram, P. Evans, H. Noorman*, et al.*, "The effect of MEVVA ion implantation of Zr on the corrosion behaviour of PVD TiN coatings," *Corrosion Science,* vol. 50, pp. 8-14, 1/2008.
[120] L. Aihua, D. Jianxin, C. Haibing, C. Yangyang, and Z. Jun, "Friction and wear properties of TiN, TiAlN, AlTiN and CrAlN PVD nitride coatings," *International Journal of Refractory Metals and Hard Materials,* vol. 31, pp. 82-88, 3/2012.
[121] R. Wuhrer and W. Y. Yeung, "A comparative study of magnetron co-sputtered nanocrystalline titanium aluminium and chromium aluminium nitride coatings," *Scripta Materialia,* vol. 50, pp. 1461-1466, 6/2004.
[122] O. N. B. Sundaram, P. Meena, V. Veeravazhuthi, and K. T. Selvan, *Synthesis and characterization of Cr-N coating prepared by plasma processes*. New Delhi Allied Publishers PVT.LTD, 2004.
[123] A. Cavaleiro and J. T. M. De Hosson, *Nanostructure coating: Characterization of TiN and TiN-(Ti,Al)N multilayer*. New York Springer, 2006.
[124] A. O. Sergici and N. X. Randall, "Scratch testing of coating," in *In Proceeding of the 3rd International Brazing and Soldering Conference*, Ohio, 2006, pp. 41-43.
[125] M. M. Donald, *Atomistic film growth and some growth- related film properties*. United Kingdom Elsevier, 2010.
[126] J. A. Thronton, "High rate thick film growth," *Annual Review in Materials Science,* vol. 7, pp. 239-260, 1977.
[127] O. Milton, *Substrate surface and thin-film nucleation*. New Jersey Academic Press, 2002.

Chulalongkorn University

[128] W. C. Oliver and G. M. Pharr, "Advances in understanding and refinement to methodology," *Journal of Material Research* vol. 19, pp. 3-20, 2004.
[129] S. Sveen, J. M. Andersson, R. M'Saoubi, and M. Olsson, "Scratch adhesion characteristics of PVD TiAlN deposited on high speed steel, cemented carbide and PCBN substrates," *Wear,* vol. 308, pp. 133-141, 11/30/ 2013.
[130] A. I. Fernández-Abia, J. Barreiro, J. Fernández-Larrinoa, L. N. L. d. Lacalle, A. Fernández-Valdivielso, and O. M. Pereira, "Behaviour of PVD Coatings in the Turning of Austenitic Stainless Steels," *Procedia Engineering,* vol. 63, pp. 133-141, 2013.
[131] L. A. Dobrzanski, M. Polok, P. Panjan, S. Bugliosi, and M. Adamiak, "Improvement of wear resistance of hot work steels by PVD coatings deposition," *Journal of Materials Processing Technology,* vol. 155–156, pp. 1995-2001, 11/30/ 2004.
[132] S. Rossi, L. Fedrizzi, M. Leoni, P. Scardi, and Y. Massiani, "(Ti,Cr)N and Ti/TiN PVD coatings on 304 stainless steel substrates: wear-corrosion behaviour," *Thin Solid Films,* vol. 350, pp. 161-167, 8/15/ 1999.
[133] M. Nordin, M. Herranen, and S. Hogmark, "Influence of lamellae thickness on the corrosion behaviour of multilayered PVD TiN/CrN coatings," *Thin Solid Films,* vol. 348, pp. 202-209, 7/6/ 1999.
[134] C. Mendibide, P. Steyer, and J. P. Millet, "Formation of a semiconductive surface film on nanomultilayered TiN/CrN coatings and its correlation with corrosion protection of steel," *Surface and Coatings Technology,* vol. 200, pp. 109-112, 10/1/ 2005.
[135] K. Taweesup, S. tungasmita, N. Yongvanich, G. Lothongkum, and P. Visuttipitukul, "Mechanical and corrosion resistance of (Ti,Cr)N grown by DC magnetron sputter on H13 tool steel," *Material Testing,* vol. 07-08 pp. 588-592, 2013.
[136] Y. Pei, D. Jianxin, W. Ze, L. Shipeng, X. Youqiang, and Z. Jun, "Friction and wear behavior of the PVD (Zr,Ti)N coated cemented carbide against 40 Cr hardened steel," *International Journal of Refractory Metals and Hard Materials,* vol. 35, pp. 213-200, 2012.
[137] Y. W. Lin, J.-H. Huang, and G. P. Yu, "Effect of nitrogen flow rate on properties of nanostructure TiZrN thin films produced by radio frequency magnetron sputtering " *Thin solid films* vol. 518, pp. 7308-7311, 2010.
[138] E. Machnikova, M. Pazderova, M. Bazzaoui, and N. Hackerman, "Corrosion study of PVD coatings and conductive polymer deposited on mild steel: Part I: Polypyrrole," *Surface and Coatings Technology,* vol. 202, pp. 1543-1550, 1/15/ 2008.
[139] P. K. Vencovsky, R. Sanchez, J. R. T. Branco, and M. Galvano, "Enhancing corrosion resistance of PVD-coated tools," *Surface and Coatings Technology,* vol. 108–109, pp. 599-603, 10/10/ 1998.
[140] J. Creus, A. Billard, and F. Sanchette, "Corrosion behaviour of amorphous Al–Cr and Al–Cr–(N) coatings deposited by dc magnetron sputtering on mild steel substrate," *Thin Solid Films,* vol. 466, pp. 1-9, 11/1/ 2004.
[141] M. G. Fontana, *Corrosion Engineering*, Third ed. Singapore: McGraw-Hill, 1986.

[142] C. Liu, Q. Bi, A. Leyland, and A. Matthews, "An electrochemical impedance spectroscopy study of the corrosion behaviour of PVD coated steels in 0.5 N NaCl aqueous solution: Part II.: EIS interpretation of corrosion behaviour," *Corrosion Science,* vol. 45, pp. 1257-1273, 6/2003.

[143] V. K. William Grips, H. C. Barshilia, V. E. Selvi, Kalavati, and K. S. Rajam, "Electrochemical behavior of single layer CrN, TiN, TiAlN coatings and nanolayered TiAlN/CrN multilayer coatings prepared by reactive direct current magnetron sputtering," *Thin Solid Films,* vol. 514, pp. 204-211, 8/30/ 2006.

[144] J.-Y. Wang, C.-M. Liu, W.-K. Chen, Y.-M. Liu, and M.-D. Ger, "Microstructure and corrosion resistance of anodized Mg-9 mass% Li-1 mass% Zn alloy," *Materials Transaction* vol. 49, pp. 1355-1358, 2008.

[145] C. Liu, Q. Bi, and A. Matthews, "EIS comparison on corrosion performance of PVD TiN and CrN coated mild steel in 0.5 N NaCl aqueous solution," *Corrosion Science,* vol. 43, pp. 1953-1961, 10/2001.

[146] C. H. Tsai and F. Mansfeld, "Determination of coating deterioration with EIS: part II development of a method for field testing of protective coating," *Corrosion Science,* vol. 49, 1993.

[147] Y. H. Yoo, J. H. Hong, J. G. Kim, J. H. Lee, and J. G. Han, "Effect of Si addition to CrN coating on the corrosion resistance of CrN/stainless steel coating/substrate system in deaerated 3.5 wt.% NaCl solution," *Surface&Coating Technology,* vol. 201, pp. 9518-9523, 2007.

[148] I. D. Raistrick, J. R. MacDonald, and D. R. Franceschetti, *The electrical analogs of physical and chemical process, in: J.R. MacDonald ,Impedance Spectroscopy*. New York: John Wiley & Sons, 2003.

[149] F. Mansfeld, H. Shih, H. Greene, and C. M. Tsai, *Analysis of EIS data for common corrosion process,* . Philadelphia, PA, : ASTM, 1993.

[150] B. Normand, H. Takenouti, M. Keddam, H. Liao, G. Monteil, and C. Coddet, "Electrochemical impedance spectroscopy and dielectric properties of polymer: application to PEEK thermally sprayed coating," *Electrochimica Acta,* vol. 49, pp. 2981-2986, 7/30/ 2004.

[151] J. Vogelsang and W. Strunz, "New interpretation of electrochemical data obtained from organic barrier coatings," *Electrochimica Acta,* vol. 46, pp. 3817-3826, 8/15/ 2001.

[152] J. B. Jorcin, M. E. Orazem, N. Pébère, and B. Tribollet, "CPE analysis by local electrochemical impedance spectroscopy," *Electrochimica Acta* vol. 51, pp. 1473-1479., 2006.

[153] J. E. G. González, a. F. J. H. Santana, and J. C. Mirza-rosca, "Effect of bacterial biofilm on 316 SS corrosion in natural seawater by eis," *Corrosion Science,* vol. 40, pp. 2141-2154, 12/1998.

[154] D. A. López, N. C. Rosero-Navarro, J. Ballarre, A. Durán, M. Aparicio, and S. Ceré, "Multilayer silica-methacrylate hybrid coatings prepared by sol–gel on stainless steel 316L: Electrochemical evaluation," *Surface and Coatings Technology,* vol. 202, pp. 2194-2201, 2/15/ 2008.

[155] C. Liu, Q. Bi, A. Leyland, and A. Matthews, "An electrochemical impedance spectroscopy study of the corrosion behaviour of PVD coated steels in 0.5 N NaCl aqueous solution: Part I. Establishment of equivalent circuits for EIS data modelling," *Corrosion Science,* vol. 45, pp. 1243-1256, 6/2003.

[156] C.-c. Li, X.-y. Guo, S. Shen, P. Song, T. Xu, Y. Wen, *et al.*, "Adsorption and corrosion inhibition of phytic acid calcium on the copper surface in 3 wt% NaCl solution," *Corrosion Science,* vol. 83, pp. 147-154, 6/2014.

[157] M. Mohamedi, D. Takahashi, T. Uchiyama, T. Itoh, M. Nishizawa, and I. Uchida, "Explicit analysis of impedance spectra related to thin films of spinel $LiMn_2O_4$," *Journal of Power Sources* vol. 93, pp. 93-103, 2001.

[158] M. Wagner, C. Kuarnström, A. Ivaska, and J. Bobacka, "Electrochemical properties of Novel porous carbon based material synthesized from polycyclic Aromatic hydrocarbons," *Electrochimica Acta,* vol. 105, pp. 384-393, 2013.

[159] C. Liu, A. Leyland, S. Lyon, and A. Matthews, "An a.c. impedance study on PVD CrN-coated mild steel with different surface roughnesses," *Surface and Coatings Technology,* vol. 76–77, Part 2, pp. 623-631, 12/1995.

[160] C. Liu, A. Leyland, S. Lyon, and A. Matthews, "Electrochemical impedance spectroscopy of PVD-TiN coatings on mild steel and AISI316 substrates," *Surface and Coatings Technology,* vol. 76–77, Part 2, pp. 615-622, 12/1995.

[161] T. Nabatame, M. Kimura, H. Yamada, A. Ohi, T. Ohishi, and T. Chikyow, "Influence of oxygen transfer in Hf-based high-k dielectrics on flatband voltage shif," *Thin Solids Films* vol. 520, pp. 3387-3391, 2012.

[162] T. Nabatame, Y. Nunoshige, M. Kadoshima, H. Takaba, K. Segawa, S. Kimura, *et al.*, "Changes in effective work function of HfxRu1−x alloy gate electrode," *Microelectronic Engineering,* vol. 85, pp. 1524-1528, 7/2008.

[163] N. Yasuda, H. Ota, T. Horikawa, T. Nabatame, H. Satake, A. Toriumi, *et al.*, *Ext. Abstr.Solid State Devices and Materials, ,* p. 250, 2005.

[164] N. G. Pramod and S. N. Pandey, "Influence of Sb doping on the structural, optical, electrical and acetone sensing properties of In2O3 thin films," *Ceramics International,* vol. 40, pp. 3461-3468, 3/2014.

[165] T. Abe, S. Inoue, and K. Watanabe, "XRD and electrochemical measurements of RuO2 powder treated by using a mechanical grinding method," *Journal of Alloys and Compounds,* vol. 358, pp. 177-181, 8/25/ 2003.

[166] J. C. Cruz, V. Baglio, S. Siracusano, V. Antonucci, A. S. Aricò, R. Ornelas, *et al.*, "Preparation and characterization of RuO2 catalysts for oxygen evolution in a solid polymer electrolyte," *International Journal of Electrochemical Science* vol. 6, pp. 6607-6619., 2011.

[167] S. Jung, N. G. Park, M. Y. Kwak, B. O. Kim, K. H. Choi, Y. J. Cho, *et al.*, "Surface treatment effects of indium–tin oxide in organic light-emitting diodes," *Optical Materials,* vol. 21, pp. 235-241, 1/2003.

[168] Y. Qiu and J. Qiao, "Photostability and morphological stability of hole transporting materials used in organic electroluminescence," *Thin Solid Films,* vol. 372, pp. 265-270, 9/1/ 2000.

[169] J. Davenas, S. Besbes, A. Abderrahmen, N. Jaffrezic, and H. Ben Ouada, "Surface characterisation and functionalisation of indium tin oxide anodes for improvement of charge injection in organic light emitting diodes," *Thin Solid Films,* vol. 516, pp. 1341-1344, 2/15/ 2008.

[170] R. L. Weiher, "Electrical properties of single crystals of indium oxide," *Journal of Applied Physics,* vol. 33, p. 2834, 1962.

[171] J. Hamberg and C. G. Granquist, "Evaporated Sn-doped In2O3 films: Basic optical properties and applications to energy-efficient windows," *Journal of Applied Physics* vol. 60, 1986.

[172] J.-H. Huang and M.-S. Wong, "Structures and properties of titania thin films annealed under different atmosphere," *Thin Solid Films,* vol. 520, pp. 1379-1384, 12/30/ 2011.

[173] S. Yoon, I. Huh, J. H. Lim, and B. Yoo, "Annealing effects on electrical and optical properties of ZnO thin films synthesized by the electrochemical method," *Current Applied Physics,* vol. 12, pp. 784-788, 2012.

[174] P. Homhuan, T. Nabatame, T. Chikyow, and S. Tungasmita, "Effect of Y content in (TaC)1-xYx gate electrodes on flatband voltage control for Hf-based high-k gate stacks," *Japanese Journal of Applied Physics* vol. 50, 2011.

จุฬาลงกรณ์มหาวิทยาลัย
CHULALONGKORN UNIVERSITY

APPENDIX

EIS simulation

1. Set up the Impedance program as below figure;

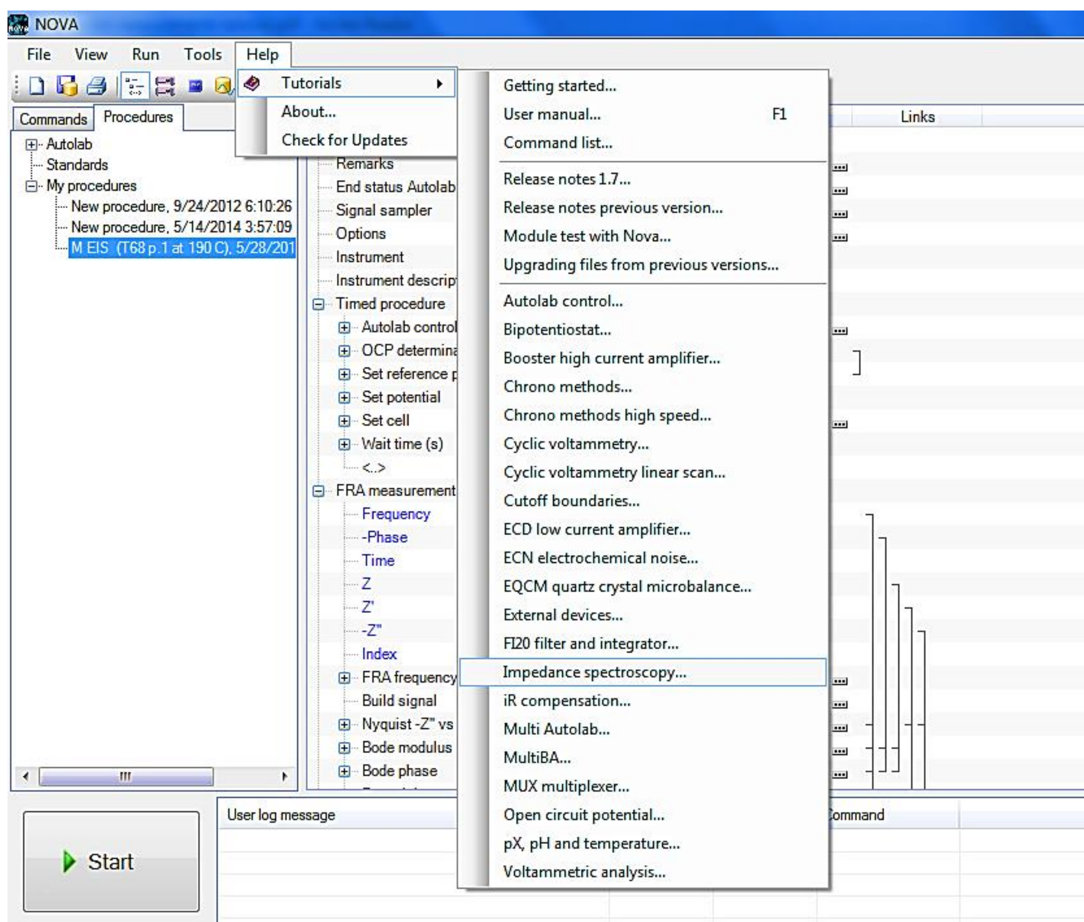

2. Using command as below figure;

NOVA

File View Run Tools Help

Commands | Procedures

Autolab
Standards
My procedures
New procedure, 9/24/2012 6:10:26
New procedure, 5/14/2014 3:57:09
M EIS (T68 p.1 at 190 C), 5/28/201

Commands	Parameters	Links
M EIS (T68 p.1 at 190 C)		
Remarks	FRA impedance potentiostatic: require...	
End status Autolab		
Signal sampler	No signals.	
Options	1 Options	
Instrument		
Instrument description		
Timed procedure		
Autolab control		
OCP determination	[-0.480]	
Set reference potential	-0.480	
Set potential	0.000	
Set cell	On	
Wait time (s)	5	
<..>		
FRA measurement potentiostatic		
Frequency	<..array..> (Hz)	
-Phase	<..array..> (°)	
Time	<..array..> (s)	
Z	<..array..> (Ω)	
Z'	<..array..> (Ω)	
-Z''	<..array..> (Ω)	
Index	<..array..>	
FRA frequency scan		
Build signal		
Nyquist -Z'' vs Z'		
Bode modulus		
Bode phase		

Start

User log message	Time	Date	Command

Ready

จุฬาลงกรณ์มหาวิทยาลัย
Chulalongkorn University

3. The results after EIS testing as shown in figure

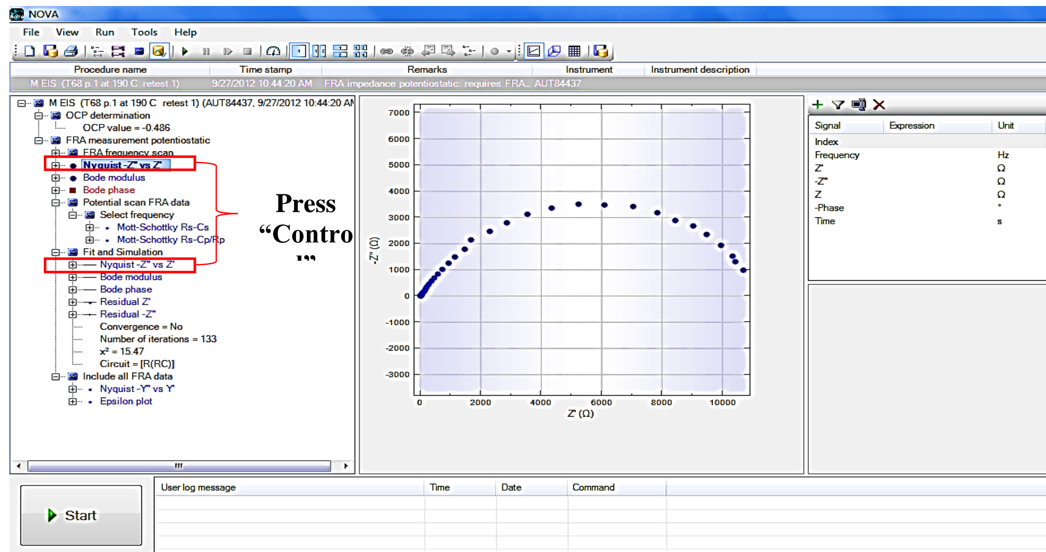

4. The new window appear

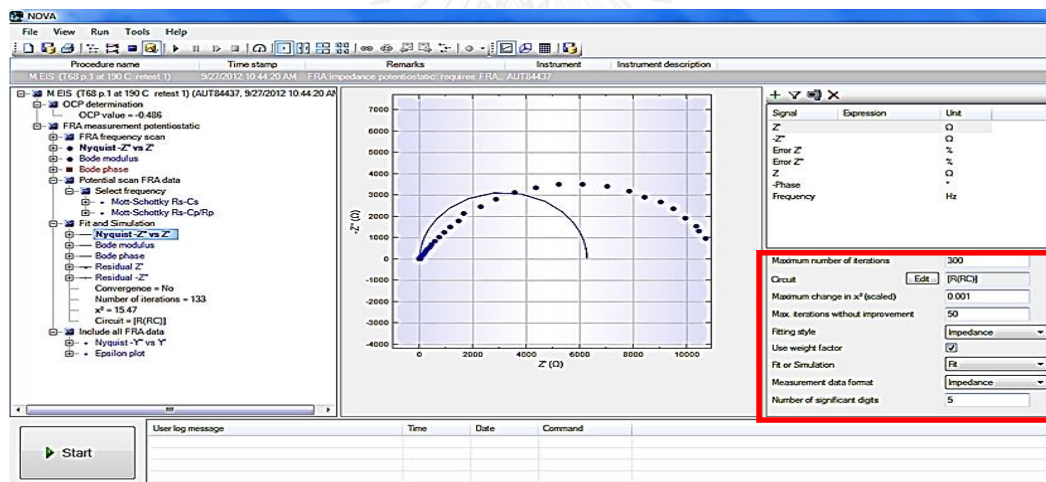

5. Click "Edit" for opening "Equivalent Circuit Editor" and then click "OK" for fitting circuit

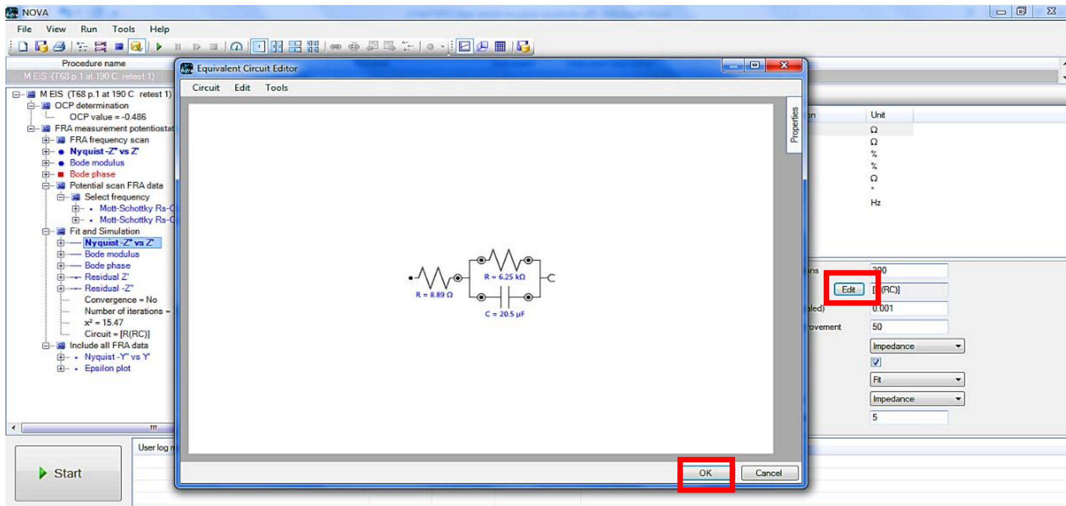

จุฬาลงกรณ์มหาวิทยาลัย
CHULALONGKORN UNIVERSITY

6. Final fitting circuit

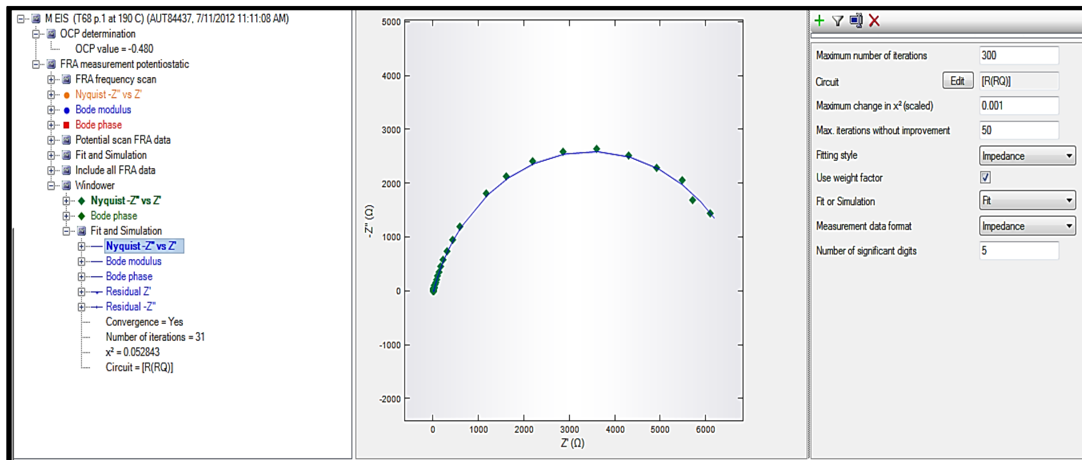

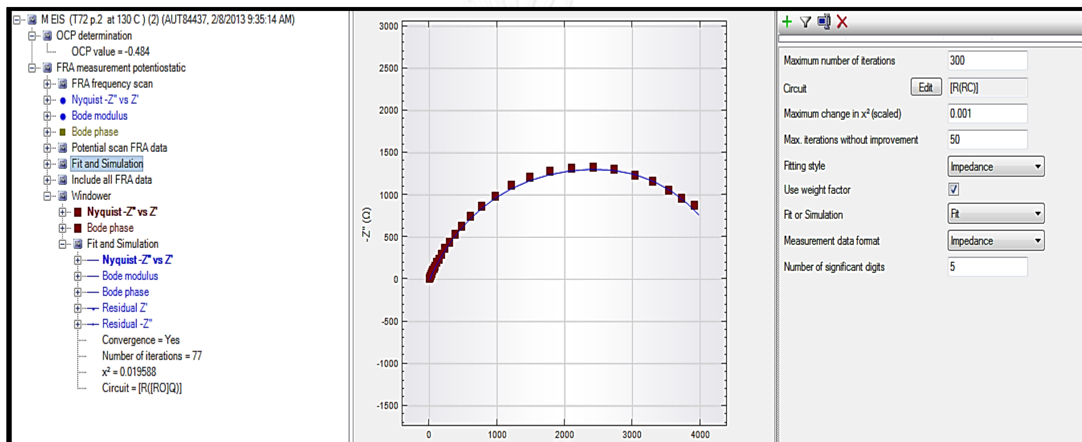

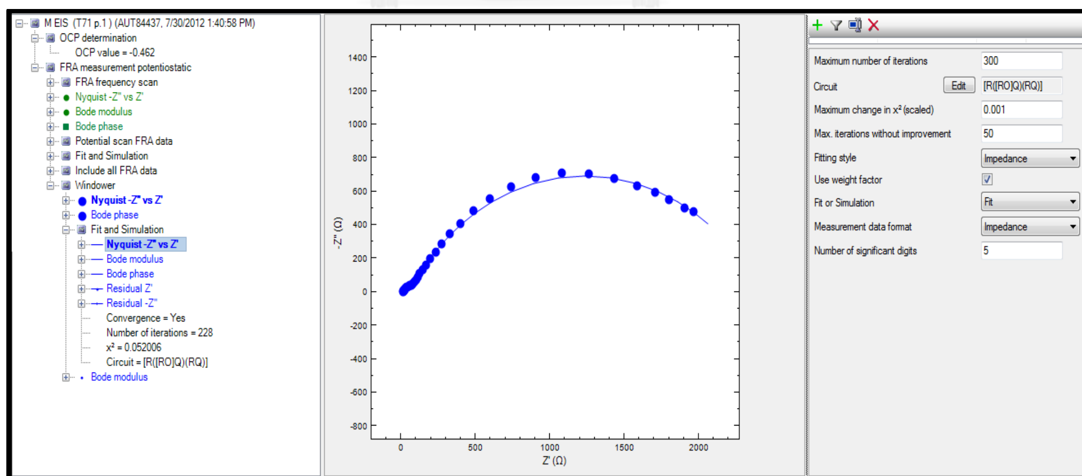

In_2O_3 Properties

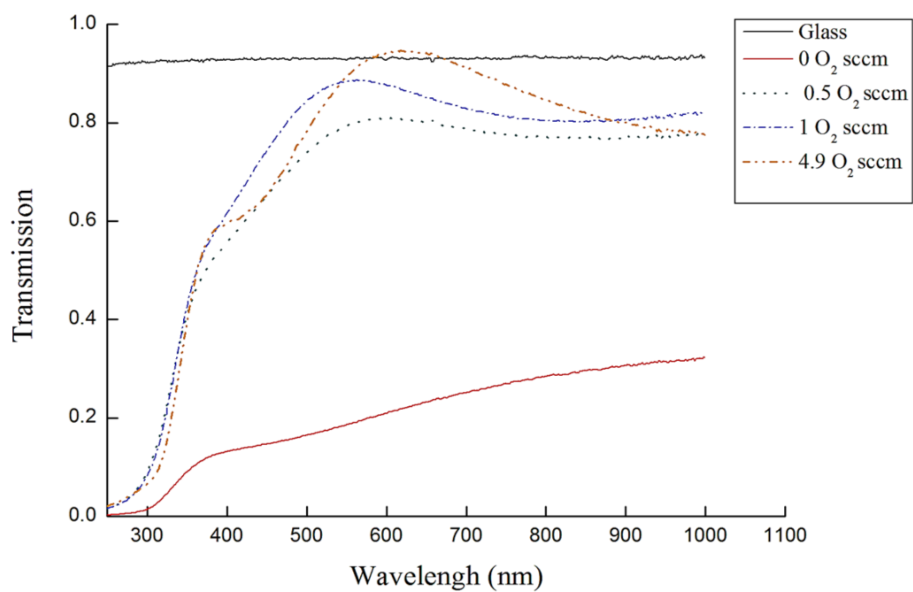

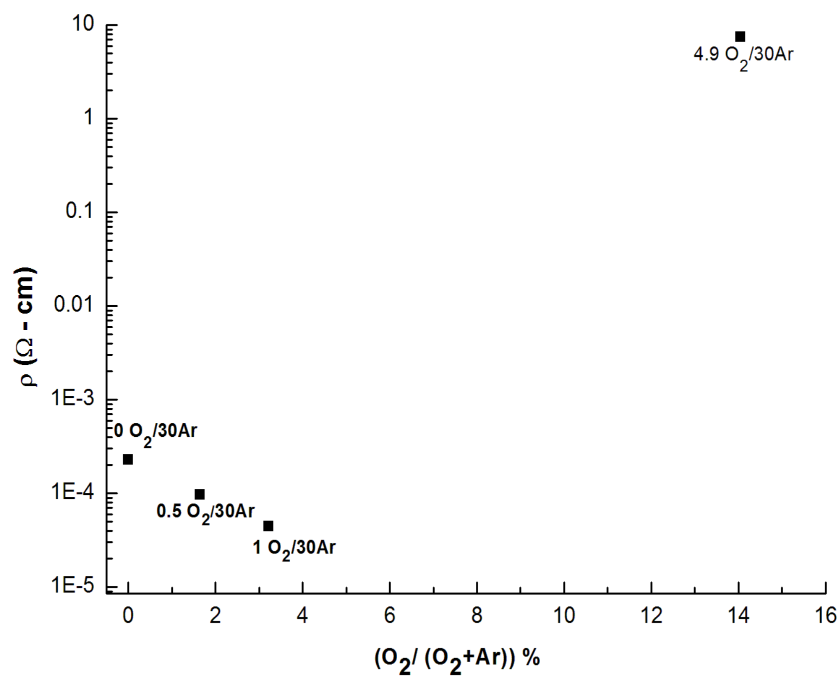

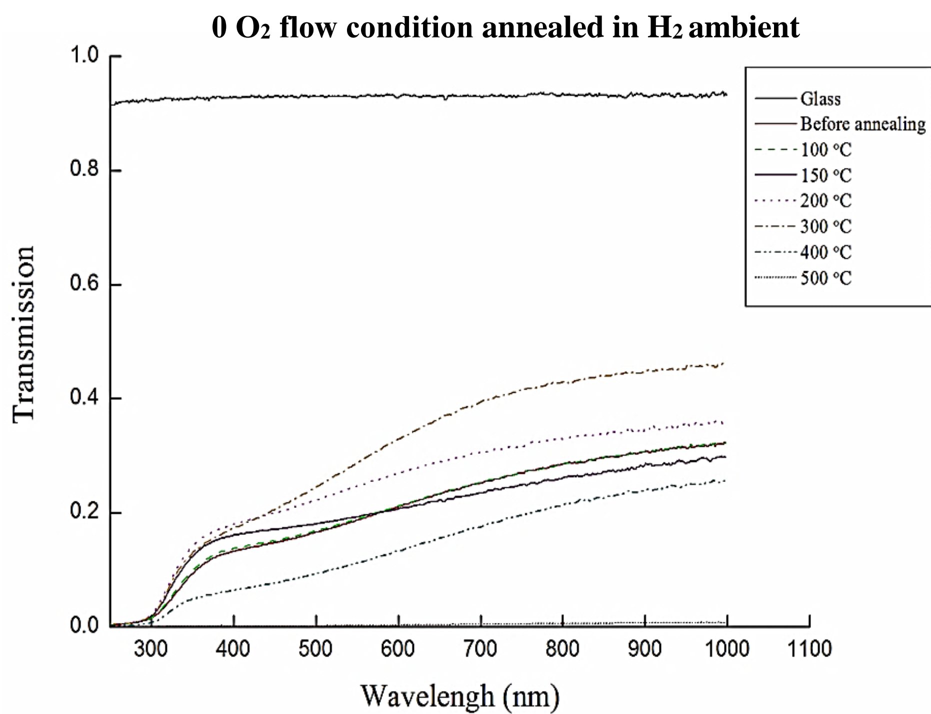
0 O2 flow condition annealed in H2 ambient
Transmission
Wavelengh (nm)
Glass
Before annealing
100 °C
150 °C
200 °C
300 °C
400 °C
500 °C
1.0
0.8
0.6
0.4
0.2
0.0
300
400
500
600
700
800
900
1000
1100

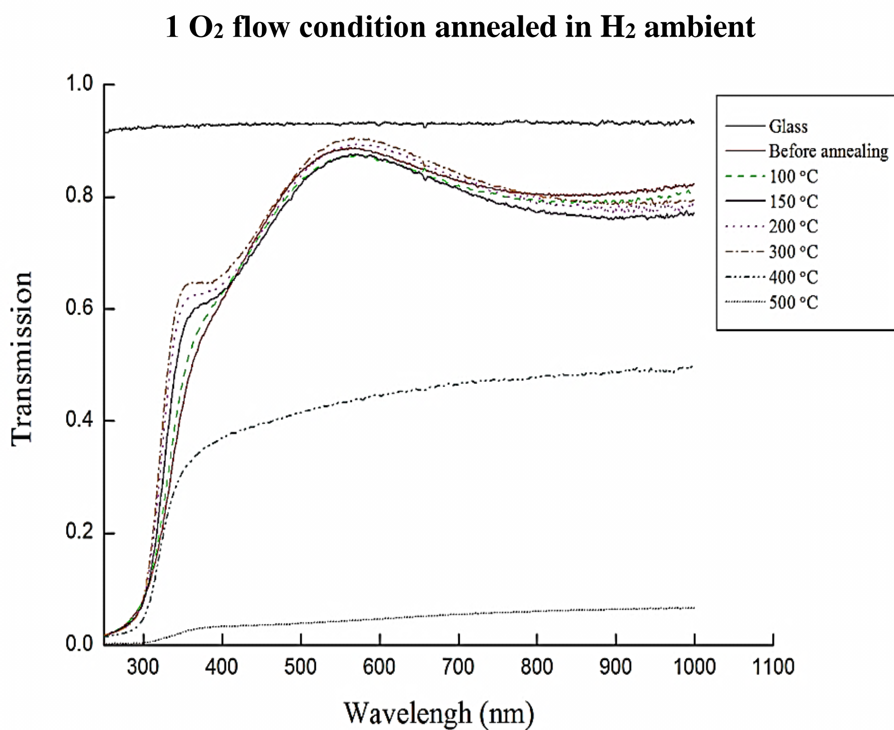
1 O2 flow condition annealed in H2 ambient
Transmission
Wavelengh (nm)
Glass
Before annealing
100 °C
150 °C
200 °C
300 °C
400 °C
500 °C
1.0
0.8
0.6
0.4
0.2
0.0
300
400
500
600
700
800
900
1000
1100

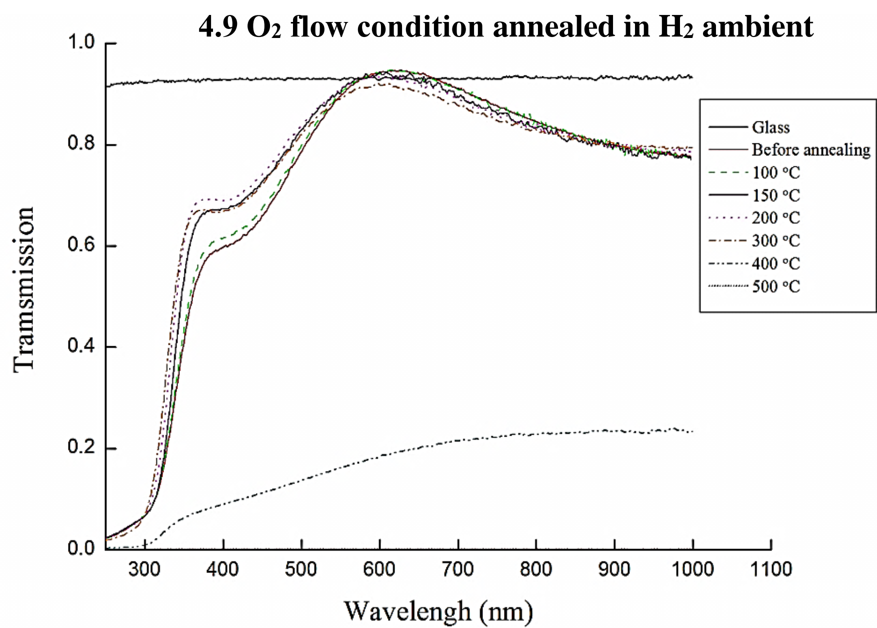
4.9 O2 flow condition annealed in H2 ambient
Tramsmission
Wavelengh (nm)
Glass
Before annealing
100 °C
150 °C
200 °C
300 °C
400 °C
500 °C
1.0
0.8
0.6
0.4
0.2
0.0
300
400
500
600
700
800
900
1000
1100

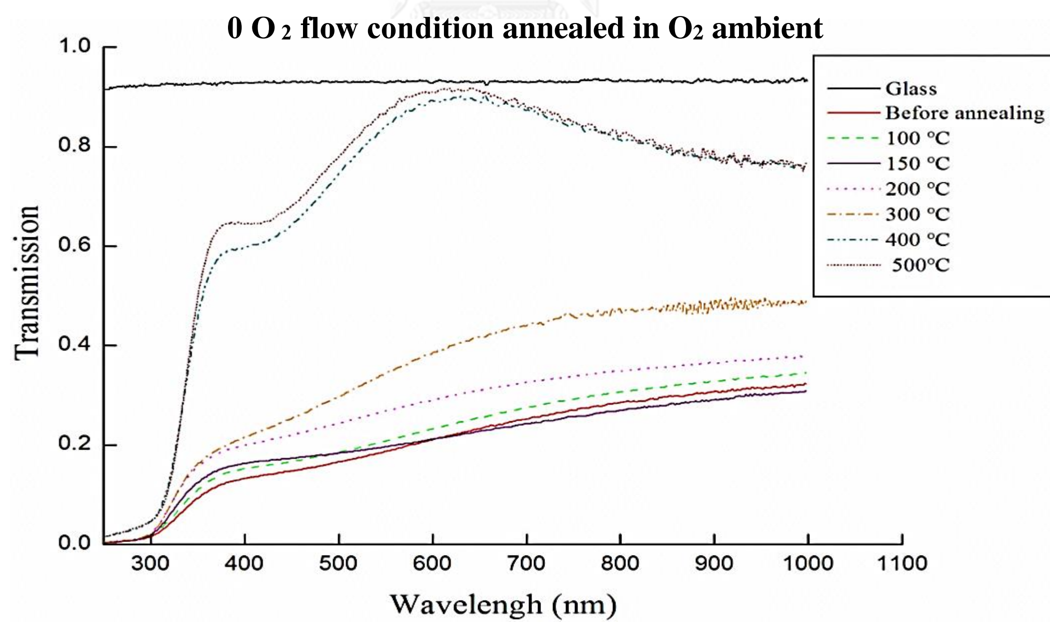
0 O 2 flow condition annealed in O2 ambient
Transmission
Wavelengh (nm)
Glass
Before annealing
100 °C
150 °C
200 °C
300 °C
400 °C
500°C
1.0
0.8
0.6
0.4
0.2
0.0
300
400
500
600
700
800
900
1000
1100

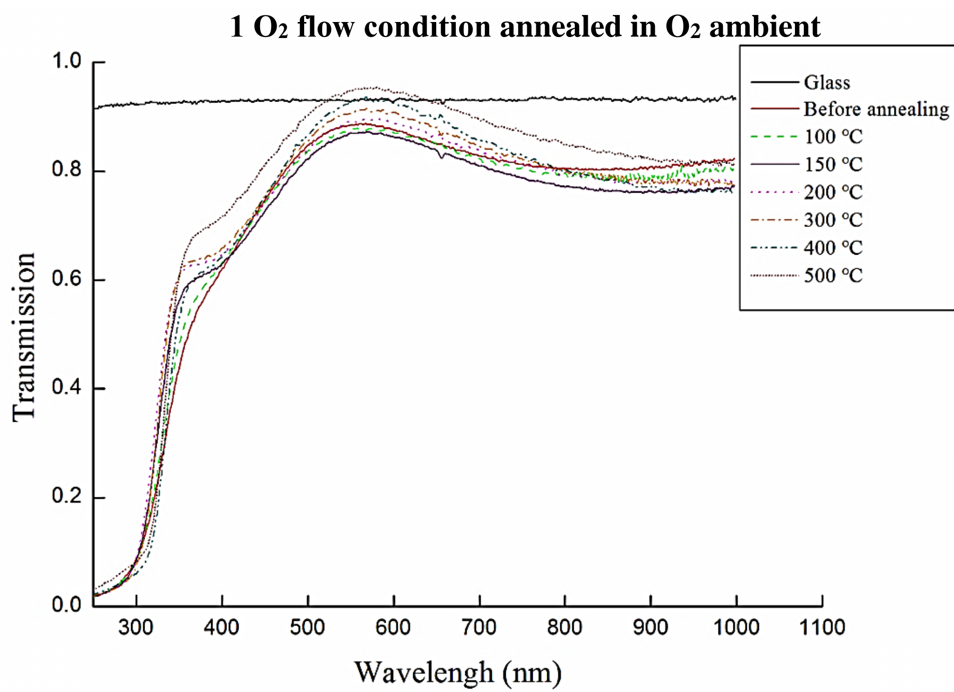

1 O2 flow condition annealed in O2 ambient
Transmission
Wavelengh (nm)
1.0
0.8
0.6
0.4
0.2
0.0
300
400
500
600
700
800
900
1000
1100
Glass
Before annealing
100 °C
150 °C
200 °C
300 °C
400 °C
500 °C

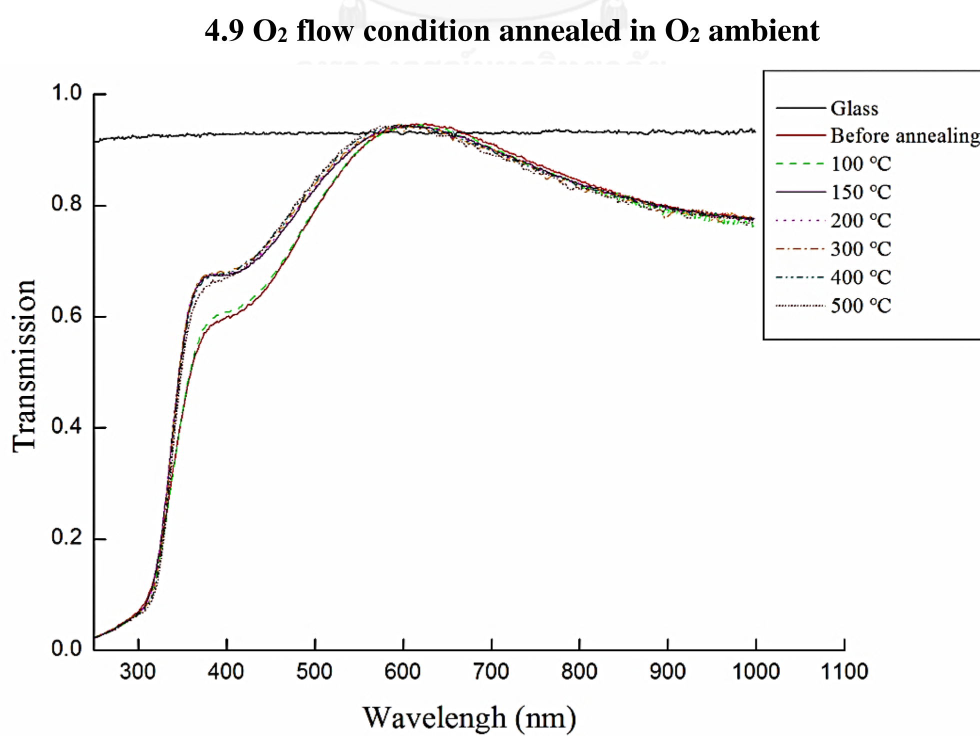

4.9 O2 flow condition annealed in O2 ambient
Transmission
Wavelengh (nm)
1.0
0.8
0.6
0.4
0.2
0.0
300
400
500
600
700
800
900
1000
1100
Glass
Before annealing
100 °C
150 °C
200 °C
300 °C
400 °C
500 °C

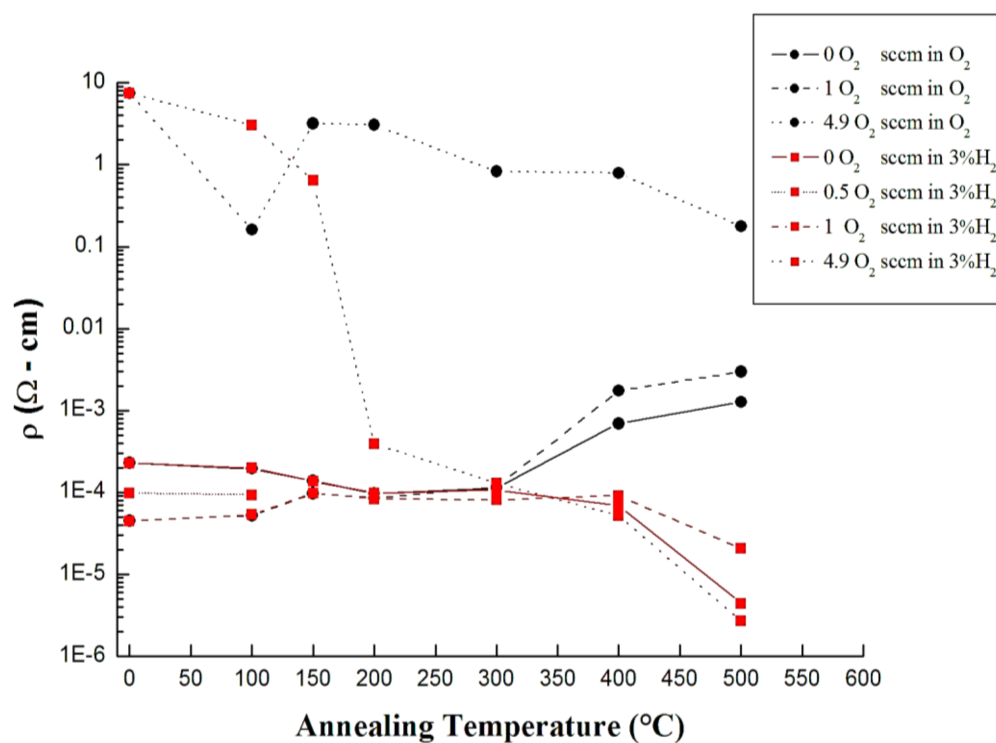
0 O2 sccm in O2
1 O2 sccm in O2
4.9 O2 sccm in O2
0 O2 sccm in 3%H2
0.5 O2 sccm in 3%H2
1 O2 sccm in 3%H2
4.9 O2 sccm in 3%H2
ρ (Ω - cm)
10
1
0.1
0.01
1E-3
1E-4
1E-5
1E-6
0
50
100
150
200
250
300
350
400
450
500
550
600
Annealing Temperature (°C)

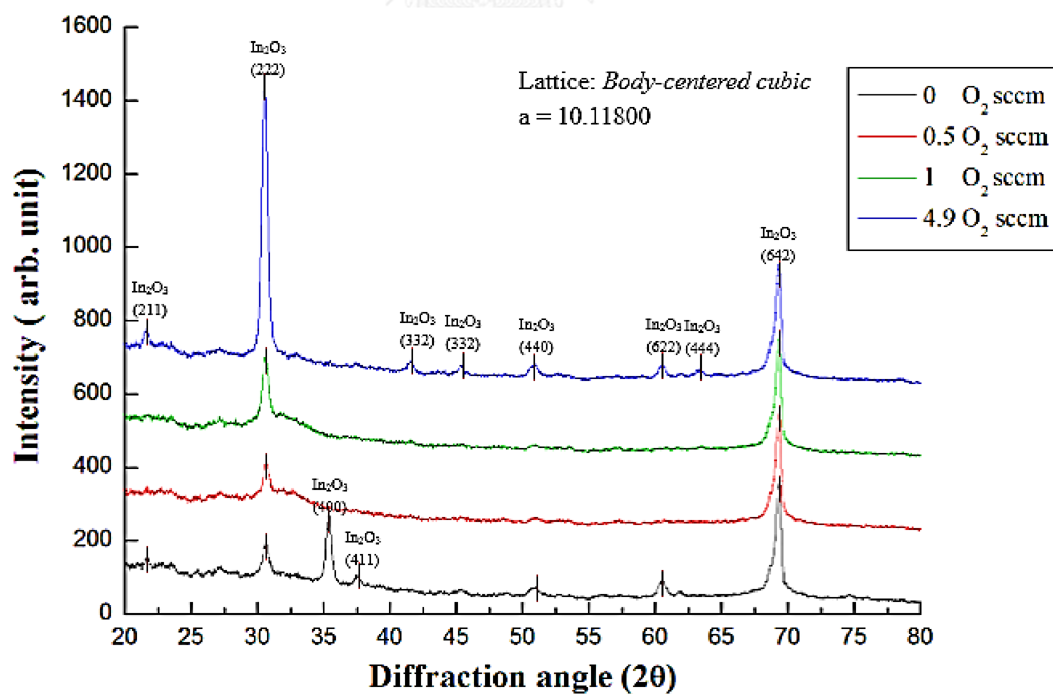
Lattice: Body-centered cubic
a = 10.11800
0 O2 sccm
0.5 O2 sccm
1 O2 sccm
4.9 O2 sccm
In2O3 (222)
In2O3 (211)
In2O3 (332)
In2O3 (332)
In2O3 (440)
In2O3 (622)
In2O3 (444)
In2O3 (642)
In2O3 (400)
In2O3 (411)
Intensity (arb. unit)
Diffraction angle (2θ)

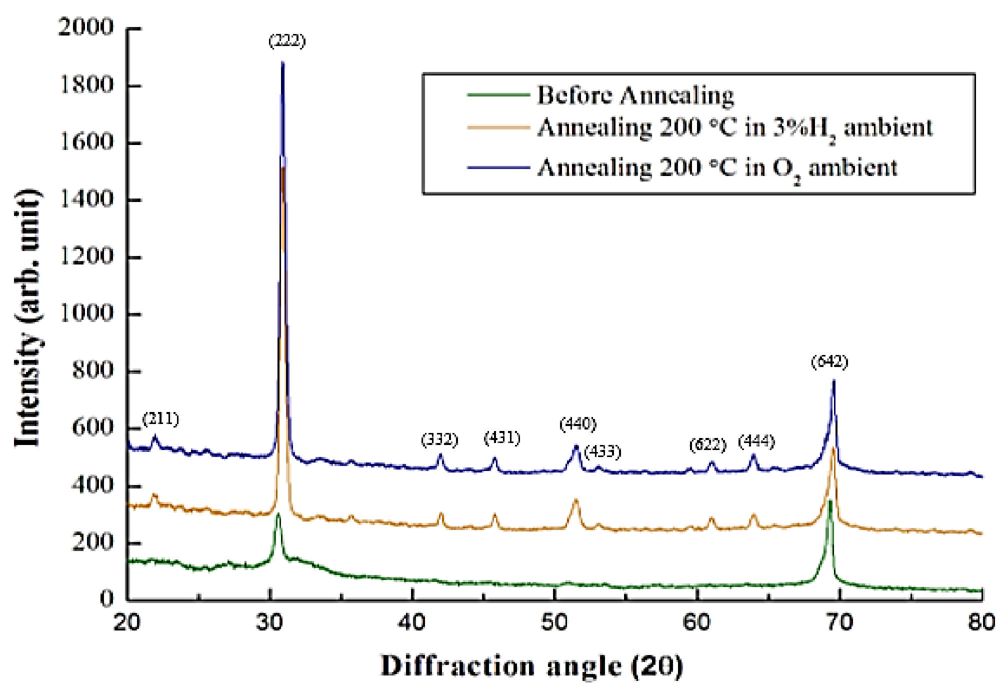
Intensity (arb. unit)
Diffraction angle (2θ)
Before Annealing
Annealing 200 °C in 3%H2 ambient
Annealing 200 °C in O2 ambient
(222)
(211)
(332)
(431)
(440)
(433)
(622)
(444)
(642)

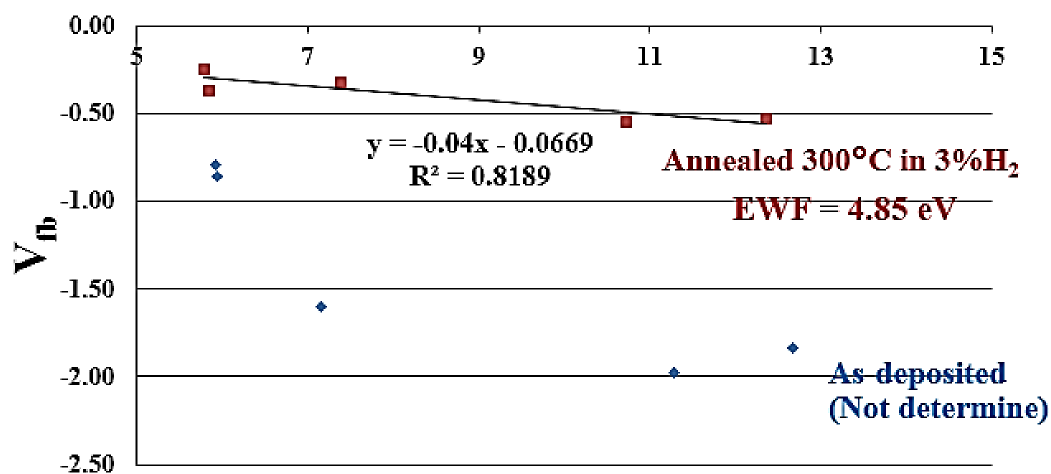
EOT
Vfb
y = -0.04x - 0.0669
R² = 0.8189
Annealed 300°C in 3%H2
EWF = 4.85 eV
As deposited
(Not determine)

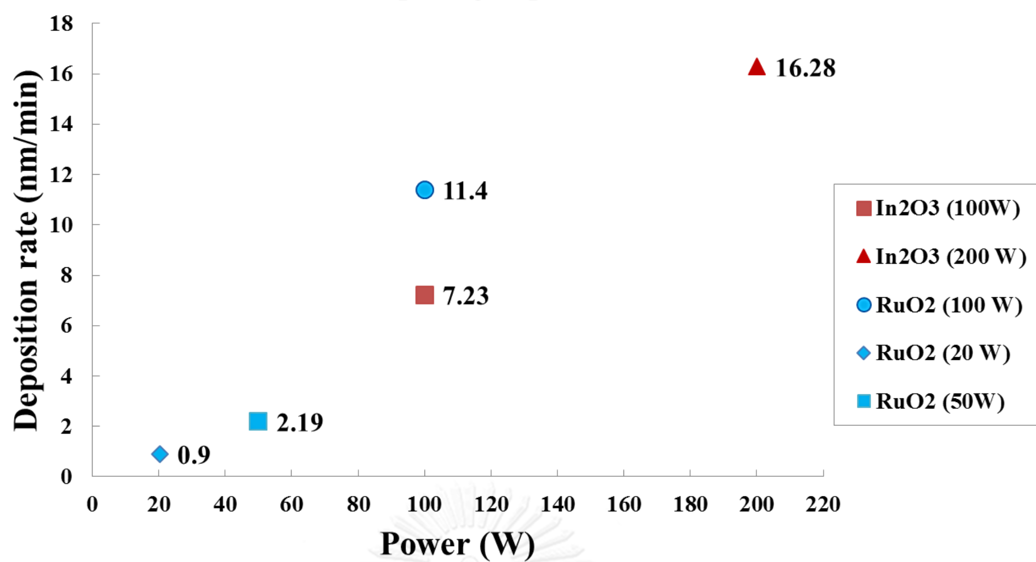
Comparing Deposition Rate
Deposition rate (nm/min)
Power (W)
16.28
11.4
7.23
2.19
0.9
In2O3 (100W)
In2O3 (200 W)
RuO2 (100 W)
RuO2 (20 W)
RuO2 (50W)

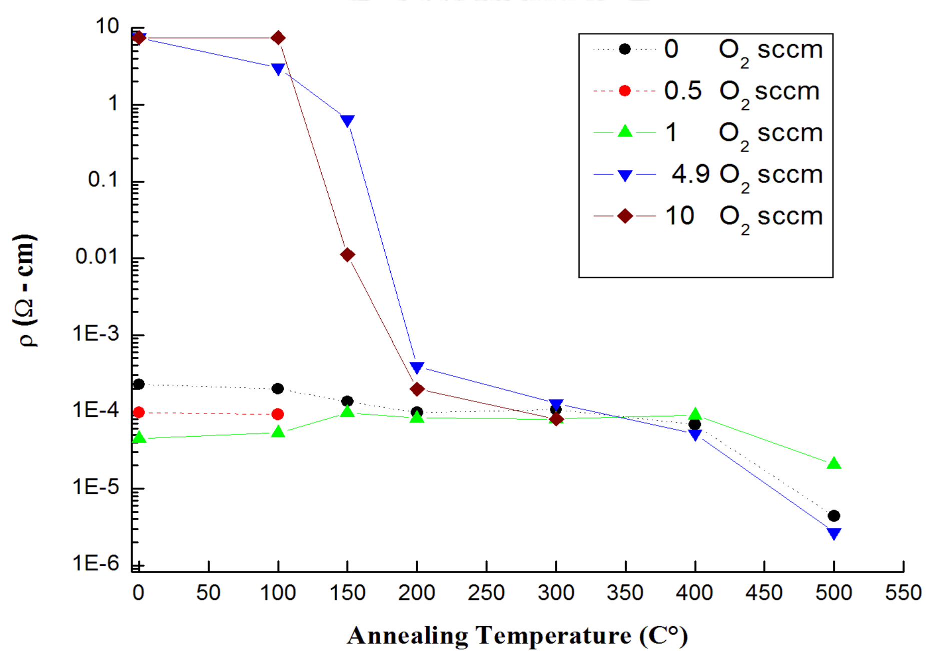
ρ (Ω - cm)
Annealing Temperature (C°)
0 O2 sccm
0.5 O2 sccm
1 O2 sccm
4.9 O2 sccm
10 O2 sccm

Calculation atomic ratio by using sputtering power

In_2O_3

In_2O_3 Density is 7.179 g/cm^3

Molar mass of In_2O_3 277.64 g/mol

Atomic ratio (i :j) = atomic percent (i) : atomic percent (j)

Atomic percent (i) = $\frac{Ni}{N\ total} \times 100$

RuO_2

RuO_2 Density is 6.97 g/cm^3

Molar mass of In_2O_3 133.0688 g/mol

Atomic ratio (i :j) = atomic percent (i) : atomic percent (j)

Atomic percent (i) = $\frac{Ni}{N\ total} \times 100$

Condition $In_{0.95}Ru_{0.62}O_y$ film: In_2O_3 deposition rate 16.28 nm/min (1.63×10^{-6} cm/min)

1. Rate × time× area

   = 1.63×10^{-6} cm/min × 7.58 min × (1.8 cm× 1.8 cm)

   Volume = 40.0315×10^{-6} cm^3

2. Volume × density = weight

   =40.0315×10^{-6} cm^3 × 7.179 g/cm^3

   =287.3861×10^{-6} g

3. $\frac{weight}{molar\ mass} = \frac{287.3861 \times 10^{-6}}{277.64\ g/mol} = 1.035 \times 10^{-6}$ mol

Condition $In_{0.95}Ru_{0.62}O_y$ film: RuO_2 deposition rate 0.9 nm/min (0.09×10^{-8} cm/min)

1. Rate × time× area

   = 0.09×10^{-6} cm/min × 7.58 min × (1.8 cm× 1.8 cm)

   Volume = 2.21×10^{-6} cm^3

2. Volume × density = weight

   =2.21×10^{-6} cm^3 × 6.97 g/cm^3

   =15.4037×10^{-6} g

3. $\frac{weight}{molar\ mass} = \frac{15.4 \times 10^{-6}}{133.068\ g/mol} = 0.1157 \times 10^{-6}$ mol

4. **Condition $In_{0.95}Ru_{0.62}O_y$ film**: N_{total} = (2 mol × In) + (Ru)

= (2× 1.035 × 10^{-6} mol) + (0.1157 × 10^{-6} mol)

= 2.18× 10^{-6} mol

1. In_2O_3 atomic percent (i) = $\frac{2.07\times10^{-6}}{2.18\times10^{-6}}$ × 100 = 0.95 ×100 = 95.0%
2. RuO_2 atomic percent (i) = $\frac{0.1157\times10^{-6}}{2.18\times10^{-6}}$ × 100 =0.05 ×100 = 5 %

Condition $In_{0.38}Ru_{0.62}O_y$: In_2O_3 deposition rate 7.23 nm/min (7.23×10^7cm/min)

1. Rate × time× area

   = 7.23×10^{-7} cm/min × 7.22 min × (1.8 cm× 1.8 cm)

   Volume = 169.029 × 10^{-7} cm^3

2. Volume × density = weight

   =169.129 × 10^{-7} cm^3 × 7.179 g/cm^3

   =1.21 × 10^{-4} g

3. $\frac{weight}{molar\ mass} = \frac{1.21\times10^{-4}}{277.64\ g/mol}$ =4.35 × 10^{-7} mol

Condition $In_{0.38}Ru_{0.62}O_y$: RuO_2 deposition rate 11.4 nm/min (11.4 ×10^{-7} cm/min)

1. Rate × time× area

   = 11.4×10^{-7} cm/min × 7.22 min × (1.8 cm× 1.8 cm)

   Volume = 2.66 × 10^{-5} cm^3

2. Volume × density = weight

   =2.66 × 10^{-5} cm^3 × 6.97 g/cm^3

   =1.86× 10^{-4} g

3. $\frac{weight}{molar\ mass} = \frac{1.86\times10^{-4}}{133.068\ g/mol}$ =1.39 × 10^{-6} mol

Condition $In_{0.38}Ru_{0.62}O_y$: N_{total} = (2 mol × In) + (Ru)

= (2×4.35 × 10^{-7} mol) + (1.39 × 10^{-6} mol)

= 2.26× 10^{-6} mol

1. In_2O_3 atomic percent (i) = $\frac{0.87\times10^{-6}}{2.26\times10^{-6}}$ × 100 = 0.384 ×100 = 38 %
2. RuO_2 atomic percent (i) = $\frac{1.39\times10^{-6}}{2.26\times10^{-6}}$ × 100 =0.615 ×100 = 62%

VITA

Kattareeya Taweesup, received D.Eng and master degrees in Metallurgical Engineering from Chulalongkorn University in 2014 and 2008. She graduated with a bachelor's degree in Metallurgical Engineering from Suranaree University of Technology in 2006. Her research scope include nitriding treatment, DC magnetron sputter and corrosion characterizations.

จุฬาลงกรณ์มหาวิทยาลัย
CHULALONGKORN UNIVERSITY